Investigating the anion doping effect on the conductivity and stability of cost-effective halide solid electrolytes

Mateo Bouillez

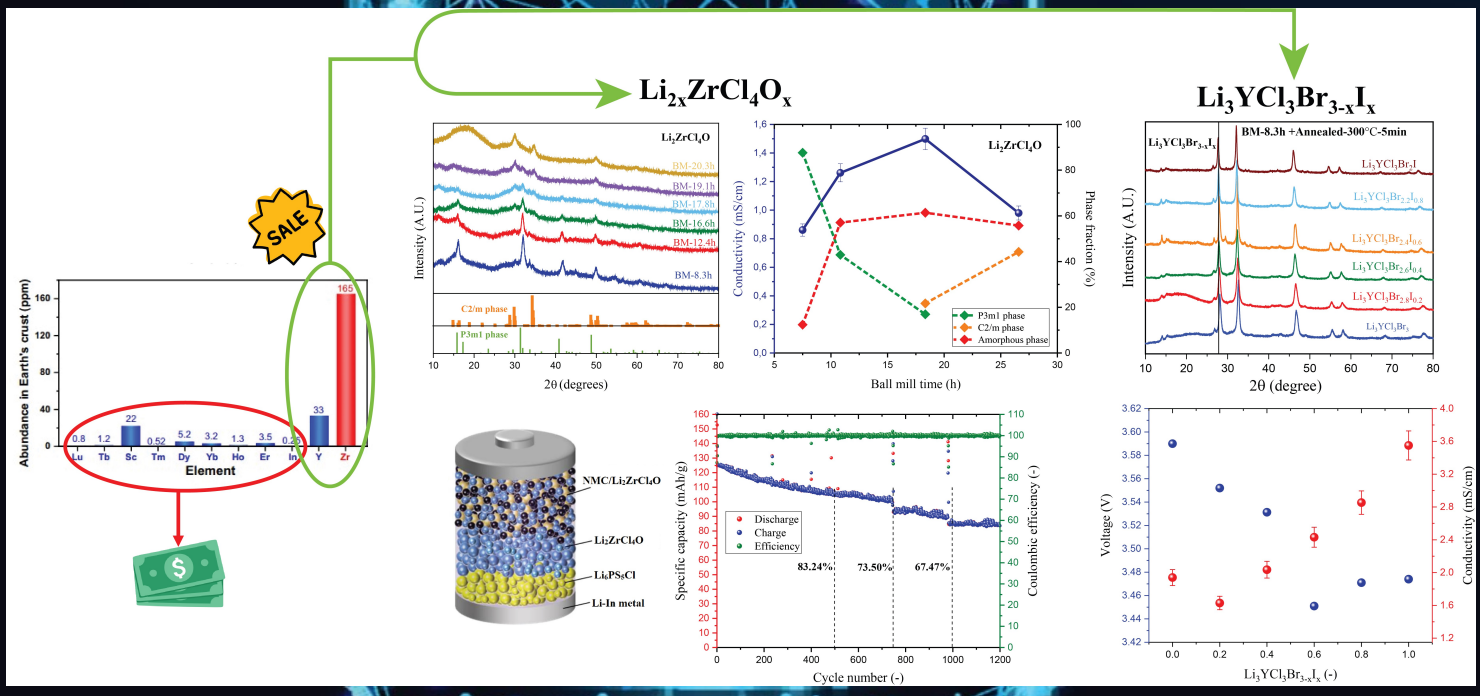

Delft University of Technology

TU Delft

Investigating the anion doping effect on the conductivity and stability of cost-effective halide solid electrolytes

by

Mateo Bouillez

to obtain the degree of Master of Science
at the Delft University of Technology
to be defended publicly on November 7, 2023 at 15:00

Thesis committee:

Supervisor:	Prof. dr. ir. M. Wagemaker - TU Delft
External examiner	Dr. X. Wang - TU Delft
	Dr. S.W.H Eijt - TU Delft
Student number:	5644305

An electronic version of this thesis is available at `http://repository.tudelft.nl/`.

Faculty of Applied Sciences
Department Radiation Science and Technology | Storage of Electrochemical Energy (SEE) Group

TU Delft

Acknowledgements

I have had a great time working on this thesis project within the SEE group where I learned a lot. I would like to thank the members from the S&D group meeting that helped me during the project to answer all my questions. Especially thanks to Shengnan Zhang for the help with SEM measurements and for always being so kind and smiling. Also, Ajay Gautam for the suggestions and helping with the refinements and Robert Dankelman for the XRD measurement training. Meng-Fu Tu who became my lab buddy with whom we spend time together in the lab until late. Frans Ooms and Esther Bijl for keeping the labs running and helping for any equipment questions. Thank you to everyone in the group for their kindness.

I want to thank the defense committee members for agreeing to be in my committee.

A very special thanks to my supervisor Zhu Cheng who is an incredibly friendly, kind and helpful person without whom my thesis would not have been this enjoyable. Always taking time to explain to me any questions I have, always being available when needed and always joking and being positive. I could not have asked for a better supervisor.

Of course, thank you to my friends from the 8th floor of EWI and my roommates Nicholas, Daniel and Giacomo for cooking and teaching me a better dish than my favorite pasta with ketchup. Thank you to my parents and sister. And finally, Irmak for always being there and supporting me.

Mateo Bouillez
Delft, November 2023

Abstract

Batteries play a vital role in the ongoing energy transition, driving the demand for safer, energy denser and higher performing energy storage solutions. This has propelled research of solid-state batteries. Halide electrolytes, with high ionic conductivities and high oxidation stabilities, have attracted tremendous interest. Currently, the main challenge is that most promising halide solid electrolytes are reliant on expensive and scarce metals, hindering their application at an industrial scale. Therefore, it is of great significance to develop cost-effective halide electrolytes. Zr-based electrolytes show great promise due to their cost-effectiveness ($ZrCl_4$ = 12.5 USD/kg) and high abundance in the earth's crust (165 mg/kg). However, so far their conductivity have been unsatisfactory, falling below 1 mS/cm. Anion doping with elements like Cl, Br, I, and O has demonstrated to be effective in improving the conductivities of sulfide solid electrolyte. In this work, the O-doping effect is investigated in Zr-based halide solid electrolytes with $Li_{2x}ZrCl_4O_x$. By using various analysis techniques such as X-ray diffraction, electrochemical impedance spectroscopy, and cyclic voltammetry, this study explores the relationship between compositions, conductivities, and phases within the $Li_{2x}ZrCl_4O_x$ system. The findings reveal that, for each Zr-based oxyhalide composition, varying ball milling times result in different phases, with the most amorphous phase displaying the highest ionic conductivity. Specifically, for x = 1, Li_2ZrCl_4O reaches 1.60 mS/cm after 17.2 hours of ball milling, characterized by a structure featuring 61% amorphous content. Additionally, it demonstrates good performance as an all-solid-state battery with $LiNi_{0.8}Mn_{0.1}Co_{0.1}O_2$/ Li_2ZrCl_4O/ Li_6PS_5Cl/Li-In, achieving an initial capacity of 125.6 mAh/g at 0.5C and retaining 67.47% capacity after 1000 cycles. Moreover, the impact of I-doping is further explored in $Li_3YCl_3Br_{3-x}I_x$, another cost-effective halide solid electrolyte (YCl_3 = 330 USD/kg and 33 mg/kg). The $Li_3YCl_3Br_{3-x}I_x$ electrolyte displays tunable conductivity and stability characteristics with an excellent conductivity of 3.55 mS/cm for x = 1 compared to 1.94 mS/cm for x = 0 but with a trade-off in oxidation potential of 3.474 V to 3.59 V. This study provides insights into novel cost-effective electrolytes and exhibits the potential of anion doping in enhancing and tuning both conductivity and stability. These electrolytes hold a serious potential as a solid electrolyte in solid-state batteries.

Contents

1

Background

1.1 General battery history and future need

Batteries are devices that store chemical energy and convert it to electrical energy. They find many applications in daily life such as laptops, electric vehicles and phones. The battery is an old discovery which was first found by Alessandro Volta in 1800. However, the first rechargeable battery was only found later by Gaston Planté in 1859 and was based on lead acid [1]. Since then, only a handful of other batteries have emerged on a commercial scale with most known the lithium-ion battery developed by Sony in 1991 [2].

From Figure 1a it is observed that the older battery technologies (lead-acid and Ni-Cd) have low energy densities and have not evolved much over time. Currently, considering commercially available batteries, lithium ion batteries hold the highest energy densities [3]. However, bottlenecks such as safety, limitations in energy density, environmental issues and charging speed with traditional Li-ion batteries have started the search for alternative battery technologies such as solid-state batteries.

Batteries have become an indispensable product in every day life, which is found all over the globe and will become even more important in the future. Since renewable sources such as solar and wind will become increasingly prevalent in future energy systems. Batteries can store surplus renewable energy generated during peak periods and supply it to the grid when renewable energy generation is limited, thereby mitigating grid congestion. Moreover, batteries are also crucial for the electrification of the transportation sector.

Considering the battery market, in the past it has been growing and is expected to expand substantially in the future as shown in Figure 1b [4]. The main producer of batteries in the world is China, where 70% of them are manufactured. The annual production of batteries in 2020 was 320 GWh. By targets set by governments around the globe it is anticipated that the annual battery production will be 1500 GWh by 2030 and in subsequent years 3000 GWh [5].

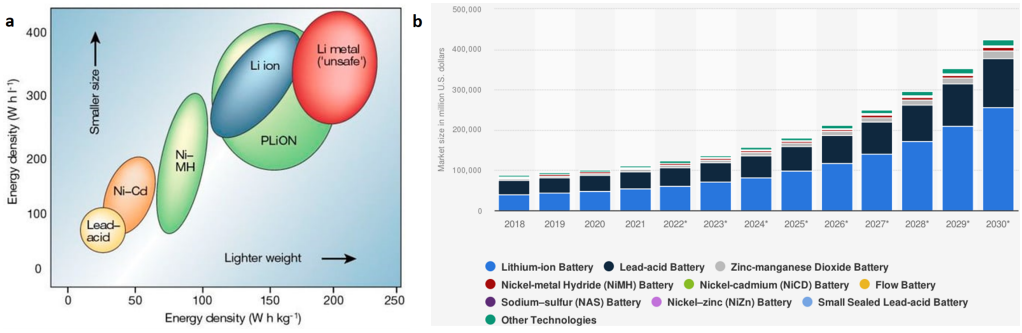

Figure 1: (a) Energy density plot of several battery technologies used in EVs [3] and (b) Expected battery market evolution [4]

1.2 Lithium-ion battery

1.2.1 Lithium-ion battery principle

In a typical lithium-ion battery structure, there are four main layers (as illustrated in Figure 2): the negative electrode (anode), positive electrode (cathode), electrolyte and separator. During the discharging process of the battery, Li^+ ions are released (deintercalation) at the anode along with electrons. The Li^+ ions pass through the electrolyte while the electrons flow through an external circuit towards the cathode. At the cathode, these electrons and ions recombine, completing a redox reaction, where one species loses an electron (oxidized), while the other gains an electron (reduced). Because this reaction is reversible, applying a current can initiate the reversal of these half-reactions, constituting the charging phase [6].

The primary function of the electrolyte is to only allow transport of ions (here Li^+) from one electrode to the other and prevents short circuiting. The separator, on the other hand, acts as a physical barrier between the anode and cathode. It only allows the passage of Li^+ ions while blocking the movement of electrons between both electrodes. This separation ensures the safe and efficient operation of the battery [7].

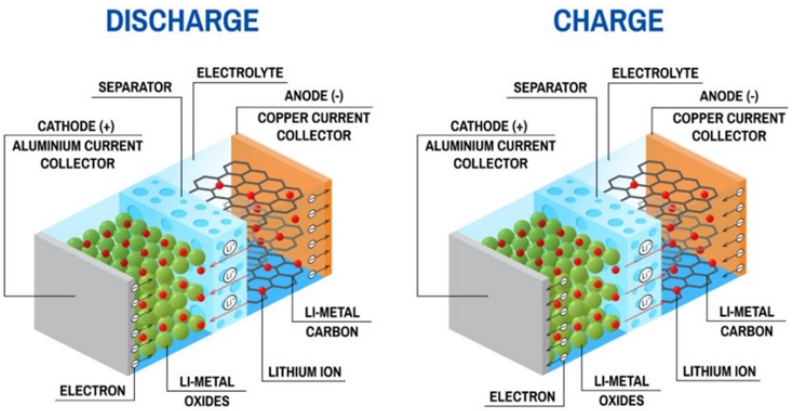

Figure 2: Li-ion battery charge and discharge working principle [8]

There exist various types of anode and cathode materials. For each type the fundamental principle remains the same. An example of a redox reaction in a commercial liquid lithium-ion battery is shown in equation 1 and 2. This redox reaction involves the transfer of electrons between different species. Here the transition metal "M", for example cobalt (Co), is oxidized from Co^{3+} to Co^{4+} within Li_xCoO_2 during the charging phase and is reduced from Co^{4+} to Co^{3+} during the discharging process [6]. The overall reaction results in a balanced reaction.

Positive electrode:

$$LiCoO_2 \Longleftrightarrow Li_{1-x}CoO_2 + xLi^+ + xe^- \tag{1}$$

Negative electrode:

$$6C + xLi^+ + xe^- \Longleftrightarrow Li_xC_6 \tag{2}$$

Overall reaction

$$LiCoO_2 + 6C \Longleftrightarrow Li_xC_6 + Li_{1-x}CoO_2 \tag{3}$$

1.2.2 Solid-state batteries

Lithium-ion batteries have the advantage of possessing a high discharge voltage, high cycle stability and good energy densities. For these reasons lithium-ion batteries are the most commercially used batteries [9]. Liquid lithium-ion batteries are still improving but they are approaching a physico-chemical limit that may hinder further advancements, particularly in terms of energy density [10].

Additionally, the liquid electrolytes in lithium ion batteries are highly flammable and pose a safety risk for larger systems due to fire accidents and explosions. Therefore, intensive research is being conducted in the field of all-solid-state batteries (ASSB) which aim to replace the liquid electrolyte with a solid electrolyte. Solid-state batteries (SSB) offer several advantages including potential for higher energy density (due to higher packing efficiency from less dead weight loss), freedom in the design of the battery geometry, compatibility with high potential cathodes and eliminate the safety concerns [11, 12]. Lastly, faster charging and discharging is possible due to better thermal stability meaning the SSB can run at higher currents [13].

The structure of a solid state battery is shown in Figure 3a with the anode, solid state electrolyte and the cathode. The current collector serves to collect the electrons generated at the anode during discharge and transport them through the external circuit to the cathode, where they combine with ions to complete the electrochemical reaction. Additionally, there is no need for a separator as the solid electrolyte already acts as a physical barrier between the anode and cathode.

In Figure 3b the reaction in a solid state battery is shown. This is the same principle as in a traditional battery.

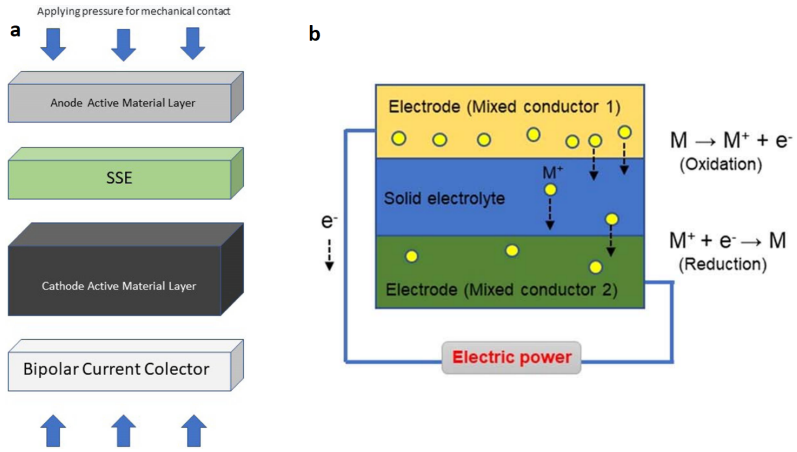

Figure 3: (a) Structure of a solid state battery [14]. (b) Solid state battery charge and discharge working principle [15]

1.2.3 Types of electrolytes

As stated previously, the purpose of electrolyte is to let ions flow between the positive and negative electrodes, enabling the flow of electric current while maintaining the charge balance within the system. The ideal electrolyte should have a good ionic conductivity (1 to 10 mS/cm), compressibility, and cost effectiveness [16]. Additionally, a wide electrochemical stability window is also important and a negligible electron conductivity [12]. Moreover, the electrolyte should exhibit compatibility and stability with the electrodes and should be safe. In the context of a complete battery, the battery should have extensive cycle life, elevated volumetric energy density, high power density and be cost-effective, and scalable.

There are many different electrolytes in batteries. The most common electrolyte type is the **non-aqueous liquid electrolytes** which are organic solvent-based electrolytes and are commonly used in lithium-polymer batteries [17]. However their main drawback is their flammability. Another important electrolyte

is the **aqueous electrolytes** which are water-based electrolytes and are commonly used in alkaline batteries and some types of flow batteries. But they are limited by the thermodynamic electrochemical window of water [18].

As mentioned before, another type of electrolyte is the **solid-state electrolytes** which are becoming increasingly researched due to their potential for enhancing safety, higher energy density, faster charging and discharging and cycle life. Solid electrolytes can be categorized into inorganic (e.g. oxides, sulfides, halides) and polymer electrolytes (gel and composite) [19]. In this report the solid electrolytes investigated are part of the halide and oxyhalide group.

Lastly, another interesting emerging electrolyte is the **hybrid electrolytes** that combine characteristics of inorganic solid and solid polymer electrolytes, that aim to achieve the benefits of both electrolytes while minimizing their drawbacks (e.g. high ionic conductivity and high electrode stability) [20].

1.2.4 Anode and Cathode materials

In liquid lithium-ion batteries, the most commonly used anode material is graphite, whereas in SSB, lithium metal is commonly employed as the anode. The reason for using Li-metal is that it has the lowest reduction potential (0 V vs. Li/Li^+) meaning that the overall cell voltage will be higher leading to higher energy density. Li-metal also holds high capacities (2046 mAh/cm^3 and 3862 mAh/g) [21]. However, due to stability issues with the solid electrolyte often an indium-lithium metal alloy is used.

Cathodes are more versatile and are selected by their rate capability and long term cycling. Some traditional cathode materials for lithium ion batteries are lithium oxides like $LiCoO_2$, NMC (lithium nickel manganese cobalt oxides) and lithium iron phosphates ($LiFePO_4$)[22, 23]. In SSBs, these materials are common cathodes, but sulfur and composite cathodes are examples of researched materials [9].

1.3 Raw material availability and cost

Future global demand for raw materials in batteries will increase drastically. Nickel, graphite and lithium demand are projected to increase by 20, 19 and 14 times, respectively, in 2040 compared to 2020. With China being the main exporter. In the future, shortfalls can be expected for these materials. Therefore, using more abundant materials, extending battery lifespan and recycling will become more and more important. Additionally, extensive research is being conducted to enhance battery technologies with greater performance, superior energy density, faster charging, enhanced environmental safety (e.g. cobalt mining and material availability) and more cost-effective materials. Which would make batteries more accessible [5].

As stated previously, for emerging battery technologies to be economically viable and competitive against traditional ones, they must use readily available materials and be cost-effective. Figure 4a provides insight into the abundance of elements in the earth's crust, which are specifically used in halide solid state electrolytes. Here it is clearly visible that material availability varies considerably. Comparing active materials, lithium and sodium, Li is more scarce with 20 mg/kg then Na with 23600 mg/kg. This is one of the reasons for research into sodium-ion batteries. Considering metals there is a huge difference in abundance. Titanium, for instance, is the most abundant metal with 5650 mg/kg followed by zirconium with 165 mg/kg. Additionally, metals like yttrium, niobium, and indium exhibit varying levels of availability, with 33 mg/kg, 3 mg/kg and 0.25 mg/kg respectively. Lastly, the abundance of halides also differ from each other with fluoride (585 mg/kg), chloride (145 mg/kg), bromide (10 mg/kg), iodide (0.45 mg/kg) and sulfide (350 mg/kg). Additional information regarding the abundance of all elements and of abundance of metals in solid electrolytes can be found in Figure A.1.

In general, looking at Figure 4b, elements that are less abundant tend to have higher prices. But interestingly, material prices don't always align with the natural abundance of an element. For example, despite yttrium (Y) being more abundant then europium (Eu) the price difference is very similar. This might be due to the difficulty of material extraction or their use in global industries.

Since abundance and price of materials can affect the viability and cost-efficiency of battery production, a careful selection of materials is crucial [24]. From a paper from Hu et al. the material cost of a solid electrolyte should not exceed 50 USD/kg in order to be a commercially viable electrolyte [16].

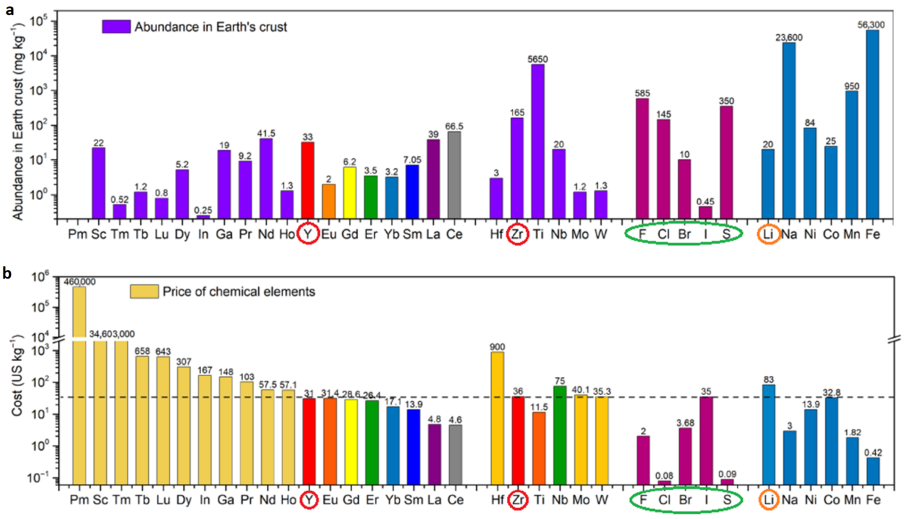

Figure 4: (a) Abundance of elements in the earth's crust used for halide solid state electrolytes [24], (b) Price per element in USD/kg [24].

In this project, the oxyhalide $Li_{2x}ZrCl_4O_x$ is prepared with precursors $ZrCl_4$ and Li_2O. Compared to other metals, zirconium (Zr) is an abundant metal with 165 mg/kg in the earth's crust. This abundance is particularly clear when compared with other raw materials used in the synthesis of chloride-based solid electrolytes (see Figure A.1). Besides titanium (Ti) the closest metal in abundance is cerium (Ce) with 66.5 mg/kg.

Commercially zirconium is derived from zircon ($ZrSiO_4$) and undergoes a chemical reaction to obtain $ZrCl_4$ as shown in the following reaction.

$$ZrSiO_4 + 2C + 4Cl_2 \Rightarrow ZrCl_4 + SiCl_4 + 2CO_2 \tag{4}$$

$ZrCl_4$ hosts multiple advantages, particularly its wide use in industrial areas (≈1 Mton produced per year[25]). Figure 5 presents a comparison of cost per kg for all precursors employed in chloride-based electrolytes. It is clear that $ZrCl_4$ is by far the cheapest with 12.5 USD/kg followed by YCl_3 with 320.3 USD/kg [26]. Another research paper estimated $ZrCl_4$ to cost 8.1 USD/kg [27].

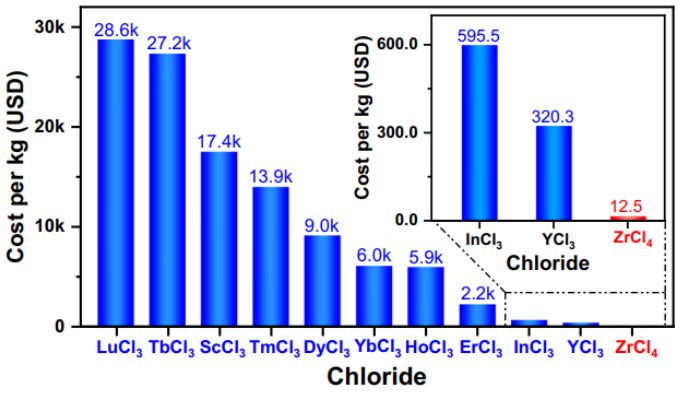

Figure 5: Estimated prices for chemicals used in chloride solid state electrolytes in USD/kg [26].

Li_2O is used in niche applications such as pharmaceuticals or nuclear reactors. Lithium oxide can be produced in a rather simple reaction pathway. Commonly it is formed by burning Li metal in air at temperatures above 100°C (see reaction 5). As of September 2023, in Sigma Aldrich, 100g of Li_2O costs 535 euros. But this may not accurately reflect real-world pricing since it has a very limited range of applications. Especially since Li_2O can be prepared from cheap chemicals such as Li_2CO_3, LiOH, and their hydrates [16].

$$4Li + O_2 \Rightarrow 2Li_2O \tag{5}$$

However, a lithium shortage is anticipated by 2025 since it takes 16.5 years to start operation in a new lithium mine and the demand is increasing drastically. Also lithium reserves are heavily concentrated in a small number of countries, with 80% of these reserves located in China [5]. Therefore, it can be beneficial if the electrolyte does not heavily rely on lithium.

In this first research project, the focus is on investigating the oxyhalide electrolyte $Li_{2x}ZrCl_4O_x$. To gain insights, it is interesting to compare this with a similar composition described in literature. In a study by Hu et al., they synthesized $Li_{1.75}ZrCl_{4.75}O_{0.5}$ using Li_2O, $ZrCl_4$, and LiCl. They estimate their electrolyte to cost 11.60 USD/kg which is significantly below their claimed 50 USD/kg threshold needed for commercial viability. This exhibits the promise of $Li_{2x}ZrCl_4O_x$ as a cost-effective electrolyte option.

Considering the mixed halide electrolyte examined in this second project, the abundance of yttrium is slightly lower at 33 mg/kg. Additionally, the estimated cost for the Zr-based oxyhalide with Li_3YCl_6 is approximately 196.31 USD/kg [16]. While this cost is higher than that of the Zr-based electrolyte, it remains significantly cheaper than other researched halide solid electrolytes.

1.4 Ionic conductivity in batteries

Electronic and ionic conductivity are important parameters in a battery. The basic principle in a battery is the transport of charged particles between the anode and cathode. The ionic conductivity is governed by the Li-ions that move through the electrolyte and the electronic conductivity is mostly relevant at the electrodes.

1.4.1 Activation energy and bottleneck

Ionic conductivity is responsible for the charge and discharge rate, capacity and cycling stability. Conductivity is based on diffusion of ions which involves ions hopping from one structural position to a neighboring one (see Figure 6). This diffusion is controlled by temperature, which follows an Arrhenius

behavior (which represents the reaction rate through the activation barrier). Additionally, temperature affects ion jump rates and jump distances. This jump rate is also dependent on the crystal structure and size.

The activation energy (E_a) represents the minimum energy required for a reaction to occur. In the context of solid electrolytes, E_a refers to the energy required to create mobile defects (E_f) and to the highest energy barrier that ions must overcome to migrate through the solid electrolyte (E_m) [28]. See Figure 6a for an illustration of the energy needed for an ion to migrate through the solid by direct vacancy hopping. The importance of activation energy is with its relation towards the ionic conductivity. As in theory, with lower E_a the mobility of ions and ionic conductivity increases [29].

The activation energy is dependent on the Arrhenius equation. The Arrhenius equation defines the temperature dependence of conductivity. This results in the following equation 6. Where σ is the electrical conductivity (S/cm), σ_0 is the pre-exponential factor (S/cm), Ea is the activation energy (eV), R is the gas constant (8.3145 J/mol) and T is the absolute temperature (K) [30].

$$\sigma = \sigma_0 \cdot e^{-\frac{E_a}{R \cdot T}} \tag{6}$$

The pre-factor can be further computed with the equation 7. Where z is the geometrical factor, n is the charge carrier concentration and q is charge of diffusing ion. ΔS_m represents the entropy of the diffusing ion and k_B the Boltzmann constant. Lastly, a_0 is the jump distance, and v_0 the attempt frequency [29].

$$\sigma_0 = \frac{zn(q)^2}{k_B} \cdot e^{\frac{\Delta_{S_m}}{k_B}} \cdot a_0^2 v_0 \tag{7}$$

The oscillatory frequency v_0 can be written in terms of activation energy, lithium concentration and the jump distance.

$$v_0 = \frac{1}{a_0}\sqrt{\frac{2E_A}{M_{Li}}} \tag{8}$$

As introduced, an important parameter for E_a is the migration energy (E_m). The E_m is tied to the resistance encountered within the host structure of the migrating ions. This energy barrier is often also referred to as the bottleneck. This bottleneck can be pictured as the area spanned by neighboring atoms in a crystal structure [31]. Figure 6b provides an illustration of this bottleneck, where the red ball symbolizes an ion migrating through a crystal structure [28].

The modification of bottleneck size has a direct impact on activation energy and, consequently, ionic conductivity. By altering the lattice volume and ionic size a change in activation energy can be seen. The diffusion coefficients of different mobile monovalent ions can vary significantly in the same crystal structure. Consequently, the optimal bottleneck size for a specific ion leads to the highest diffusion coefficient and the lowest activation energy. This phenomenon occurs because ions with a larger ionic size are blocked from traversing through the bottleneck, whereas ions that are too small may become trapped in the local energetic minima. Therefore, adjusting the bottleneck size can lead to lower activation energies and can be achieved through complete or partial substitution of atoms inside the host lattice with larger atoms. For these reasons, ensuring an optimal bottleneck size is crucial to minimizing activation energy and maximizing ionic conductivity [28, 31].

The defect formation energy (E_f) is another factor influencing the activation energy. It determines the presence of interstitials, vacancies, and occupancy in lattice sites. Additionally, substitution of aliovalent cations can create more interstitials and vacancies influencing the ionic conductivity [28].

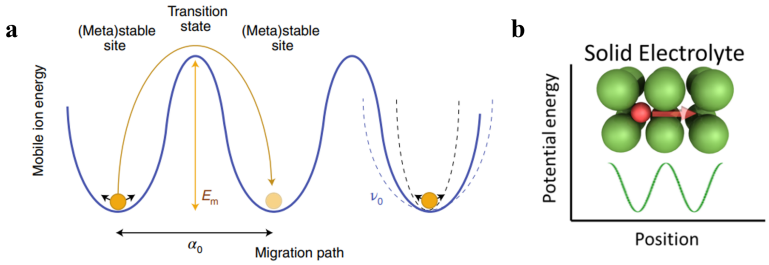

Figure 6: (a) Energy barrier for ion hopping through direct vacancy mechanism [29] and (b) an illustration of a mobile ion in a crystalline solid [28].

1.4.2 Types of conductivity mechanisms

Ionic diffusion can be one-, two- or three dimensional meaning the Li^+ ions diffuse in a line, plane or in all directions. There are two types of ion diffusion that are relevant for solids: vacancy/defect and non defect mechanisms [32]. The type of diffusion mechanism depends on the crystal structure. For **defect** driven mechanisms two distinct types exist: vacancy and divacancy. In vacancy mechanism an ion jumps to a neighboring vacancy that is an atomic defect in the crystal or metal (see Figure 7a). Divacancy mechanism is the jumping through a group of vacancies [33].

For **non defect** driven mechanisms, there are four distinct processes: direct interstitial, collective, interstitialcy and interstitial-substitutional exchange. The direct interstitial mechanism of ion diffusion occurs when ions or atoms move within a crystal lattice through occupying interstitial sites (see Figure 7b). These interstitial sites are small empty spaces or voids between regularly arranged lattice sites of the host crystal structure. Therefore, the ion should be smaller than the host atom's interstitial sites to not change the lattice structure. Collective diffusion is a mechanism where particles interact with each other and the motion of one particle is influenced by the positions and motions of neighboring particles. This collective mechanism is a common mechanism in amorphous systems (see figure 7c). Interstitialcy is similar to direct interstitial mechanism but involves interstitial atoms with sizes similar to those of lattice atoms. The diffusion occurs by the interstitial atom being displaced by a lattice atom which then can displace another lattice atom and so on. The diffusion occurs through atoms moving by jumping into and out of interstitial sites within the crystal structure (see Figure A.3) [33].

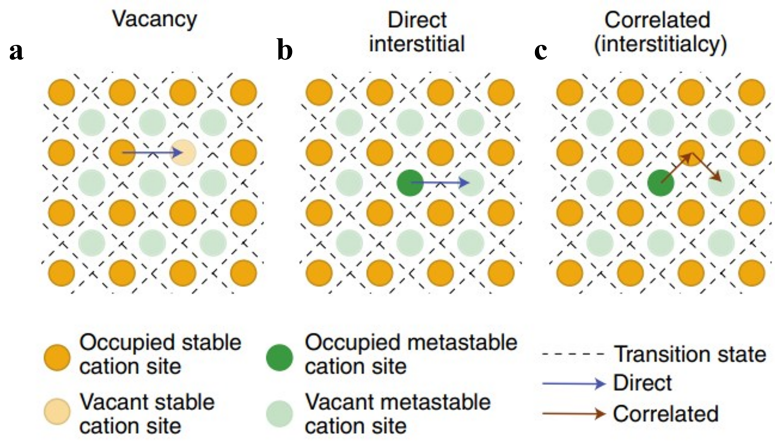

Figure 7: Different ionic diffusion mechanisms in a solid [29].

1.4.3 Conductivity in Li-ion batteries

In lithium-ion batteries, generally the main diffusion mechanism at the electrodes is vacancy diffusion. This occurs because lithium vacancies are created in the electrode upon the charging and discharging process of the battery [34]. Considering the electrolyte, as a liquid, the Li^+ ions have a long diffusion distance due to their interaction with the electrolyte, forming a complex with the electrolyte. Instead, in solid state batteries the Li^+ ions employ a hopping mechanism to diffuse through the electrolyte [35].

The diffusion mechanism, in halide solid electrolytes, mostly relies on vacancies or interstitials depending on the obtained crystal structure [36, 37, 38]. For example, in materials such as Li_3YCl_6 and Li_3YBr_6, diffusion occurs through Li-ion hopping in octahedral sites through existing vacant sites with a low energy barrier [38]. The reason behind halides being able to conduct Li^+ is due to the weak bonding of the monovalent (meaning only one valency e.g. Br^-) halide anion with Li^+ that result in a low energy barrier [37].

Ionic conductivity in liquid electrolytes are usually 10^{-3} to 10^{-2} S/cm (1 to 10 mS/cm) while in solid state batteries these are often around 10^{-3} S/cm (1 mS/cm) [39].

1.4.4 Electronic conductivity

Electron conductivity is important within electrodes because electrons need to be provided or withdrawn rapidly from these in order to allow for efficient charging and discharging of the battery. To ease this process current collectors are added to the electrodes, usually aluminium foil (Al) for the cathode (not needed in SSBs) and copper (Cu) for the anode [40].

However, in electrolytes, electron conduction is undesirable and should be negligible due to dangers of explosions and dendrite formation leading to short circuiting of the cell [41]. An electrolyte is electronically insulating for values around 10^{-11} S/cm [22].

1.5 Electrochemical stability

The electrochemical stability window (ESW) is defined as the voltage range between the oxidation potential (E_{ox}) and the reduction potential (E_{red}). Meaning that a material won't undergo any chemical reaction and remain stable. The ESW is an important parameter since it influences the energy density and durability of the battery. In the context of solid-state batteries, the solid-state electrolyte material must exhibit stability at high potentials vs Li^+/Li and be compatible with high-voltage cathode materials like NMC ($LiNiMnCoO_2$) which operates in the range of 4.2V [42].

One common method to analyze the ESW is through Linear Sweep Voltammetry (LSV). This technique involves a material being subjected to a controlled voltage sweep from a lower potential to a higher potential at a constant scan rate (mV/s). The resulting current is then measured as a function of time. The aim is to understand at what potential a material is degraded through oxidation or reduction [43].

The calculated electrochemical stability windows of Li-M-X solid electrolytes, where M represents the metal cation and X represents fluorides, chlorides, bromides, iodides, oxides, sulfides, and nitrides, exhibit substantial variations in their range of stability. These variations are shown in Figure 8.

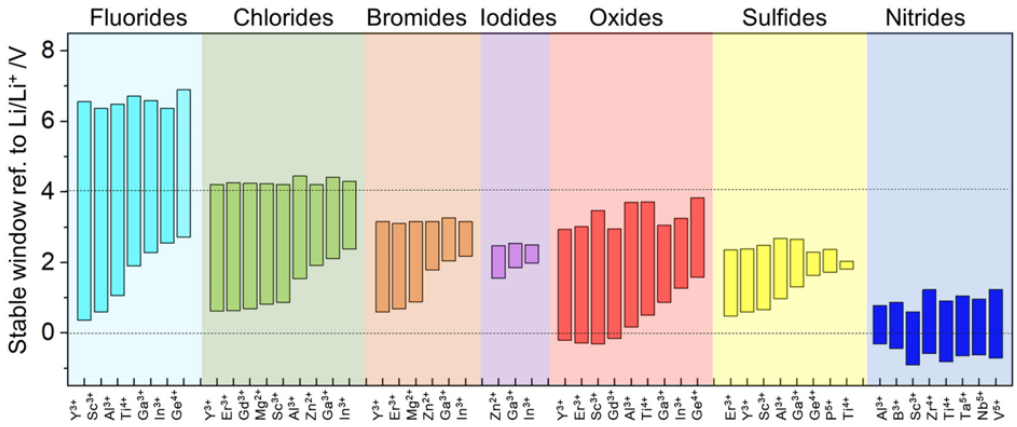

Figure 8: The calculated electrochemical stability window of different solid-state electrolytes[27].

Specifically, nitride, sulfide, and iodide-based electrolytes have very narrow stability windows. To provide some specific examples: nitride span around -0.2 to 0.8 V bounded with Al^{3+}, sulfide around 0.5 to 2.4 V integrated with Sc^{3+}, and iodide 1.5 to 2.5 V with Ga^{3+}. While, fluorides exhibit a much broader stability range, ranging from 1.1 to 6.5 V incorporated with Ti^{4+}. Chlorides and oxides also present reasonably broad windows, for instance, 0.75 to 4.2 V for chloride with Gd^{3+} and -0.1 to 3 V for oxide with Y^{3+}. Bromides fall in between, spanning from 0.8 to 3.1 V with Mg^{2+}.

Electrochemical stability windows are different when mixed with different elements. Therefore, tuning of the stability window is possible through doping with different elements [24].

1.6 Crystal and amorphous structures

Crystallinity referes to the arrangement of atoms or ions in a material's structure. The structure can have a significant impact on ionic conductivity. There are two different types of structural ordering of atoms: crystalline and amorphous. The crystalline structure is a highly ordered and repeating arrangement of atoms or ions. Due to this ordering a distinctive pattern can be observed upon exposure to x-rays and the specific structure can be identified. Amorphous structures have a disordered arrangement and their patterns cannot be defined under exposure of x-rays [44].

1.6.1 Crystal systems

Crystalline structures can be categorized into specific groups with the help of "unit cells". A unit cell is the smallest repeating unit in a crystal structure. Meaning that only by using the unit cell you can replicate the entire crystal structure. A unit cell is composed of six parameters, with the length of the cell edges (a, b, c) and the angles between them (α, β, γ). The different unit cells are cubic, tertragonal, orthorhombic, monoclinic, hexagonal, rhombohedral and triclinic as seen in Figure 9 [44].

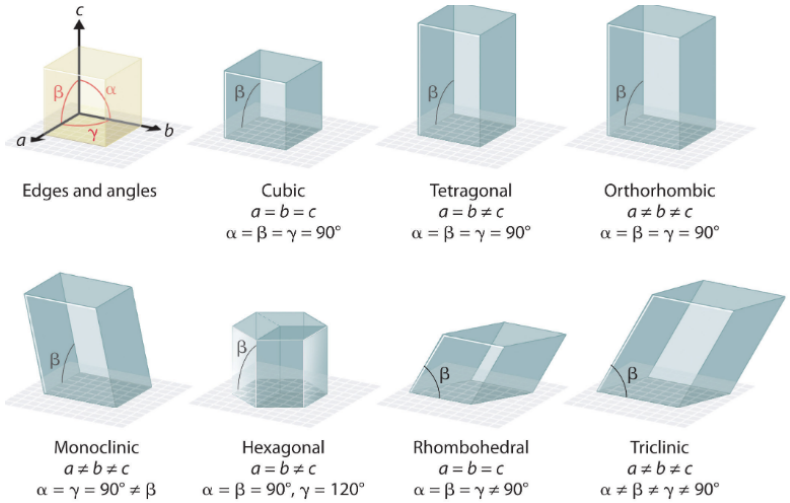

Figure 9: Seven basic unit cells [45].

Bravais lattices

In a unit cell, the atoms can be positioned in different ways, which is further classified through Bravais lattices. The simplest example is the cubic system (see Figure 10). If the atoms are only on the corners of the cube it is a simple cubic. If an extra atom is positioned at the center of the cube, it is termed body-centered cubic (bcc) and when additional atoms are located in the centre of each face the structure is a face-centered cubic (fcc). In total there are 14 different Bravais lattices [44].

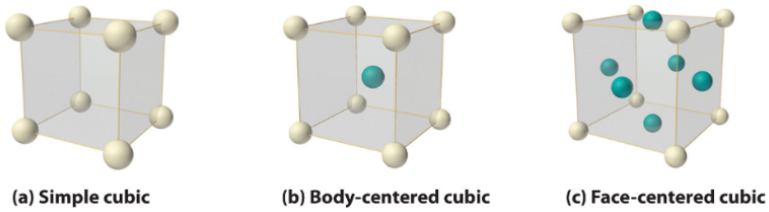

Figure 10: Cubic structures [45].

Space groups

Lastly, space groups describe the different symmetry operations that leave a crystal's structure unchanged. There are 230 different space groups. Space groups are denoted by numbers and letters, such as "C2/m" or "P3m1". These symbols describe the precise symmetry operations and arrangements of atoms or ions within the unit cell.

Close packing arrangements

Close packing arrangements refers to a way in which atoms or ions, can be arranged to efficiently occupy space. The two most common types of close packing are hexagonal close packing (HCP) and cubic close packing (CCP). This is also the case for chloride electrolytes (Li_3MCl_6) [24].

The HCP structure is characterized by hexagonal base structured layers (see Figure 11). Each particle in a layer is surrounded by six neighboring atoms, forming a hexagonal pattern. The overall structure has a repeating ABAB pattern, meaning that consecutive A and B layers align exactly with previous

layers. This layered structure results in a hexagonal close packed structure. In contrast, CCP has a very similar structure as HCP, however, instead of a repeating A layer, a C layer is introduced. CCP follows an ABCABC repeating structure which results in a cubic close packing arrangement.

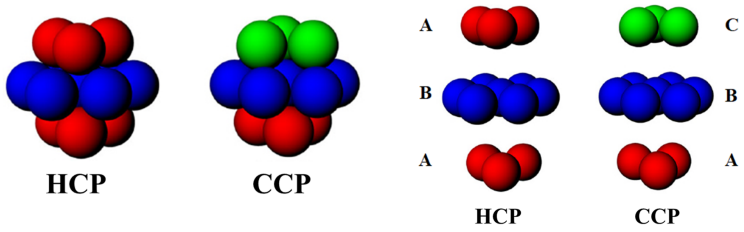

Figure 11: Hexagonal and cubic close packing structures [46].

C2/m and P3m1 structures

An example of crystal structures relevant in this report are P3m1 and C2/m. The letter "P" in P3m1 defines the crystal system. This means it is a primitive (simple) structure where all atoms are on the edges. The "3" refers to the Bravais lattice and belongs to the hexagonal lattice type. And lastly, "m1" concerns the space group with a specific symmetry.

For C2/m it is the same concept. The "C" stands for monoclinic structure, "2" represents base-centered lattice and "/m" is a specific symmetry.

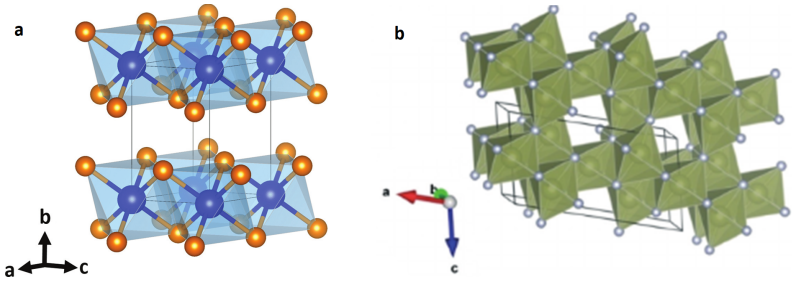

Figure 12: (a) P3m1 structure [47], (b) C2/m structure [48].

1.6.2 Amorphous systems

Advantages and challenges

Amorphous structures are defined as solids that lack long rage ordering in their atomic arrangement [49]. Solid electrolytes that show amorphous structuring have several advantages. They are usually softer materials with fewer grain boundaries which allows ions to move more freely and contributes to enhanced conductivity. Additionally, amorphous powders are typically easier to fabricate. Also the absence of a regular crystal lattice in amorphous materials promotes ion transport through a hopping mechanism, where ions move in a more random way between different sites. This random movement can facilitate ion mobility and increase overall conductivity.

Amorphous solid electrolytes can address some of the challenges associated with crystalline solid electrolytes, such as high grain boundary resistance, limited processability, and higher production costs. It has, however, been observed that amorphous powders generally posses a lower ionic conductivity compared to crystalline solids [50].

Amorphous structure through ball milling

Ball milling can be employed to achieve amorphous structures. Ball milling is an alternative method for producing solid state electrolytes. It involves grinding solid materials using balls within a jar at high speeds. During this process, the energy from the collisions of the balls is converted into chemical energy, leading to structural changes in the powder material [51]. Several parameters in the ball milling process can be adjusted, including the ball-to-powder ratio, the type of ball mill jars and balls, the surrounding atmosphere (e.g., O_2, N_2, H_2, or vacuum), ball milling duration, and rotational speed. This room temperature synthesis technique offers several advantages. It is cheaper and requires less energy, especially when compared to high-temperature synthesis methods. Therefore, it is an interesting technique to apply for large scale production [52].

With longer times of high-energy ball milling an amorphous structuring becomes increasingly prevalent. As with high-energy ball milling, particles accumulate mechanical energy. And at a critical point, this energy can cause mechanical deformations such as cracks, and particle breakage due to lattice strain, leading to the formation of new structures and amorphization. As a result, particle size decreases, and disorder within the material increases. This increase in disorder provides more opportunities for ions to move freely within the material, ultimately leading to higher conductivity [53, 54]. X-ray diffraction (XRD) analysis has revealed that amorphization starts when particles reach a critical size and microstrain decreases. Additionally, increasing ball milling time often leads to peak broadening in XRD data, indicating the start of the amorphization process [55].

It is important to note that the solid material can change structure back to crystal with high mechanical energy when a lot of heat is generated [55]. These produced structural phases are usually different from the ones produced with thermal treatment [51].

Challenges in understanding amorphous structure

One of the challenges associated with amorphous structures is their lack of long-range ordering, as previously mentioned. Therefore, understanding the ionic conductivity mechanisms in amorphous solid electrolytes can be quite challenging. Currently, there are only a few available theories for modeling their structure and predicting their conductivity [50].

1.7 Solid electrolytes

As previously stated, electrolyte allows ions to flow between the positive and negative electrodes. This principle is the same for solid and traditional liquid electrolytes. Therefore, the solid-state battery is based on the same principle as traditional liquid-state batteries [12]. Thus, while charging, Li-ions undergo deintercalation from the cathode and pass through the electrolyte and the interfaces between the electrolyte and the electrodes to reach the anode. At the same time, electrons migrate from the cathode to the anode through the external circuit, completing the electrical circuit. In the discharge process, this movement of Li-ions and electrons is reversed [12]. Many different groups of solid electrolytes are currently being researched such as NASICON, garnets, perovskites, LISICON, LiPON, Li_3N, sulfides, argyrodites, oxides and halide electrolytes[12].

In this thesis project the solid oxyhalide electrolyte $Li_{2x}ZrCl_4O_x$ (with X = 0.25, 0.5, 1 and 1.5) and solid halide electrolyte $Li_3YCl_3Br_{3-x}I_{1-x}$ (with X = 0, 0.2, 0.4, 0.6, 0.8 and 1) are investigated. Therefore, in this chapter properties of halide and oxyhalide electrolytes will be presented along with sulfide and oxide electrolytes to compare with.

A general spider plot is shown in Figure 13 of properties of sulfide, halide and oxide electrolytes. It is clear that each electrolyte has their advantages and disadvantages.

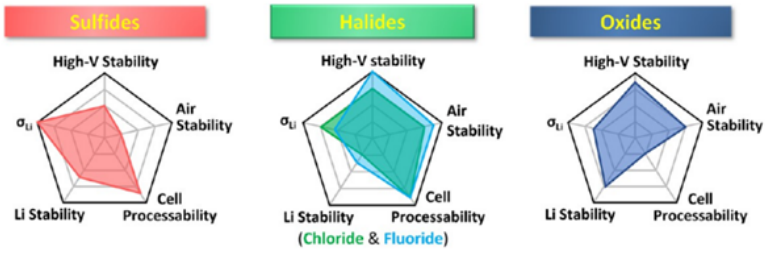

Figure 13: Spider plot of electrolyte performance of sulfide, halide and oxide electrolytes [27].

1.7.1 Oxide and sulfide solid electrolytes

Oxide electrolytes are being researched for exhibiting a decent stability in atmospheric air and its great electrochemical stability window (ESW). For example, $Li_{1.3}Al_{0.3}Ti_{1.7}(PO_4)_3$ has ESW of 2.17-4.21 V, and $Li_{0.33}La_{0.56}TiO_3$ an ESW of 1.75-3.71 V. They are typically paired with, 4V $LiCoO_2$ cathode. Current bottlenecks, however, are the mediocre ionic conductivities (e.g., 0.1 mS/cm for $Li_7La_3Zr_2O_{12}$ and 1 mS/cm for $La_{\frac{2}{3}-x}Li_xTiO_3$) [56], poor mechanical properties and poor ionic contacts with electrodes (due to its brittleness) resulting in large interfacial impedances and issues in cell processability [27, 57, 58].

Sulfide electrolytes on the other hand show great ionic conductivity with $Li_{10}GeP_2S_{12}$ and $Li_{9.54}Si_{1.74}P_{1.44}S_{11.7}Cl_{0.38}$ exhibiting ionic conductivities of $\sigma > 10$ mS/cm which is comparable to traditional liquid electrolytes [56]. They also hold a high mechanical sinterability which is advantageous for cell production in solid-state batteries. This is a process where powder is heated to a temperature below their melting point but high enough to promote bonding between particles, this results in the formation of a denser and more cohesive solid material.

The main challenge of sulfide electrolytes is their narrow electrochemical stability window, with oxidation of S^{2-} occurring at 2.5 V and known electrolytes $Li_{10}GeP_2S_{12}$ (LGPS) and Li_3PS_4 operating between 1.72-2.29 V and 1.71-2.31 V respectively [22, 27]. This prevents it from being used with high energy density electrode materials that can deliver more capacity per unit of voltage. Additionally, sulfides have a low chemical stability in air and when exposed to moisture, they react with water to create hydrogen sulfide gas which is colorless, highly flammable and highly toxic [27, 59]. Some sulfide electrolytes also rely on rare metals such as Ge which are expensive and not abundant [14].

1.7.2 Halide electrolytes

Advantages

Halide electrolytes are another type of recently emerging solid state electrolytes which previously received little interest due to low ionic conductivities. This changed in 2018, however, with the published work of Asano et al. on chloride (Cl) and bromide (Br) based electrolytes namely Li_3YCl_6 and Li_3YBr_6. They discovered these electrolytes exhibit decent Li^+ ion conductivity of 0.51 and 1.7 mS/cm respectively, which sparked a new wave of research in this field [13]. Since then halide electrolytes are regarded as the electrolyte that holds both advantages of oxide and sulfide electrolytes due to its potential for high ionic conductivity, wide electrochemical stability window, high deformability, potential partial air and moisture stability and more cost effective [60].

Classification

The halide group consists of fluoride (F^-), chloride (Cl^-), bromide (Br^-) and iodide (I^-). They differ in properties such as electronegativity, F > Cl > Br > I with 4.0 > 3.0 > 2.8 > 2.5 respectively and ionic radii

which are larger than oxide and sulfide anions (r_{F^-} = 136 pm, r_{Cl^-} = 167 pm, r_{Br^-} = 182 pm, r_{I^-} = 202 pm) [24].

Halide electrolytes can be categorized into three different groups namely: 1) containing group 3 elements e.g., scandium (Sc) and yttrium (Y) , 2) containing group 13 elements e.g., aluminium (Al) and indium (In), and 3) those with divalent metals e.g. Fe^{2+} [27]. Group 3 and 13 based halide electrolytes have the general formula Li_3MX_6, with M being a metal (M = In, Y, Sc, or Er) and X = F, Cl, Br or I [61]. However, the amount of Li and type and amount of metal/halide can be tuned.

Crystal structures

The structural variations in halide electrolytes depend on the sizes of the cations and the specific ionic radii of the M^{3+} ions. For chloride electrolytes (Li_3MCl_6) there are two potential anion sublattice arrangements: hexagonal close packing (hcp) and cubic close packing (ccp). These arrangements can be categorized into three distinct space groups [24]:

1. Trigonal structure (space group: P3m1): This structure emerges with M^{3+} ions with large ionic radius (ranging from 102 to 106.4 pm, e.g., Tb^{3+}). The M^{3+} ions are situated in these octahedral positions.
2. Orthorhombic structure (space group: Pnma): This structure appears when M^{3+} has ionic radius in the range of 100-102 pm (e.g., Y^{3+} with 101.1 pm). The M^{3+} ions usually sit in the octahedral sites.
3. Monoclinic structure: The structure has an ABCABC stacking and appears with an M^{3+} with ionic radius >100 pm (e.g., In^{3+} and Sc^{3+}). The M^{3+} are also located in the octahedral site.

For chloride based electrolytes the monoclinic phase shows the highest conducivity followed by the orthombic phase and lastly the trigonal phase [24].

In contrast, as discussed in the review paper of Wang et al., bromide (Li_3MBr_6) and iodide (Li_3MI_6) based electrolytes exhibit only monoclinic structures for which high ionic conductivities is expected. However, there have been few bromide and iodide based electrolytes that have had a higher ionic conductivity [24].

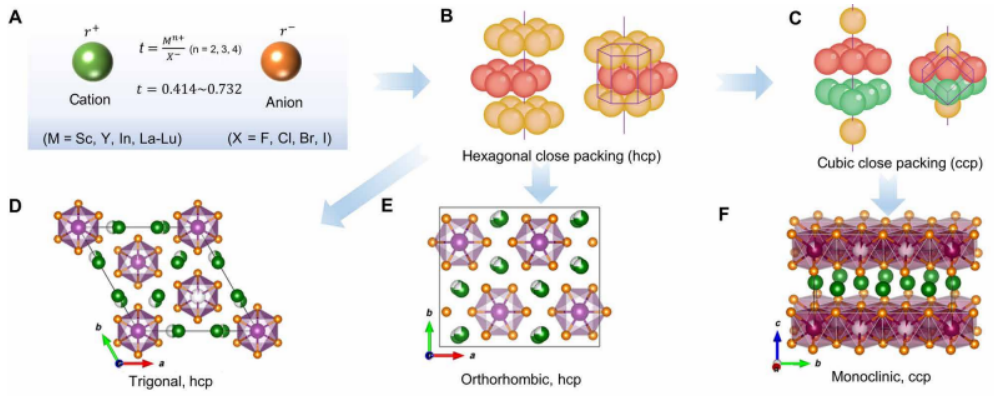

Figure 14: The crystal structure of halide solid electrolytes [24].

Synthesizing method

An effective method to synthesize halide electrolytes can be through ball milling resulting in amorphous or low-crystallinity powders with a narrow particle size distribution. Post-annealing can be used to further reduce crystallinity and improve properties [24].

Ionic conductivities

Ionic conductivity in halide electrolytes varies with the selection and combinations of central metals and halides. In Figure 15, conductivities of various halide electrolytes is shown with its respective space group. It seems the monoclinic structure exhibits the highest conductivities. For example, $LiScCl_6$ has a conductivity of 3.02 mS/cm. The highest conductivity is $Li_3YBr_3Cl_3$ which reaches 7.2 mS/cm but this performance is attributed to hot pressing, a process involving high temperature and pressure that reduces grain boundary resistance [24]. Additional conductivities and structure of halide electrolytes are shown in appendix Figure A.2 with comparison of sulfide and oxide electrolytes.

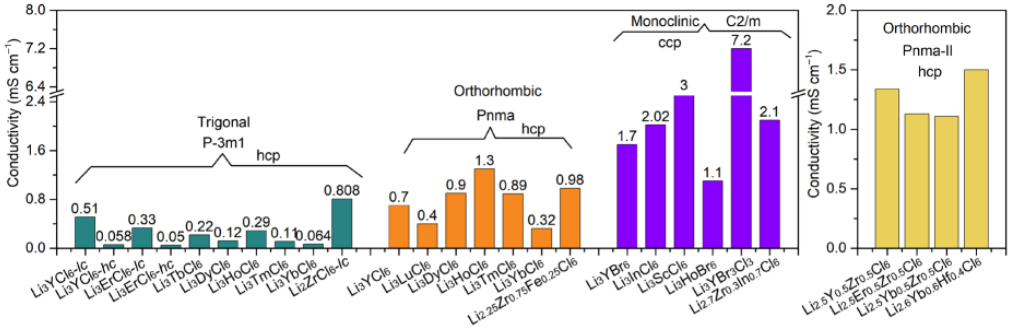

Figure 15: The conductivity of halide solid electrolytes [24].

Electrochemical stability window

Halide electrolytes exhibit wide electrochemical stability windows, as illustrated in Figure 8. Among the various halides, fluorides have the broadest electrochemical window, followed by chlorides, bromides and iodides. This can be attributed to the difference in electronegativity of the halides, as mentioned earlier. For instance, Li_3YCl_6 and Li_3YBr_6 have cathodic limits of 0.59 and 0.62 V and anodic limits of 3.15 and 4.21 V respectively.

Interestingly, it is possible to modify the reduction potential through doping or changing the metal cation, and modify the oxidation potential by doping or substituting the halide [24]. An example of this is with fluoride-doped electrolyte, $Li_3InCl_{4.8}F_{1.2}$, which has a stability up to 4.3 V that surpasses Li_3InCl_6 [27]. Among the halides discovered so far, fluoride and chloride electrolytes are compatible with cathodes operating in the 4V voltage class [22, 26].

Halide electrolytes possess high deformability, enabling more efficient processing. They also exhibit an improved air and moisture stability compared to sulfides. Lastly, they can be cost effective by utilizing less scarce materials [27, 62].

Current challenges

Some challenges with halide electrolytes are that they often rely on rare earth metals as central elements, resulting in high raw material cost, they are not stable with Li-metal anodes, and they are also sensitive to moisture [24, 60].

The frequent usage of rare earth metals (e.g., scandium) poses an issue due to their high cost and are less abundant in the earth crust. This limits the large scale use of such electrolytes in batteries [24].

The unstability of halide solid electrolytes with Li-metal is due to the lithium ions reacting with the halide ions creating an unstable layer (see equation 9) [24]. Currently a buffer layer is placed between the halide electrolyte and anode. The anode used is an indium and lithium metal alloy since indium metal does not react with sulfide electrolytes. Additionally the new interface between the sulfide and halide layers do not seem to influence the ion transport [27, 63]. However, Indium/lithium alloys have drawbacks, including lower energy density and capacity compared to pure lithium, increased manufacturing complexity, and

higher costs due to the use of Indium. The sulfide layer also lowers the energy density and requires one more step in the manufacturing.

$$Li_3MX_6 + 3Li \Rightarrow 6LiCl + M(M = In, Yetc.) \tag{9}$$

Promising halide electrolyte

Currently, a promising halide electrolyte is Li_2ZrCl_6 which is based on the cost-effective and abundant zirconium metal. The measured conductivity is decent with 0.81 mS/cm, it seems to have some air stability and it is compatible with 4V cathodes. The oxidation reaction is around 3.7 V vs Li/Li^+ [26, 64].

Another electrolyte is yttrium (Y^{3+}) based and exhibits the highest conductivity amongst halide electrolytes (5.36 mS/cm for $Li_3YBr_{4.5}Cl_{1.5}$). They also have the advantage of tunability of both conductivity and stability [65].

1.7.3 Oxyhalides

Promise of $LiTaCl_5X^{n-}_{1/n}$

A research paper made by Ishiguro et al. conducted an investigation into a novel category of halide electrolytes known as glass lithium solid electrolytes, specifically focusing on $LiTaCl_5X^{n-}_{1/n}$ where X^{n-} represents F^-, Cl^-, Br^-, I^-, O^{2-}, OH^-, O^{2-}, or S^{2-}. They reported remarkably high conductivities, reaching up to 10.95 mS/cm at a temperature of 25°C. Additionally, these electrolytes exhibited a high electrochemical stability voltage of up to 4.8 V, an ultrahigh loading exceeding 7 mAh/cm^2, and a capacity retention rate of 92.81% after undergoing 200 cycles. Specifically, the chloride-based electrolyte, $LiTaCl_5O_{0.5}$ which is synthesized through mixing of $TaCl_5$, Li_2O and LiCl is of interest in this report due to its conductivity of 8.92 mS/cm [58].

The authors attributed these performances due to strong physical contact, facilitated by the materials' deformability and the absence of grain boundaries. Furthermore, the electrolytes are in the glass phase as no crystalline peaks are observed in the XRD plots (see Figure 16a). They claim that compared to their crystalline counterparts, this amorphous structure improves ionic conductivity since more space is available for Li-ions to move. Additionally, they claim that the high ionic conductivities and good contact between the cathode and electrolyte can minimize the inner resistance in the whole battery, which might be very advantageous for use in the battery sector [58].

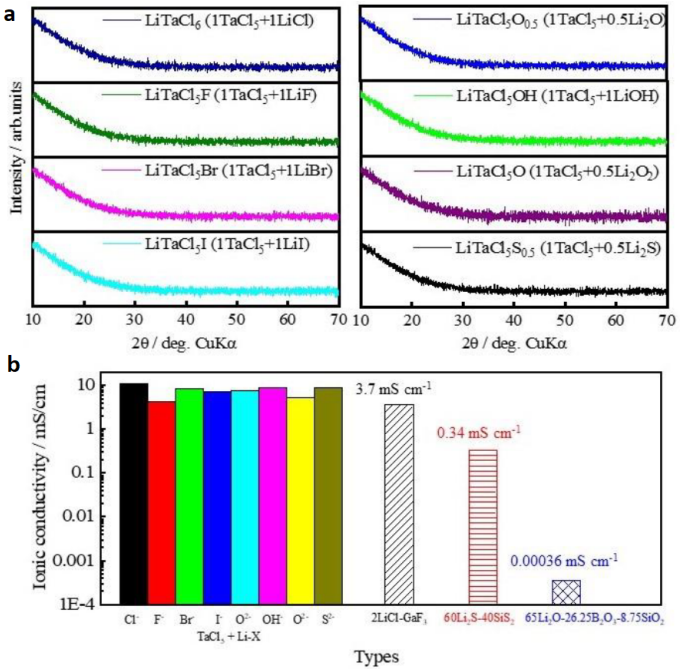

Figure 16: (a) XRD patterns of $LiTaCl_5X^{n-}_{1/n}$ (X^{n-}=F^-, Cl^-, Br^-, I^-, O^{2-}, OH^-, O^{2-}, S^{2-}), (b) comparison of ionic conductivities of $LiTaCl_5X^{n-}_{1/n}$ with typical halide, sulfide and oxide glass electrolytes [58].

However, this electrolyte type is not stable with Li-metal nor Li-In alloy anode since Ta^{5+} gets reduced. Therefore, a highly conductive protection layer is needed [58]. Additionally, Ta^{5+} is a very rare metal with an abundance of only between 0.2 ppm in earth's crust. Plus, it is almost nonexistent in its natural metallic state. This implies that it is not feasible to produce batteries on a big scale using $TaCl_5$ in the electrolyte [66].

Another research paper from Zhang et al. conducted further investigation on different compositions of xLi_2O-MCl_y, where M represents either Ta or Hf, with specific ranges for x and y ($0.8 \leq x \leq 2$ and y = 4 or 5). The amorphous solid electrolyte, $1.5Li_2O$-$HfCl_4$ achieves a conductivity of 1.97 mS/cm at 25 °C and a low activation energy of 0.328 eV. The tantalum-based electrolyte, xLi_2O-$TaCl_5$ (with $1.1 \leq x \leq 1.8$), exhibits high ionic conductivities, as seen in Figure 17b, of around 6 mS/cm with low Arrhenius activation energies ranging between 0.241 to 0.277 eV. This conductivity is lower then previously shown $LiTaCl_5O_{0.5}$ composition. Considering their electrochemical performances, they exhibit long cycle life. Especially for $1.6Li_2O$-$TaCl_5$ a capacity retention of 90.7% after 2400 cycles at 2C is observed. While $1.5Li_2O$-$HfCl_4$ exhibited a capacity retention of 89.6% after 300 cycles at 0.5C.

For both Hf and Ta based electrolytes, there is no need for coated cathodes due to their good compatibility with uncoated cathodes. However, they are not stable against anodes such as Li and Li/In metals as Ta^{5+} and Hf^{4+} will reduce.

They claim that the ionic conductivity is primarily coming from the chloride. Since chloride has a relatively large anion radius, large anion polarizability, and weak interaction with Li-ion. Additionally, the oxides contributed to forming the amorphous structure. This increase in disorder facilitates the escape of Li-ions from the structure and decreases the activation energy [50].

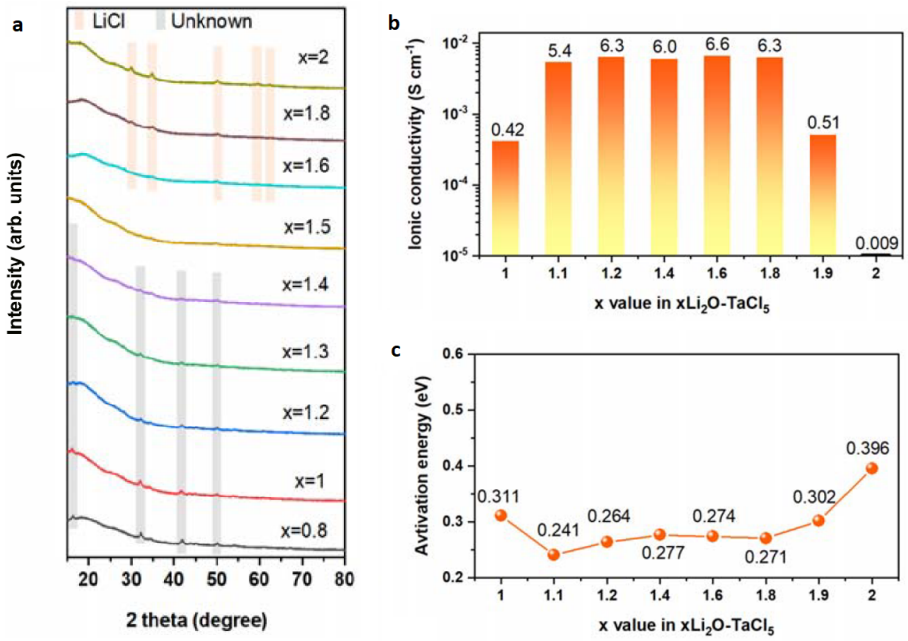

Figure 17: (a) X-ray diffraction, (b) conductivity and (c) activation energy results of different compositions of xLi_2O-$TaCl_5$ [50].

Promise of $Li_{2+x}ZrCl_{6-x}O_x$

Another important paper that was published by Hu et al. is based on the oxyhalides $Li_{2+x}ZrCl_{6-x}O_x$ and optimized composition $Li_{1.75}ZrCl_{4.75}O_{0.5}$ which are close to the oxyhalide investigated compositions in this project ($Li_{2x}ZrCl_4O_x$) [16]. The $Li_{1.75}ZrCl_{4.75}O_{0.5}$ electrolyte composition has shown good ionic conductivity with 2.42 mS/cm at 25°C and a good compressibility (94.2% density at 300 MPa) which is important for a good contact between electrolyte and electrode that should be above 90% when cold pressed. It is also almost free of cracks and pores. Importantly, the raw material cost is estimated at 11.60 USD/kg which is very cost competitive. Additionally it shows great electrochemical properties as the discharge capacity retention is 70.34% (capacity of 70.2 mAh/g) after 2082 cycles.

The $Li_{2+x}ZrCl_{6-x}O_x$ oxyhalide is ball milled at 600 rpm for 45 hours. Which gives rise to different structural phases for different compositions. The compositions with low oxygen content ($x \leq 0.25$) predominantly exhibit P3m1 symmetry while compositions with $x \leq 1.0$ mainly show C2/m crystal structure (as seen in Figure 18a). Interestingly, compositions between x is 0.5 and 0.75 display a coexistence of both phases and show significantly reduced crystallinity compared to the single phase structures. The coexisting phases exhibited crystallinity levels of less than 20%, with the majority of the structure being amorphous. In contrast, compositions with P3m1 phase have around 52% crystallinity (as observed in Figure 18b).

The study suggests that with increasing concentration of Li_2O precursor the crystallinity decreases. But at a specific concentration threshold, the structure approaches that of another crystalline compound, $Li_4ZrCl_4O_2$, resulting in increased crystallinity. Furthermore, the study reports a reduction in grain size of the coexisting two phases which is linked to the amorphization.

The conductivity of the most amorphous composition (x=0.5) is the highest with 1.17 mS/cm while the more crystalline compositions were lower. Therefore, they conclude that the contributor to this increase in conductivity is the amorphousness. The primarily P3m1, mixed phase and primarily C2/m structures have an effective migration barrier of 0.806, 0.748 and 0.411 eV respectively.

Considering the electrochemical stability, the oxyhalide electrolyte exhibits a reduction potential of 2.16

V vs Li/Li$^+$ compared to 1.79 V for Li_2ZrCl_6. This is odd since the metal cation, Zr^{4+} is the same for both electrolytes. They explain it could be due to the amorphousness of the compound or the anions it bonds with. The oxidation potential is 4.0 V vs. Li/Li+ compared to Li_2ZrCl_6 that oxidizes at 3.5 V [16].

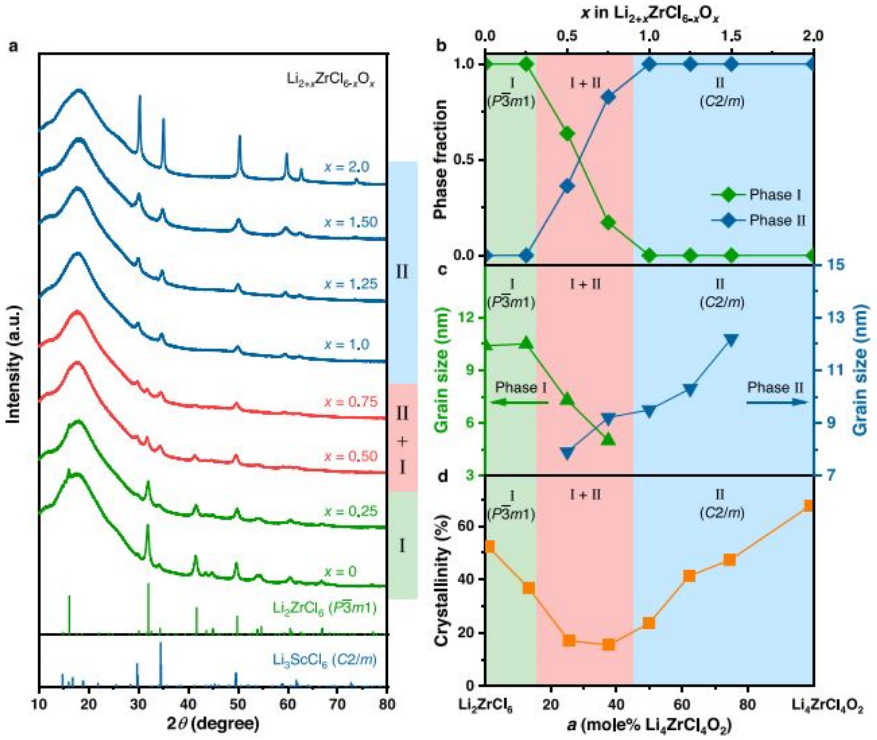

Figure 18: (a) X-ray diffraction and (b) phase fraction, grain size and crystallinity of different $Li_{2+x}ZrCl_{6-x}O_x$ compositions [16].

2

Characterization techniques

2.1 X-ray diffraction (XRD)

Theory

X-ray diffraction (XRD) is a characterization technique used to identify crystal structures of materials. Other useful information that can be found with XRD is phase information of material, and space group symmetry. The principle of XRD is based on the scattering of x-rays in crystals or molecules. X-rays have a similar wavelength with crystals and therefore will scatter in different directions. Since crystals have a repeating structure, the rays will undergo constructive or destructive interference in certain directions leading to increased or decreased intensity of the x-ray. And since each material has a different d-spacing, each material has its specific patterns [67]. In figure 19, the XRD setup is shown. The XRD setup consists of an x-ray source, a sample and an x-ray detector.

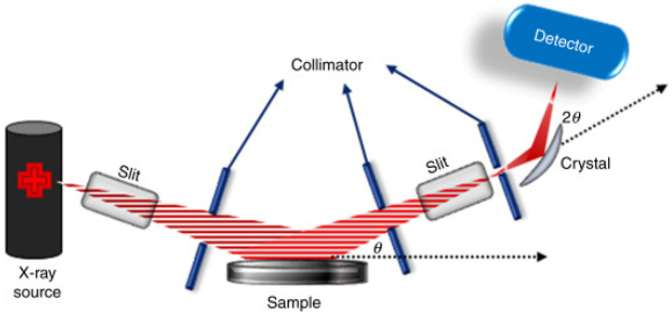

Figure 19: X-ray diffraction setup [68].

Bragg's law relates wave length and lattice space with scattering angle. Where 2θ is the difference between the angle of incident and scattered beam, n is an integer, λ the wavelength and d the lattice spacing. If n is an integer the x-rays will interfere constructively and show a high intensity in the XRD results [69]. The X-ray diffraction results are given with intensity against 2θ. Peaks and their intensities, in XRD patterns, depend on the structure of the material.

$$n\lambda = 2dsin\theta \tag{10}$$

Method

The different samples are analyzed using an X'Pert-Pro diffractometer from PANalytical. This instrument has a Cu Kα radiation source (λ = 1.5406 Å) and operates at 45 kV and 40 mA. To prepare the samples, the powder is loaded into an airtight holder. This holder comprises of a silicon zero-diffraction wafer and a Kapton film arch. The X-ray diffraction measurement takes place under room temperature and atmospheric pressure and scanning across the 2θ range spanning from 10° to 80°.

Using the GSAS-II software further refinement of samples are done to obtain parameters such as lattice parameters.

Phase fraction calculation

One approach to quantify the concentration of a specific structure in the electrolyte powder involves mixing a known quantity of pure silicon with the solid electrolyte. In this project, silicon is hand mixed with the electrolyte at a ratio of 2:8. The resulting mixture is then measured with XRD. Using software GSAS II for refinement of the XRD measurement enables the calculation of the crystal phase content and the amorphous content.

The refinement process takes into account both the crystal phase and the silicon phase by fitting the XRD curve with existing CIF files of the different phases. The refinement results provide weight fractions for both silicon and the crystal phase of the powder. From these known weight fractions it is possible to calculate the real amount of crystal and amorphous content in the powder. An example result from the refinement of a P3m1 and amorphous sample with calculation, is presented below.

First, the obtained weight fractions from the refinements are:

- Si = 0.222
- x$_{P3m1}$ = 0.778
- y$_{amorphous}$ = ?

The silicon weight fraction is known and is equal to 20% since that is the amount that was mixed. Additionally, the total amount of P3m1 and amorphous contents should equal 80%.

$$Si = 0.222 = 20\% \tag{11}$$

$$x_{P3m1} + y_{amorphous} = 80\% \tag{12}$$

Since the amount of Si is known, the following ratio can be made to find the P3m1 phase content.

$$x_{P3m1} = \frac{0.778}{0.222} \cdot 20\% = 70.09\% \tag{13}$$

The amorphous content can then be found.

$$y_{amorphous} = 80\% - x_{P3m1} = 80\% - 70.09\% = 9.91\% \tag{14}$$

Finally, these values should be divided by 80% to have the real content in the electrolyte powder. This results in a P3m1 content of 87.61% and an amorphous content of 12.39%.

Grain size

The grain size can be defined as larger, well-defined crystalline regions within the solid electrolyte. By using the XRD results and the Scherrer equation the grain size can be determined. In equation 15 the Scherrer equation is shown, where λ represents the X-ray wavelength (λ = 0.15406 nm), β is the full width at half-maximum of a diffraction peak (FWHM) (see Figure A.4 for an illustration) and, lastly, θ is the diffraction angle of the diffraction peak [70].

$$d = \frac{0.94 \cdot \lambda}{\beta \cdot cos(\theta)} \tag{15}$$

2.2 Electrochemical impedance spectroscopy (EIS)

Electrochemical Impedance Spectroscopy (EIS) is a powerful technique employed in this project to measure the resistance of an electrolyte. Impedance is defined as the effective resistance of an electric circuit or component to alternating current (AC). In EIS measurements a sinusoidal potential (AC) is applied over a long range of frequencies (in this report from 7 MHz to 0.1 Hz) and the system's response is measured [28]. This impedance is represented as complex numbers, which consist of real and imaginary parts, with the real part representing resistance. By varying the frequency of the AC signal, EIS can investigate different electrochemical processes occurring at different rates.

The data obtained from EIS measurements are commonly presented in Nyquist and Bode plots. The Nyquist plot shows the imaginary part of impedance versus the real part, and gives information on the charge transfer processes and the electrolyte's resistance. High-frequency data points mainly reveal fast processes like ion migration, while slow processes like diffusion display as a low-frequency tail [71].

EIS data can then be fitted to an equivalent electrical circuit model, which represents the electrical components and processes within the electrochemical system. These consist of components such as resistances, capacitors and inductors [72]. In this report, electrolytes with high ionic conductivities are measured. Therefore, the equivalent circuit used for fitting the EIS data, in the software Relaxis 3, is L-(R)(CPE)-CPE as shown in Figure 20. "I" indicates the inductance and is used to take into account inductance from the cables, "R" is the electrical resistance in parallel with CPE which is the constant phase element that is the capacitance of the electrolyte. The last CPE element in the circuit simulates the electronically blocking behaviour of the electrodes at lower frequencies [31].

In Figure 20 a fitting result obtained with RelaxIS is shown. The resulting fitting exhibits an electrolyte resistance of 43.21 Ω with a fitting error of 0.028. This error is minimal and therefore the fitting and electrical circuit used is deemed acceptable. The same methodology is applied to other EIS data throughout this project.

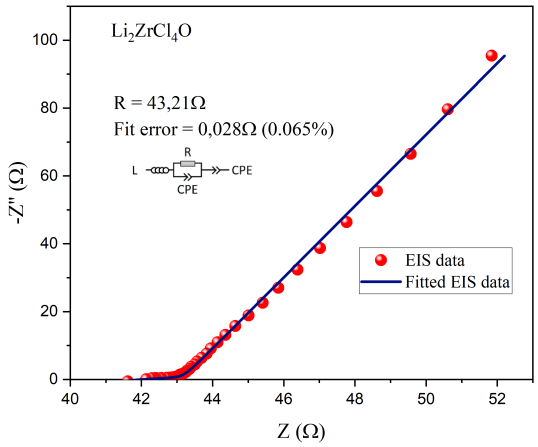

Figure 20: Example graph of EIS data fitting results using RelaxIS with an L-(R)(CPE)-CPE electrical circuit.

Method

The EIS measurements are done as follows. First, 101 grams of the synthesized powder is placed inside a hollow PEEK cylinder. The powder is compressed by placing it between two stainless steel plungers and

cold pressed up to 2.4 tons (305 MPa) using a hydraulic press. This complete step is carried out within an Argon-filled environment.

Once the powder is securely compressed, the cell is tightly sealed under the 2.4-ton pressure. Subsequently, the EIS measurements are performed using an Autolab instrument (AUT86298) within a frequency range spanning from 7 MHz down to 100 Hz. Additionally, some EIS measurements were conducted using the EC lab, covering a frequency range of 1 MHz to 100 Hz.

As explained before, the resulting EIS data are fitted using a I-(R)(P) electrical circuit with RelaxIS 3 software. With this analysis the resistance can be determined.

Conductivity calculation from resistance

The conductivity of the electrolyte can be determined by using the resistance obtained from the EIS measurement. In equation 16, the formula for conductivity is given in mS/cm. The formula consists of the pellet thickness in cm (L), divided by the resistance in Ω (R) and cross-sectional area of the pellet in cm^2 (A).

$$\sigma = \frac{L}{R \cdot A} = \frac{L}{R \cdot \pi \cdot r^2 \cdot 1000} = \frac{1 \cdot 0.05}{R \cdot \pi \cdot 0.5^2 \cdot 1000}(mS/cm) \tag{16}$$

From a paper of van der Maas et al., the measurement error in thickness is taken to be 5%. Since their halide electrolyte made ($Li_3YBr_xCl_{6-x}$) is similar to the halide electrolytes in this report this error is also used [65]. The thickness measured for all electrolytes in this project are around 500 µm, and an error of 5% has also been noticed and is deemed reasonable.

2.2.1 Arrhenius plots

The Arrhenius equation defines the temperature dependence of the conductivity. Which results in the following formula. Where σ is the electrical conductivity (S/cm), σ_0 is the pre-exponential factor (S/cm), Ea is the activation energy (eV), R is the gas constant (8.3145 J/mol) and T is the absolute temperature (K) [30]. The activation energy E_a is of interest in this project due to its relation with conductivity.

$$\sigma = \sigma_0 \cdot e^{-\frac{E_a}{R \cdot T}} \tag{17}$$

This equation can be written in the form of y = -m·x + b where m is the slope and b the intercept. And taking the natural logarithm from both sides yields.

$$ln(\sigma) = -\frac{E_a}{R \cdot T} + ln(\sigma_0) \tag{18}$$

Therefore, by plotting ln(σ) against $\frac{1}{T}$, as shown in Figure 21, it is possible to calculate the activation energy and the pre-factor. Where y = ln(σ), m = -$\frac{E_a}{RT}$, x = $\frac{1}{T}$ and b = ln(σ_0).

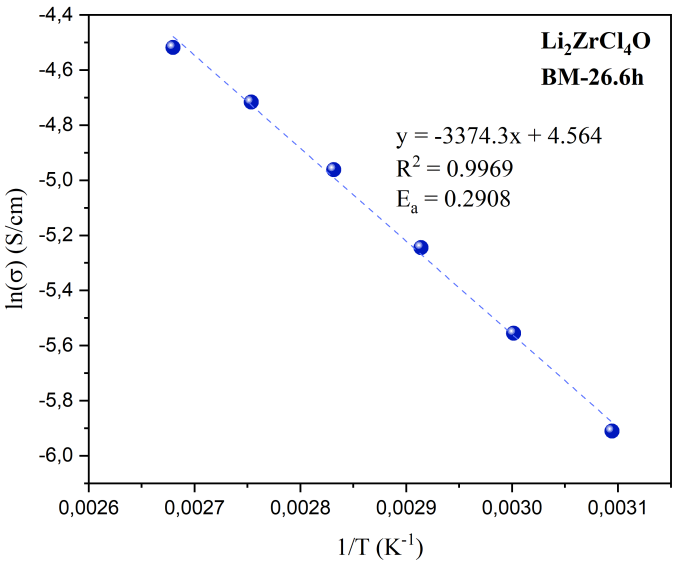

Figure 21: Example of linear regression of EIS measurement at different temperatures.

The activation energy is calculated in J/mol and is converted to eV by multiplying with 1.0364x10^{-5} (as 1 J/mol is 1.0364x10^{-5} eV/particle).

$$E_a = -m \cdot R \cdot 1.0364 \cdot 10^{-5} \tag{19}$$

Lastly, the pre-factor can be found with the intercept and is given in S/cm.

$$\sigma_0 = e^b \tag{20}$$

Method

The setup and preparation of the sample for activation energy measurements, is the same as for EIS measurements. A total of 101 grams of powder is loaded into a hollow peek cylinder and held between two stainless steel plungers. Cold pressing is performed, applying a force of 2.4 tons (305 MPa) to compact the powder and screw the cell the tight to maintain pressure.

Afterwards, the cell is placed inside an oven, and EIS measurements are conducted at various temperatures. The oven is initially set to 30°C for 1 hour, followed by an increase to 50°C for 30 minutes. The temperature is then raised by 10°C steps, with each temperature step held for 30 minutes, until reaching 100°C. Before each temperature change, an EIS measurement is taken (for the range of 50°C to 100°C). The extended duration at each temperature is necessary to allow the cell's internal temperature to stabilize.

2.3 Scanning electron microscopy (SEM)

Scanning electron microscopy (SEM) is an imaging technique that uses focused electron beam to scan the surface of a material. With the SEM a 3D image with high resolution is obtained. Therefore, the surface of a material can be investigated at the microscale and nanoscale [73].

The SEM, in this project, is employed to understand the surface morphology of the Li_2ZrCl_4O electrolyte with varying phase structures. These measurements are conducted within an argon filled environment. Inside the glovebox, the samples are placed into a homemade box and is then opened inside the SEM under argon atmosphere. The SEM used in this report is the JEOL JSM IT100LA.

2.4 X-ray photoelectron spectroscopy (XPS)

X-ray photoelectron spectroscopy (XPS) is an analytical technique used to measure the elemental composition, chemical state, and electronic state of the surface of a material. The XPS measurements can measure up to a depth of 10 nm.

The principle of XPS is the use of incident X-rays that can emit electrons from the atoms on a surface. The resulting kinetic energy from the emitted electrons can then directly be related to the binding energy of the electrons in the material. This makes it possible to identify the elements present on the surface and their properties such as the element's oxidation states (due to a shift of the binding energies) [74].

In this project XPS is used to analyze the oxidation state before and after cycling of the halides in the halide electrolyte, $Li_3YCl_3Br_{3-x}I_x$.

2.5 Electrochemical measurements

2.5.1 Galvanostatic cycling

Galvanostatic cycling measurements involve the application of a constant current, with the resulting voltage being measured. In this project, this measurement approach is used to explore the stability of Li-metal with the investigated electrolytes and the battery cycling performances.

For stability measurements of the electrolyte with Li-metal, a constant current of either 0.2 or 0.5 mA/cm^2 is applied. And for the battery cycling a set voltage range between 3.0 V to 4.3 V vs Li/Li^+. The battery is first activated with a rate of 0.05C followed by continuous cycling at 0.5C.

2.5.2 Linear sweep voltammetry (LSV)

Linear sweep voltammetry (LSV) is a technique used to measure the oxidation or reduction potential of a material. This is done by measuring the current that is obtained as a reaction to the linearly changing applied voltage. Figure 22 displays an example of an LSV plot. When the voltage is continuously increased, the LSV measurement can identify the oxidation potential of a material due to the sudden surge in current. This surge in current is from the oxidation of an element. Contrarily, when the voltage is decreased from high to low values, LSV can be used to determine the reduction potential [75].

In this project, LSV measurements using EC LAB are conducted to investigate the oxidation voltages for the synthesized electrolytes. Voltage steps of 0.1 mV/s and a voltage range from open circuit voltage (OCV) to a specific voltage.

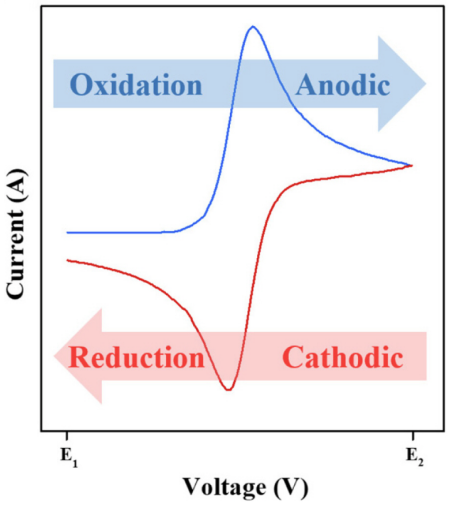

Figure 22: Example of a Linear Sweep Voltammetry (LSV) measurement result with both increasing and decreasing voltages [75].

2.5.3 Cyclic voltammetry (CV)

Cyclic voltammetry (CV) is based on the same principle as the LSV. The main difference is that CV does a full cycle and can be repeated to gather more information on the cyclability of the electrolyte, the reversibility of the redox reactions and different scanning rates can be used [75].

In this project, CV measurements using EC LAB are conducted to investigate the oxidation voltages and the reversibility of these oxidized elements for the synthesized electrolytes. Voltage steps of 0.1 mV/s and a voltage range from open circuit voltage (OCV) to 5.0 V vs. Li/Li^+ are employed.

3

Experimental procedures

3.1 Solid electrolyte composition information

In this project the solid electrolyte $Li_{2x}ZrCl_4O_x$ is studied at different compositions (with x = 0.25, 0.5, 1 and 1.5). This electrolyte is also doped with different elements such as sodium, fluoride and metals having a charge of +3 and +5. Additionally, in this report, a mixed halide $Li_3YCl_3Br_{3-x}I_x$ is also investigated. In Table 1 information can be found about the molar mass of the precursors employed and in Table 2, 3 and 4 the required mass of each precursor to synthesize a specific electrolyte is shown.

Table 1: Molar weights of precursors employed in this project.

Compound	Molar mass (g/mol)
LiI	133.85
LiCl	42.39
LiBr	86.85
LiF	25.94
Li_2O	29.88
Li_2O_2	45.88

Compound	Molar mass (g/mol)
Na_2O	61.98
$LaCl_3$	245.26
YCl_3	195.26
ZrF_4	167.21
$ZrCl_4$	233.04
$TaCl_5$	358.21

Table 2: Precursor weights required for 2g synthesis of specific Zr-based oxyhalide electrolytes powder made in this report.

Compound	LiCl (mg)	Li_2O (mg)	$ZrCl_4$ (mg)	ZrF_4 (mg)	Li_2O_2 (mg)	Na_2O (mg)
$Li_{0.5}ZrCl_4O_{0.25}$		62.18	1939.82			
$LiZrCl_4O_{0.5}$		120.51	1879.70			
$Li_{1.5}ZrCl_4O_{0.75}$		175.47	1824.70			
Li_2ZrCl_4O		227.39	1773.43			
$Li_3ZrCl_4O_{1.5}$		322.70	1677.89			
$Li_2ZrCl_5O_{0.5}$	292.52	103.09	1607.98			
Li_2ZrF_4O		303.28		1697.18		
Na_2ZrCl_4O			1580.01			420.22
$Li_2ZrCl_4O_2$			1671.13		329.01	

Table 3: Precursor weights required for 2g synthesis of specific mixed metals oxyhalides powder made in this report.

Compound	LiCl (mg)	Li_2O (mg)	$LaCl_3$ (mg)	YCl_3 (mg)	$ZrCl_4$ (mg)	$TaCl_5$ (mg)
Li_2LaCl_3O		217.23	1783.04			
$Li_{2.5}La_{0.5}Zr_{0.5}Cl_4O$	146.05	205.87	844.92		802.82	
$Li_{0.66}La_{0.5}Zr_{0.5}Cl_{3.5}O_{0.33}$		79.20	984.92		935.88	
Li_2YCl_3O		265.48		1734.89		
$Li_{2.1}Y_{0.1}Zr_{0.9}Cl_4O$	32.22	227.09		148.40	1593.99	
$LiTaCl_5O_{0.5}$		80.08				1920.00
$LiLa_{0.5}Ta_{0.5}Cl_5$	150.68		1067.8			781.4
$Li_{0.66}La_{0.5}Zr_{0.25}Ta_{0.25}Cl_{3.75}O_{0.33}$		70.40	875.58		415.98	639.40

Table 4: Precursor weights required for 2g synthesis of specific mixed halides electrolyte powder made in this report.

Compound	LiI (mg)	LiBr (mg)	LiF (mg)	YCl_3 (mg)
$Li_3YCl_3Br_3$		857.19		1143.90
$Li_3YCl_3Br_{2.8}I_{0.2}$	115.10	1045.68		839.60
$Li_3YCl_3Br_{2.6}I_{0.4}$	224.86	948.40		820.08
$Li_3YCl_3Br_{2.4}I_{0.6}$	331.92	861.48		807.01
$Li_3YCl_3Br_{2.2}I_{0.8}$	434.74	774.28		792.74
$Li_3YCl_3Br_2I$	553.40	694.80		781.04
Li_3YFCl_3BrI	607.68	394.30	117.76	886.48
$Li_3YF_{0.5}Cl_3Br_2I_{0.5}$	298.22	774.01	57.79	870.08

3.2 Synthesis procedure

The synthesis is carried out under argon atmosphere (O2 $<$ 1 ppm, H_2O $<$ 1 ppm). The first step is to weigh the different amounts of precursor to synthesize the correct compound. The following purities and providers for each precursor are: LiCl (Sigma, 99%), LiI (Sigma, 99%), LiBr (Alfa, 99.9%), LiF (Sigma, 99.98%), Li_2O (Sigma, 97%), $ZrCl_4$ (Sigma, 99.99%), ZrF4 (Sigma, 99.9%), Li_2O_2 (Sigma, 90%), Na_2O (Sigma, 80%), $LaCl_3$ (Sigma, 99.9%), YCl_3 (Sigma, 99.99%) and $TaCl_5$ (Sigma, 99.99%).

During the ball milling process, used to synthesize the specific electrolyte, a specific ratio of 40g $ZrCl_4$ balls to 1g of precursor powder (or 80g:2g) is kept. The ball milling procedure consists of 5 minutes of rotation followed by 5 minutes of resting time, with varying numbers of cycles. The rotational speed is set at 550rpm. A combination of two different sizes of ZrO_2 balls, with diameters of 3mm and 10mm, is used in equal proportions.

When an annealing step is conducted, the electrolyte powder is compressed into a pellet weighing approximately 400mg. This pellet is subsequently placed inside a glass ampoule, which is then sealed either within a nitrogen gas environment or under vacuum. Afterwards, the sealed ampoule is placed in an oven at a specific temperature and duration.

3.3 Cell assembly

In this project, a homemade cell is used which consists of an insulating hollow PEEK cylinder with stainless steel plungers on both ends. These plungers serve as current collectors and can be used to compress the powder into a pellet.

As stated before, for measurement methods that need only a single layer of solid electrolyte, such as

EIS and Arrhenius measurements, precisely 101 milligrams of the precursor powder is loaded into the hollow PEEK cylinder. This 101 mg quantity ensures consistent thickness for the solid electrolyte layer within the cell at all times. Finally, a pressure of 2.4 tonnes (equivalent to 305 MPa) is applied for 5 minutes, and the cell is tightly screwed to maintain this pressure.

In the Li-metal and electrolyte **stability measurements** a symmetric cell is made. The process is as follows: approximately 101 mg of the electrolyte is loaded into a hollow PEEK cylinder within a homemade cell and compressed to 2.4 tonnes. Li-metal films with a 10 mm diameter are positioned on both sides of the electrolyte, and the cell is tightly sealed under low pressure. It's crucial to exercise caution during this procedure due to the soft nature of Li-metal, which increases the risk of potential short-circuits.

The battery configuration for **galvanostatic cycling** measurements is assembled as follows. First, ≈50 mg of synthesized electrolyte is placed into the hollow PEEK cyclinder within the homemade cell. This is slightly hand pressed by pushing both stainless steel plungers. Afterwards, ≈50 mg of the protective layer, argyrodyte (Li_6S_5Cl), is added on top and pressurized by a hydraulic press up to 0.4 tonnes. Next, 11 mg of the cathode layer is added onto the protective layer. This cathode is a 20 minutes hand grinded mixture of NMC 811:Li_2ZrCl_4O with a 70:30 ratio. This cell is then subjected to a pressure of 2.4 tonnes. Lastly, on the Li_2ZrCl_4O layer side, the anode Li-In metal with a weight ratio of 1:40 is added. Additionally, a copper metal current collector with a 10 mm diameter is added. This assembly is slightly pressurized at 0.4 tonnes in order to ensure good contact between the layers.

The preparation process of the battery for **LSV and CV** measurements is identical to that employed for the galvanostatic measurements. However, the only difference lies in the cathode used, which is carbon nanofibers (CNF) instead of NMC811.

4

Results

It's important to note that in this report, the term "ball mill time" refers to the effective ball milling duration, excluding any resting time during each cycle. Additionally, unless mentioned otherwise, the ball milling has been carried out in cycles consisting of 5 minutes of spinning at 550 rpm followed by 5 minutes of rest. Also, EIS measurements are conducted at room temperature unless mentioned differently. Lastly, many measurements were made on the same composition but to prevent repetition in the report, only the most interesting ones are kept and the rest is placed in the appendix.

Below a summary table is made with an overview of all the most interesting results obtained for the different electrolytes investigated (see Table 5).

Table 5: Summary of most relevant results for (a) Zr-base oxyhalides and (b) mixed halide electrolytes.

Electrolyte	Ball mill time (h)	Annealing (300°C, 5min)	Conductivity (mS/cm)	Activation energy (eV)	Oxidation potential (V vs. Li/Li^+)	Fully amorphous phase reached
Zr-based oxyhalide						
$LiTaCl_5O_{0.5}$	16.5	-	3.5	-	-	Yes
Li_2ZrCl_6	8.3	-	0.48	-	4.142	-
$Li_{0.5}ZrCl_4O_{0.25}$	28.3	-	0.68	~0.298	-	Yes
$LiZrCl_4O_{0.5}$	18.2	-	1.06	~0.276	4.099	Yes
Li_2ZrCl_4O	17.2	-	1.60	~0.281	4.033	No
$Li_3ZrCl_4O_{1.5}$	4.2	-	1.23	~0.274	-	No
$Li_2ZrCl_5O_{0.5}$	10	-	1.25	-	4.019	No
$Li_{2.1}Zr_{0.9}Y_{0.1}Cl_4O$	10.8	-	1.58	-	-	~Yes
$Li_{0.66}La_{0.5}Zr_{0.5}Cl_{3.5}O_{0.33}$	18.9	-	0.65	-	-	-
$Li_{0.66}La_{0.5}Zr_{0.25}Ta_{0.25}Cl_{3.75}O_{0.33}$	16.5	-	1.55	-	-	-
Mixed halide electrolyte						
$Li_3YCl_3Br_3$	8.3	Yes	1.94	-	3.59	-
$Li_3YCl_3Br_{2.8}I_{0.2}$	8.3	Yes	1.63	-	3.552	-
$Li_3YCl_3Br_{2.6}I_{0.4}$	8.3	Yes	2.03	-	3.531	-
$Li_3YCl_3Br_{2.4}I_{0.6}$	8.3	Yes	2.43	-	3.451	-
$Li_3YCl_3Br_{2.2}I_{0.8}$	8.3	Yes	2.85	-	3.471	-
$Li_3YCl_3Br_2I$	8.3	Yes	3.55	-	3.474	-

4.1 Oxyhalide electrolyte

In this chapter the performances of solid electrolytes $LiTaCl_5O_{0.5}$, Li_2ZrCl_6 and $Li_{2x}ZrCl_4O_x$ with X = 0.25, 0.5, 1 and 1.5 are analyzed. Additionally, pathways of aliovalent doping with different metals and precursors are explored. The analysis is done through methods such as XRD, EIS (room temperature and at different temperatures), LSV/CV and SEM.

4.1.1 Structure and conductivity of $LiTaCl_5O_{0.5}$

The initial motivation and inspiration for this project started when reading the incredible and promising performances of $LiTaCl_5X^n_{1/n}$ electrolyte, particularly parameters such as the ionic conductivity, electrochemical stability window and cyclability (as shown in chapter 1.7.3) [58]. Therefore, the first step in this project is to recreate the $LiTaCl_5O_{0.5}$ electrolyte.

In the research of Ishiguro et al., they ball mill the powder for 200 hours followed by annealing for 2 hours at 120°C. Therefore, the first step is to ball mill the mixture in the same conditions as them with an expected fully amorphous structured sample. In Figure 23, the X-ray diffraction (XRD) pattern is shown with its respective conductivity at different ball milling (BM) times. After 16.5h of BM the powder seems to hold an amorphous structure as no peaks are observed and the resulting conductivity is around 3.5 mS/cm. However, after already 33 hours of BM the structure is not fully amorphous anymore and a drastic loss in conductivity follows. These new peaks observed in the XRD at 33h of BM could be attributed to ZrO_2 which might have originated from the ZrO_2 balls used within the ball mill jar. It appears that 33h of BM is too harsh on the powder, causing the ZrO_2 to be incorporated into the structure. Since ZrO_2 is not conductive, this incorporation leads to a conductivity drop. Further BM introduced even more ZrO_2 into the structure continuing to drop the conductivity. Therefore it was decided to stop this measurement after 41.3h of BM.

The highest achieved conductivity is around 3.5 mS/cm, significantly lower than the reported conductivity of 8.92 mS/cm, even-though the XRD structure displays an amorphous structure. This inconsistency in XRD for longer ball milling time may be due to variations in the type of balls or type of ball mill jar used. Despite the results not matching the promising paper's result, it is still very interesting to investigate if the reported performances can be mimicked in another type of oxyhalide based on zirconium metal ($Li_{2x}ZrCl_4O_x$) which is much less expensive.

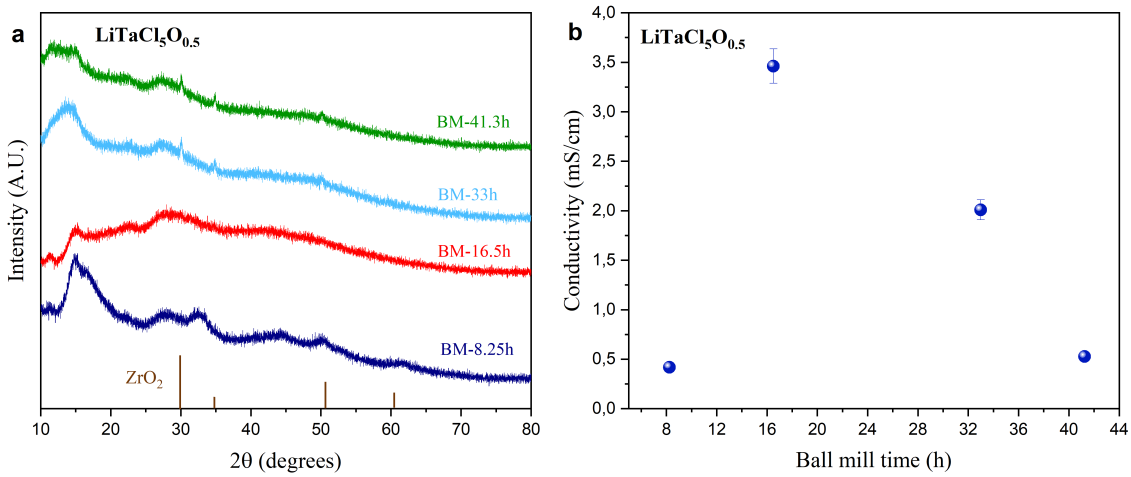

Figure 23: (a) X-ray diffraction pattern of $LiTaCl_5O_{0.5}$ ball milled for different times and (b) their respective ionic conductivities.

4.1.2 Structure and conductivity of Li_2ZrCl_6

As stated before, one of the primary focuses of this report is on the Zr-based oxyhalide electrolyte: $Li_{2x}ZrCl_4O_x$. Therefore, first the electrolyte Li_2ZrCl_6 is synthesized and analyzed in order to compare its performances with its oxyhalide counterpart.

In Figure 24, the XRD and the electrochemical impedance pectroscopy (EIS) results are depicted after 8.3 hours of BM. The crystal structure is identified as P3m1, and a resistance of 132 Ωis measured, equivalent to 0.48 mS/cm. This conductivity value is similar with the 0.4 mS/cm at 30°C reported by Kwak et al. after

BM for 10 hours [37]. However, it is lower than the reported 0.81 mS/cm achieved after 45 hours of BM by Wang et al. [26]. This could be due to the difference in BM time. Further on in this report, the LSV measurement reveals an oxidation potential of 4.142 V vs. Li/Li^+ (see Figure 36).

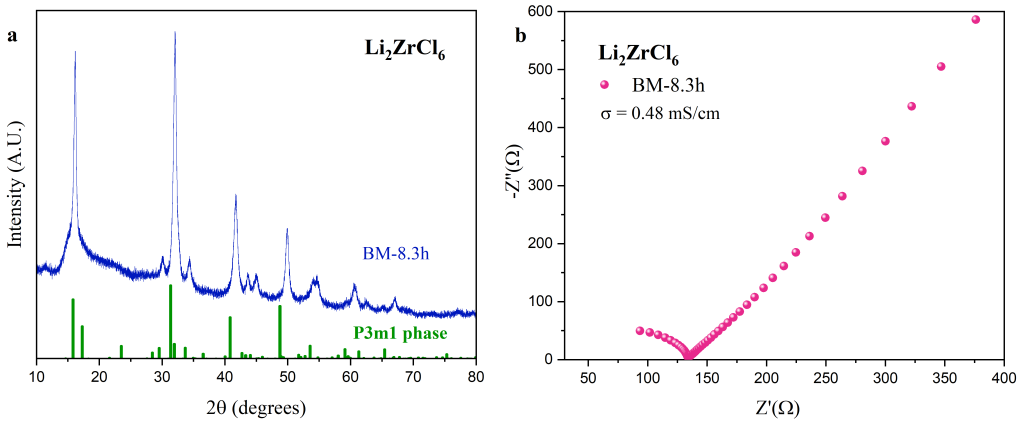

Figure 24: (a) X-ray diffraction measurement and (b) electrochemical impedance spectroscopy measurement of Li_2ZrCl_6 ball milled for 8.3 hours.

4.1.3 Structure, conductivity and activation energy analysis of $Li_{2x}ZrCl_4O_x$.

$Li_{0.5}ZrCl_4O_{0.25}$

Structure and conductivity

The oxyhalide electrolyte with the lowest Li_2O precursor content studied in this project is $Li_{0.5}ZrCl_4O_{0.25}$. The possible future shortages of lithium and its associated costs could make this composition more advantageous [5].

Concerning the $Li_{0.5}ZrCl_4O_{0.25}$ composition, the XRD results presented in Figure 25a indicate that, following BM durations of 16.5 and 20.7 hours, the material exhibits predominantly a C2/m crystalline phase. Interestingly, with prolonged BM times, the crystal structure gradually shifts towards an amorphous structure. This change in structure, as explained in chapter 1.6.2, could be due to the continuous high energy collisions during BM resulting in strong mechanical forces, temperature elevation, and reduced particle size. Furthermore, upon a detailed examination of the XRD patterns, no precursor peaks are observed, indicating that the powder is well mixed and all Li_2O is incorporated in the structure. The XRD pattern for the Li_2O precursor is illustrated in appendix Figure B.1, where the principal diffraction peak arises at 33.50°.

The observed trend in the conductivity of this composition (see Figure 25b) suggests a direct relationship: as the presence of the C2/m crystalline phase diminishes and the amorphous phase becomes more dominant, the conductivity increases. This could be an indication that a more amorphous phase and its resulting disorder can result in a more conductive material. At higher BM times, the conductivity appears to reach a plateau. The highest conductivity of 0.68 mS/cm is measured in the amorphous phase after 28.3h of BM.

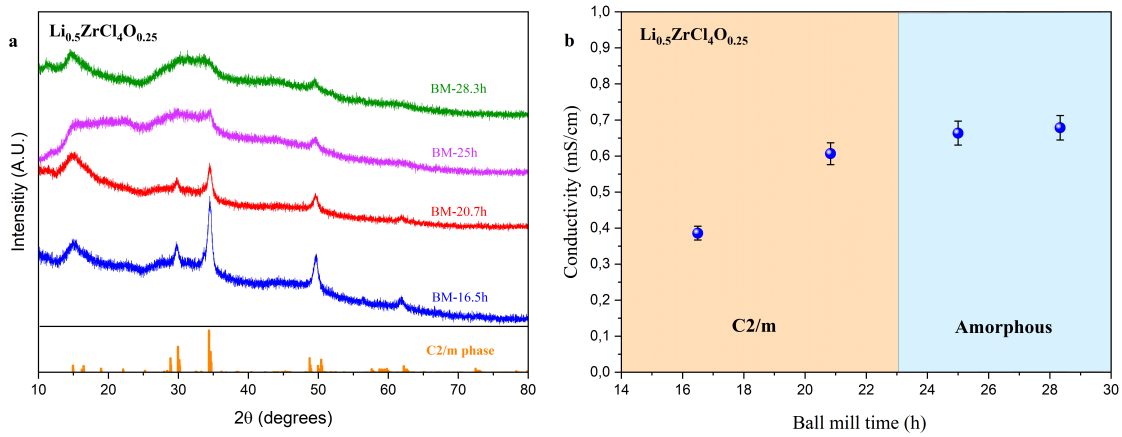

Figure 25: (a) X-ray diffraction measurements and (b) conductivity measurements of $Li_{0.5}ZrCl_4O_{0.25}$ ball milling for different durations.

XRD and conductivity results of another batch with smaller ball milling time-steps is shown in Figure 26. A similar trend is observed as in the previously presented batch. Interestingly, at minimal BM times of 2.1h and 4.2h, the conductivity is remarkably low. In the case of 2.1h of BM, this could be due to a lack of mixing, where the BM did not result in enough energy transfer to break atom bonds and introduce the precursor inside the structure. This is confirmed with the small diffraction peak of Li_2O observed at 33.50°. However, even after 4.2h of BM the conductivity remains low, although the Li_2O has been incorporated, indicating another cause. Short BM times might result in larger particle sizes and potentially an uneven composition which might impede the conductivity pathways.

With the gradual increase in BM time from 4.2h on, there is a noticeable suppression of the C2/m phase by what appears to be the amorphous phase. This phase change results in an increase in conductivity, again indicating the amorphous phase is more conductive possibly due to an increase in disorder. After 18.7h of BM, the C2/m phase is nearly indistinguishable, and the structure is almost fully amorphous, with a prevalent amorphous phase at 26.9h of BM, reaching a maximum conductivity of 0.61 mS/cm.

Another batch can be found in appendix Figure B.2 but the conductivity is worse and the amorphous phase is not reached even with 44.9h of BM.

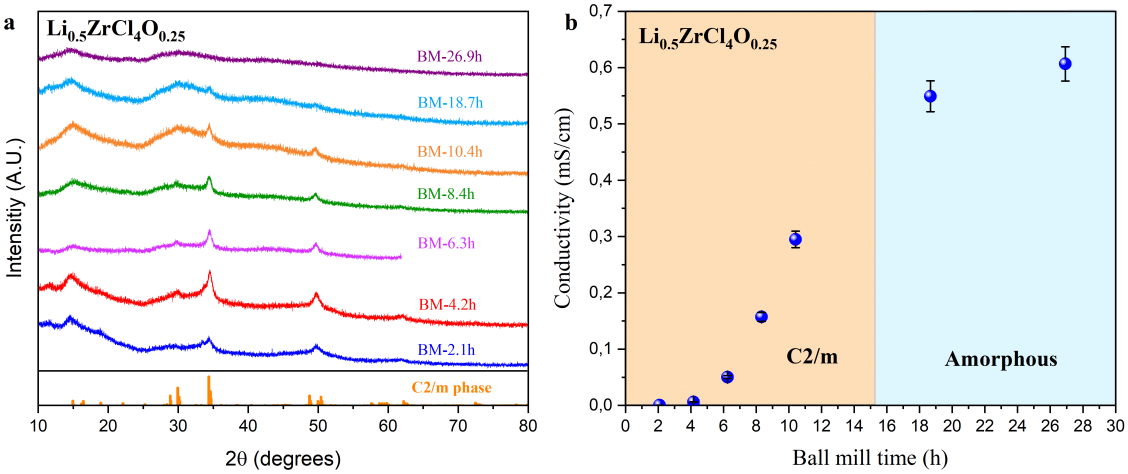

Figure 26: (a) X-ray diffraction measurements and (b) conductivity measurements of $Li_{0.5}ZrCl_4O_{0.25}$ ball milling for different durations.

Activation energy

In the Arrhenius experiment conducted on two different BM times (see Figure 27), the activation energy (E_a) remains very similar, with values of 0.2979 eV for 16.5h of BM and 0.2990 eV for 35.8h of BM.

Interestingly, despite the similar activation energies, the obtained conductivities measured at different temperatures are twice as small for the 35.8h BM sample compared to the 16.5h BM sample (see Figure 27c). This difference in conductivity is reflected in the pre-factor value which doubled (see Figure 27d). A factor for this pre-factor increase could be the jump distance (a) which decreases with a decreasing lattice parameter. It is also worth considering that the behavior of this specific batch is unusual because the dominant amorphous phase is never fully reached, which is different from the trend observed in the other batches.

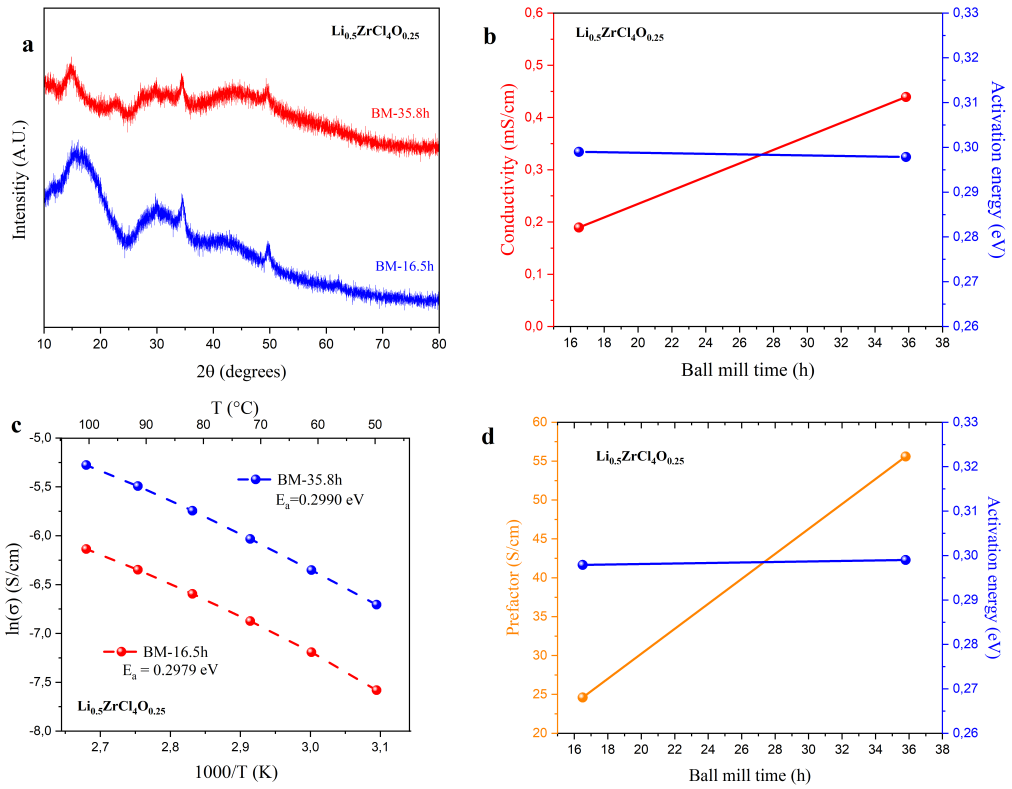

Figure 27: Arrhenius measurements with 16.5h and 35.8h BM $Li_{0.5}ZrCl_4O_{0.25}$, a) corresponding XRD patterns, b) corresponding conductivity and activation energy (E_a), c) corresponding conductivities from 50 to 100°C and d) corresponding pre-factor with activation energy.

$LiZrCl_4O_{0.5}$

Structure and conductivity

In the investigation of $LiZrCl_4O_{0.5}$ composition, it is observed that distinct structural phases emerge during different BM durations notably: C2/m, amorphous, and P3m1. In Figure 28, the XRD and conductivity results of $LiZrCl_4O_{0.5}$ are shown at different BM times (for this batch the effective BM cycles are 10 minutes instead of 5 minutes). Initially, with 8.3h of BM, the C2/m phase predominates, but a gradual increase in the amorphous phase is observed, leading to a dominating amorphous state after 14.7h of BM. Interestingly, this amorphous phase remains relatively stable for a few hours of milling. With 18.2h of BM, however, a P3m1 phase starts to emerge and after an additional 10h of BM, a clear transition to the P3M1 phase occurs. In this and other batches, no Li_2O precursor is detected, suggesting that all the precursor

enters the structure at this composition.

In terms of conductivity, the C2/m phase exhibits the lowest conductivity, while an increase in conductivity is observed as the amorphous phase becomes more predominant, reaching its highest value at 1.06 mS/cm after 18.2h of BM. Interestingly, the highest conductivity is achieved not in a fully amorphous structure but rather when the material begins to transition toward a P3m1 structure. The predominantly P3m1 phase also displays good conductivity, although it is slightly lower than that of the mixed amorphous phase. From these measurements it seems that the C2/m phase is less favorable for ionic conductivity and there appears to be an optimal ratio of amorphous and P3m1 phase since the conductivity increased in between 17.2h and 18.2h of BM. Meaning that potentially an even higher conductivity could be reached in between the transition from the amorphous phase to the P3m1 phase (18.2h-28.2h of BM).

It's worth noting that the conductivity measurement at 14.7h of BM might have been a measurement error since the conductivity remains unchanged despite a shift in the crystal phase. Additional batches in the appendix Figures B.3 and B.4 exhibit similar trends, affirming the consistency of these phase transitions and their corresponding effects on conductivity.

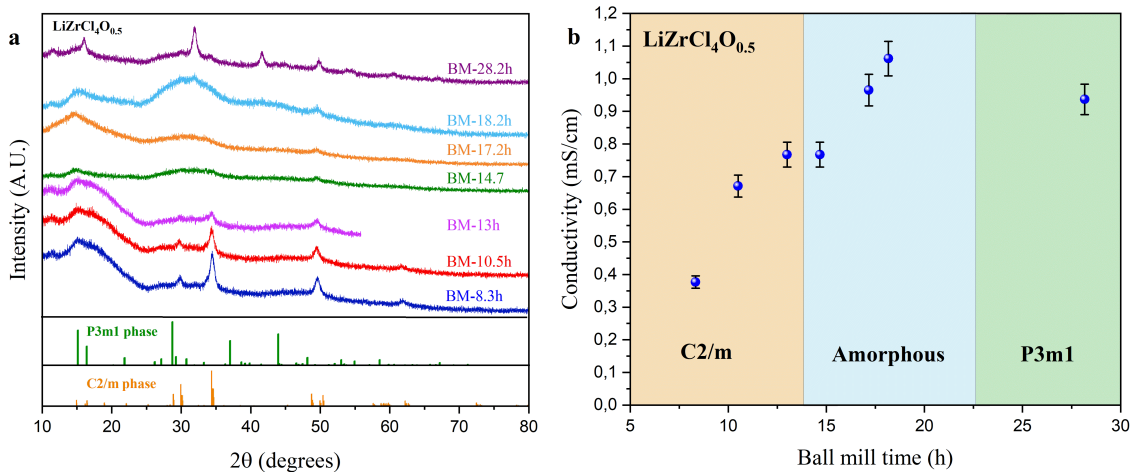

Figure 28: (a) XRD measurements and (b) EIS measurements of $LiZrCl_4O_{0.5}$ ball milling for different durations.

Activation energy

The three distinct phases are analyzed through Arrhenius measurements. Figure 29c reveals that the activation energy is the lowest for the amorphous dominating phase, with a value of 0.2764 eV, followed by the C2/m phase with 0.2888 eV, and the P3m1 phase with 0.3024 eV. The activation energy of the P3m1 phase is larger than the C2/m phase although the conductivity is higher. This pattern is reflected in the pre-factor (Figure 29d) that increases drastically for the P3m1 phase. Considering the trend of the pre-factor and the activation energy, it follows the same trend based on the pre-factor equation 7, which is related to the oscillatory frequency v_0 and decreases with decreasing activation energy.

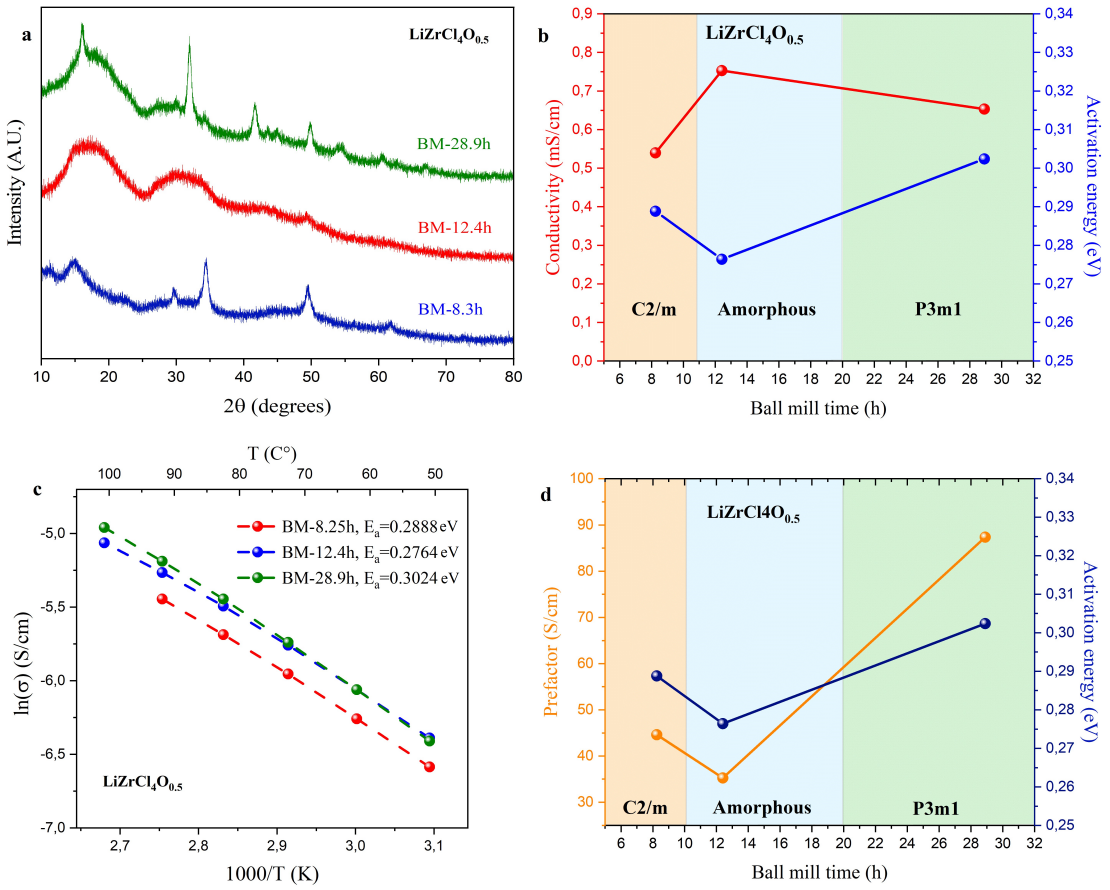

Figure 29: Arrhenius measurements with 8.3h, 12.4h and 28.9h ball milled $LiZrCl_4O_{0.5}$, a) corresponding X-ray diffraction patterns, b) corresponding conductivity and activation energy (E_a), c) corresponding conductivities from 50 to 100°C and d) corresponding pre-factor and activation energy.

Li_2ZrCl_4O

Structure and conductivity

The composition Li_2ZrCl_4O has been a focus point of this project and has consistently exhibited the highest conductivity, reaching 1.60 mS/cm with 17.2h of BM. In the first representative batch, as shown in Figure 30a and 30b, an interesting trend is observed. Compared to the samples, shown previously, with a higher concentration of Li_2O, the initial phase formed after 8.3h of BM is the P3m1 phase (compared to C2/m). With an additional 8h of BM, there is an emergence of a seemingly amorphous phase with some coexistence of P3m1 and C2/m phases. However, it appears a complete amorphous phase is not attainable. Finally, as ball milling continues, the structure transitions towards a C2/m phase. Extending the BM time even further doesn't lead to a change in structure but rather an increase in the formation of the crystalline C2/m phase. Furthermore, there is still some Li_2O precursor present in the powder which is visible in the XRD data for the P3m1 and amorphous phase at 33.50°. Nevertheless, it appears that with a sufficiently long duration of ball milling (BM), the Li_2O precursor is incorporated into the C2/m structure.

Among the identified phases, the the crystalline P3m1 phase exhibits fine conductivity, with 1.28 mS/cm. The predominant amorphous phase, however, demonstrates the highest conductivity with 1.48 mS/cm. Curiously, it becomes evident that as BM time increases beyond a certain point, there is a drop in conductivity. This trend continues even with very long BM (41.3 hours). This observation suggests that the C2/m is not a favorable structure towards high conductivity and agrees with what has been observed

with previous compositions. Additionally, it is expected that with the presence of Li_2O precursor the conductivity decreases as Li_2O is a poor conductor. Nonetheless, a high conductivity is still measured. This could suggest an even higher conductivity can be reached if the precursor is eliminated.

In another batch, as depicted in Figure 30c and 30d, a more detailed investigation is conducted by using smaller steps of BM time to create a clearer connection between structure and conductivity. Similar to the previous batch, the P3m1 phase emerges after 8.3h of BM, and as BM time increases gradually, the electrolyte powder approaches a coexistence between P3m1, amorphous and C2/m structure. It seems that achieving a completely amorphous phase for this composition may not be feasible especially looking at 17.8 and 19.1h of BM. Afterwards, with just one additional hour of BM (20.3h) the phase transitions towards a dominant C2/m phase. This highlights the sensitivity of this coexisting phase to ball milling and the challenge of achieving the optimal structure for attaining the highest conductivity. Moreover, the Li_2O precursor is again visible in the powder for all BM times.

From the previous compositions, conductivities tend to improve as the dominance of the amorphous phase increases. Interestingly, the highest conductivity is not achieved at what seems to be the most amorphous phase at 17.8h and 19.1h of BM (1.458 and 1.468 mS/cm) but rather when there is still a significant presence of the P3m1 phase at 16.6h of BM (1.535 mS/cm). This decrease in conductivity observed at 17.8 hours of ball milling could be attributed to the increasing presence of the less conductive C2/m phase.

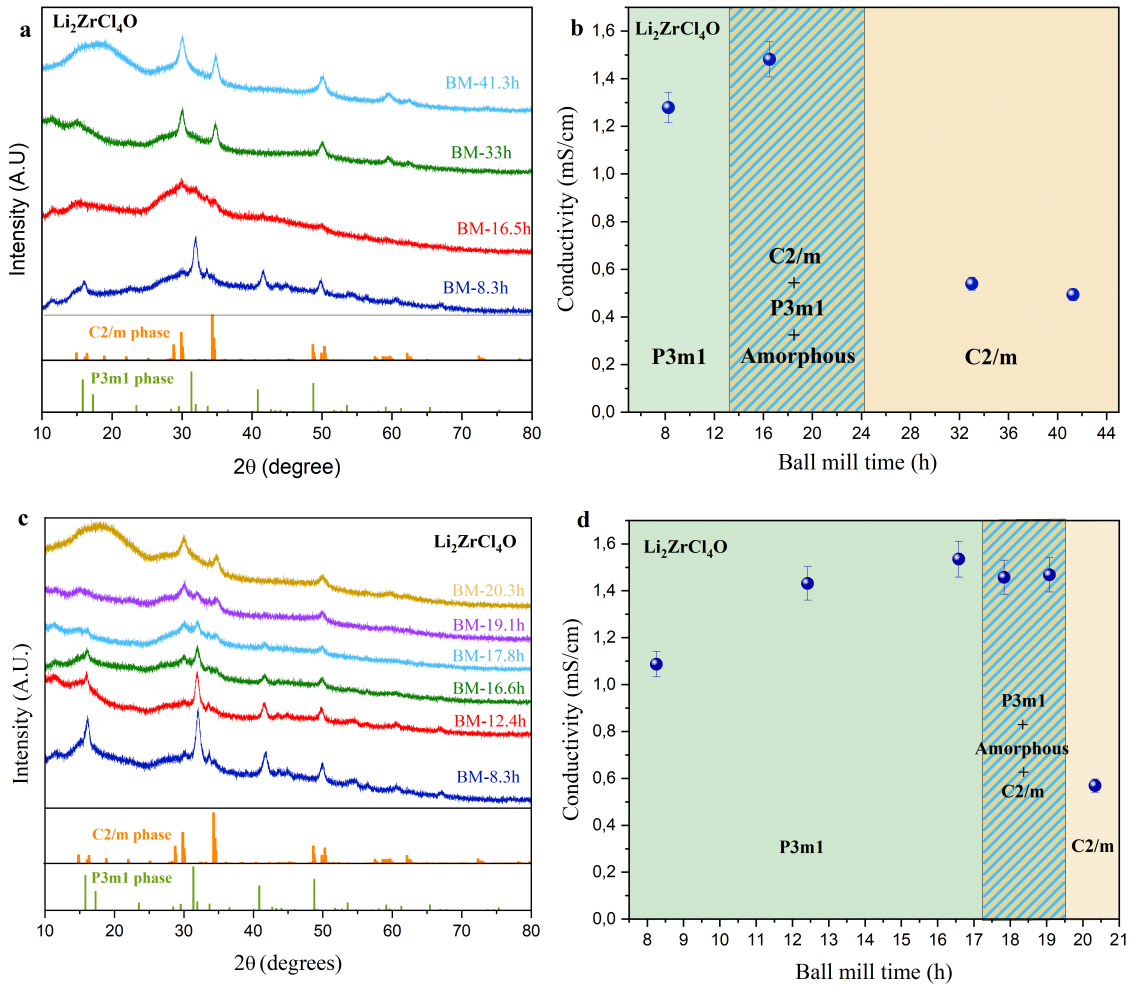

Figure 30: First batch of Li_2ZrCl_4O ball milled at different durations (a) resulting XRD measurements and (b) conductivity measurements. Second batch of Li_2ZrCl_4O ball milled at different durations (c) resulting XRD measurements and (d) conductivity measurements.

An additional batch (see Figure B.5) further supports the conclusion that synthesizing a fully amorphous phase does not seem possible and that an optimal ratio of the P3m1 and amorphous phases exists, which maximizes conductivity without the clear presence of the C2/m phase. The highest conductivity measured is 1.60 mS/cm and is also composed of some presence of P3m1 and amorphous phase.

Finally, an attempt is made to determine if a conductive phase can be observed with minimal ball milling of 2.3 hours, as shown in Figure B.6. Unfortunately, as with previous compositions, a low conductivity of 6.53x10^{-3} mS/cm is measured, indicating that more ball milling is required. The limited conductivity could be attributed to the fact that the crystal phase has not yet formed, and the precursors have not mixed thoroughly (as shown by the clear presence of the Li_2O precursor at 33.50° in the XRD).

Activation energy

Arrhenius measurements are made on the predominantly P3m1, amorphous and C2/m phases. In Figure 31b the Arrhenius measurements reveal a correlation between activation energy and conductivity, with activation energy increasing as conductivity decreases. Specifically, the mostly amorphous phase sample (BM time of 18.3h) exhibits the highest conductivity with an activation energy of 0.2813 eV, while the P3m1 phase shows activation energies of 0.3049 eV and 0.2911 eV. The C2/m phase displays a similar activation energy and conductivity to the P3m1 phase, measuring at 0.2908 eV. Additionally, the resulting pre-factors also follow the expected trend based on the pre-factor equation 7.

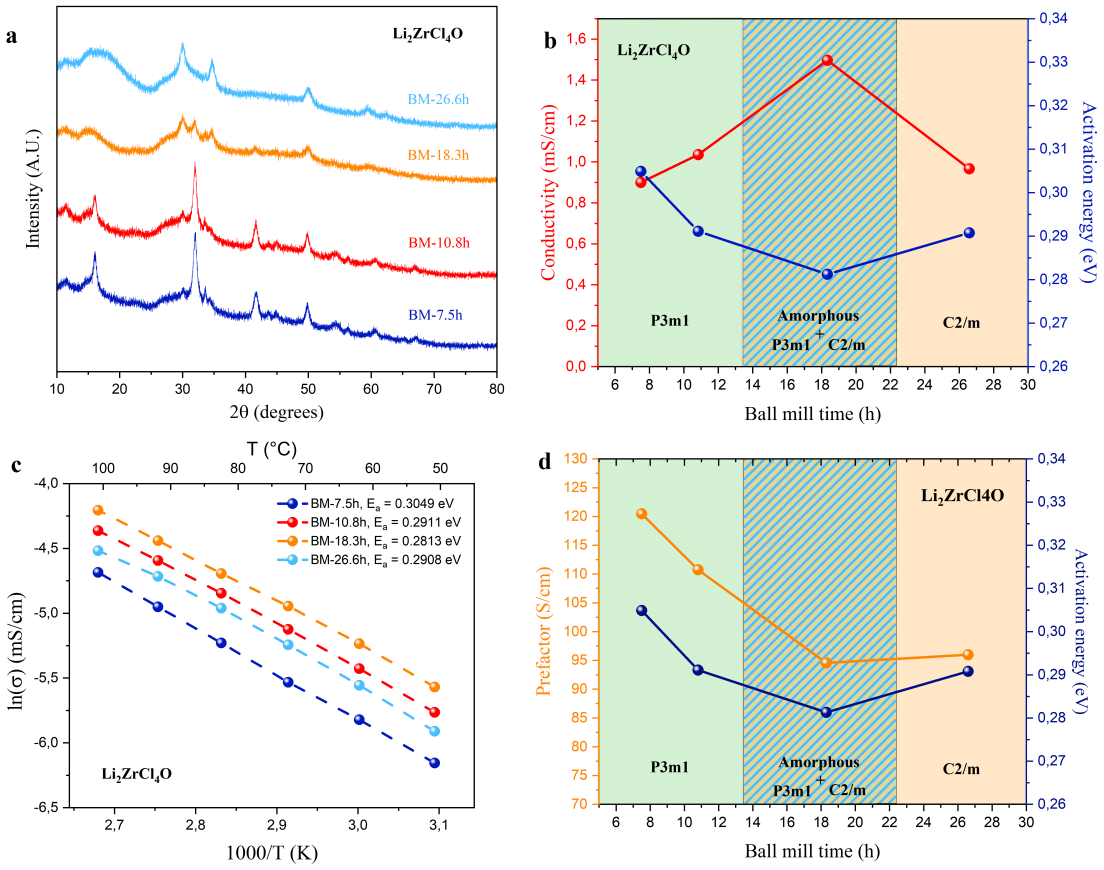

Figure 31: Arrhenius measurements with 7.5h, 10.8h, 18.3 and 26.6h BM Li_2ZrCl_4O, a) corresponding X-ray diffraction patterns, b) corresponding conductivity and activation energy (E_a), c) corresponding conductivities from 50 to 100°C and d) the corresponding pre-factor and E_a.

Phase contents of Li_2ZrCl_4O

Figure 32a displays the resulting XRD patterns obtained from hand-mixed pure silicon with varied BM times of Li_2ZrCl_4O at a 2:8 ratio. The structural compositions are selected to include a predominant P3m1 structure, a coexistence of P3m1, C2/m, and amorphous phases, and a pure C2/m phase. By employing refinements with GSAS II software and the introduction of silicon, it becomes feasible to determine the proportion of each phase present for each BM duration (see refinement results in Figure B.7).

From Figure 32b, it is evident that with a BM time of 7.5 hours, the P3m1 phase prevails with 87% content, yielding a conductivity of 0.86 mS/cm. However, extending the BM time by just 3.3 hours leads to a substantial increase in amorphous content, reaching 57% content, and a higher conductivity of 1.26 mS/cm. After 18.3 hours of BM, the amorphous phase becomes the dominant component at 61%, accompanied by a further increase in conductivity to 1.50 mS/cm. With continued BM, the P3m1 phase diminishes, and the C2/m phase becomes more prominent, resulting in a significant drop in conductivity. This analysis exhibits the positive influence of amorphous content on conductivity, while indicating that the C2/m phase is less conductive than the P3m1 structure (as with similar contents of $\approx$ 43% a lower conductivity is observed for the C2/m phase).

Hu et al. have reported a relationship between grain size and phase fraction, observing a decrease in both P3m1 and C2/m grain sizes with increasing amorphization. Their study, however, was conducted with the same BM time but for different compositions [16]. In contrast, in Figure 32b, a distinct trend is not immediately clear but it does appear that as BM time increases, there is a reduction in grain size, a phenomenon that can be attributed to the continuous exerted mechanical forces on the material by the milling balls during the BM process.

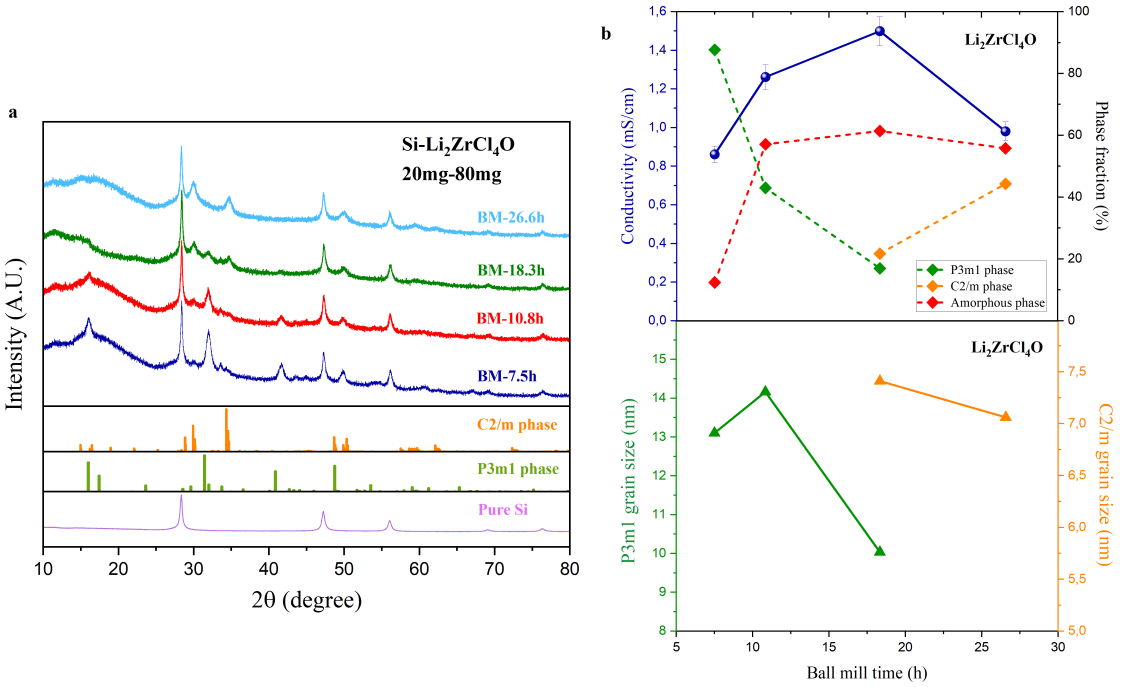

Figure 32: (a) X-ray diffraction of hand-mixed pure silicon and different ball milled times of Li_2ZrCl_4O with 2:8 ratio, (b) resulting crystallinity, structure and grain size.

$Li_3ZrCl_4O_{1.5}$

Structure and conductivity

$Li_3ZrCl_4O_{1.5}$ is the composition with the highest Li_2O precursor content in this project. The resulting XRD and conductivities are shown in Figure 33. Similar to Li_2ZrCl_4O, in this composition, the P3m1 phase is the first phase to appear after 4.2h of BM, but already shows signs of amorphization. With an additional 2h and 4h of BM, a more amorphous phase is created, but XRD data also show the presence of peaks from the P3m1 and C2/m phases. After 12.4h of BM the structure is mainly C2/m. Again at approximately 33.50° in the XRD measurement, the Li_2O precursor has a visible peak. Only at the highest ball milled sample the precursor is fully incorporated into the structure.

Considering the conductivity, interestingly, the phase that exhibits the highest conductivity, with 1.23 mS/cm, is achieved with little BM time of 4.2h. This trend supports the idea that with higher Li_2O content there is a faster amorphization as for $Li_{0.5}ZrCl_4O_{0.25}$ around 20h of BM is needed compared to 16h for Li_2ZrCl_4O. Notably, even at 2.1 hours of BM, when the electrolyte doesn't have a clear structure yet, it already displays a conductivity of 0.955 mS/cm. Similar to the Li_2ZrCl_4O composition, it seems that a fully amorphous phase cannot be achieved. The 4.2h BM powder is a coexistence of mainly P3m1 and amorphous phases. And with only 2.1h of additional BM the structure switches clearly to a coexistence of C2/m and amorphous phases. Due to the presence of the C2/m phase the conductivity decreases as the C2/m phase is not highly conductive. Therefore, the highest conductivity is observed with 4.2h of BM. Afterwards, with additional BM time to 12.4h and 20.8h of BM, the electrolyte transitions quickly to the C2/m phase, resulting in a significant drop in conductivity.

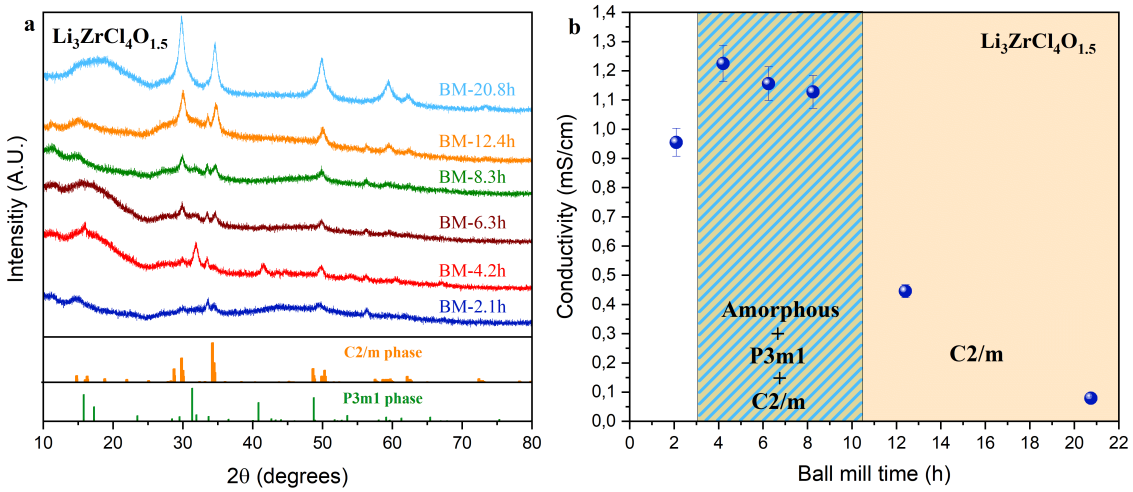

Figure 33: (a) X-ray diffraction measurements and (b) conductivities of $Li_3ZrCl_4O_{1.5}$ ball milling for different durations.

Activation energy

From the Arrhenius measurements, in Figure 34, the activation energy of the mainly P3m1 phase exhibits 0.2803 eV while the predominant coexistent C2/m and amorphous phases have a slightly lower energy with 0.2744 eV. The pure C2/m phase has a significantly higher activation energy of 0.3315 eV, which aligns with the observed low conductivity in this phase.

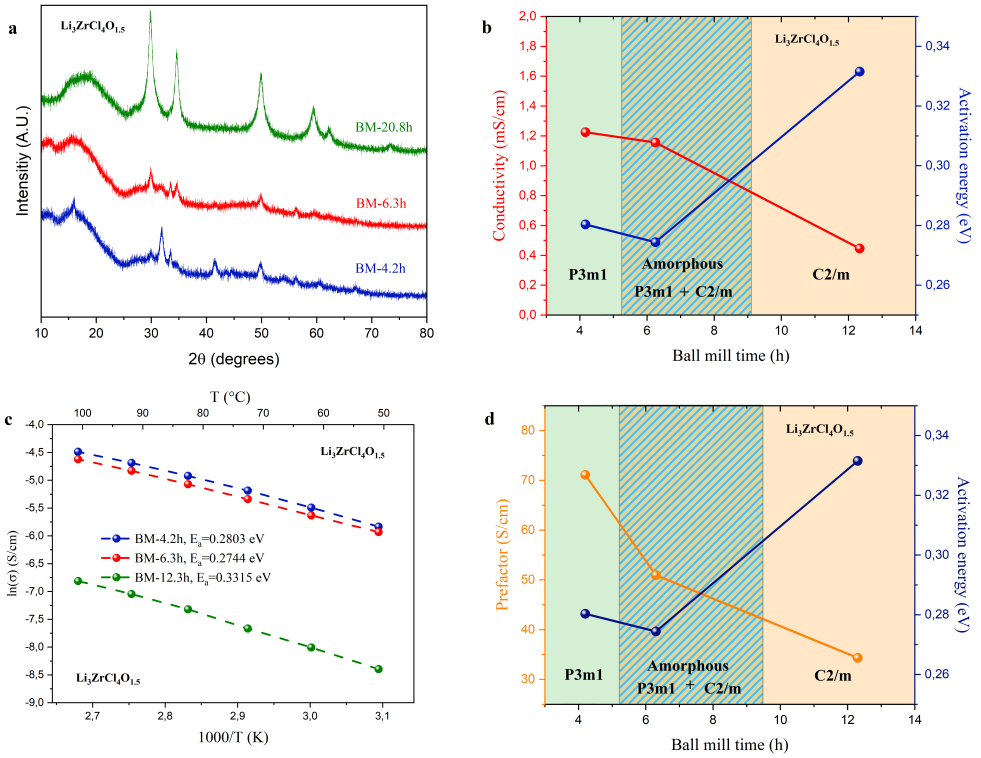

Figure 34: Arrhenius measurements with 4.2h, 6.3h and 20.8h BM $Li_3ZrCl_4O_{1.5}$, (a) corresponding X-ray diffraction patterns, b) corresponding conductivity and activation energy (E_a), c) corresponding conductivities from 50 to 100°C and d) the corresponding pre-factor and E_a.

All conductivities for $Li_{2x}ZrCl_4O_x$

Figure 35 displays the conductivities obtained from the EIS measurements for all the batches synthesized with various compositions of $Li_{2x}ZrCl_4O_x$ in this project. It can be observed that the different batches do not consistently produce identical EIS results for the same ball milling durations. This could be due to a few batches being synthesized with a different number of grinding balls or different cycling rates or speed. It is also noticed in general that each batch behaves differently and the performances differ, making it challenging to replicate measurements, even under the exact same conditions. However, when examining the XRD patterns alongside these measurements, it is usually possible to better understand and explain the resulting conductivity.

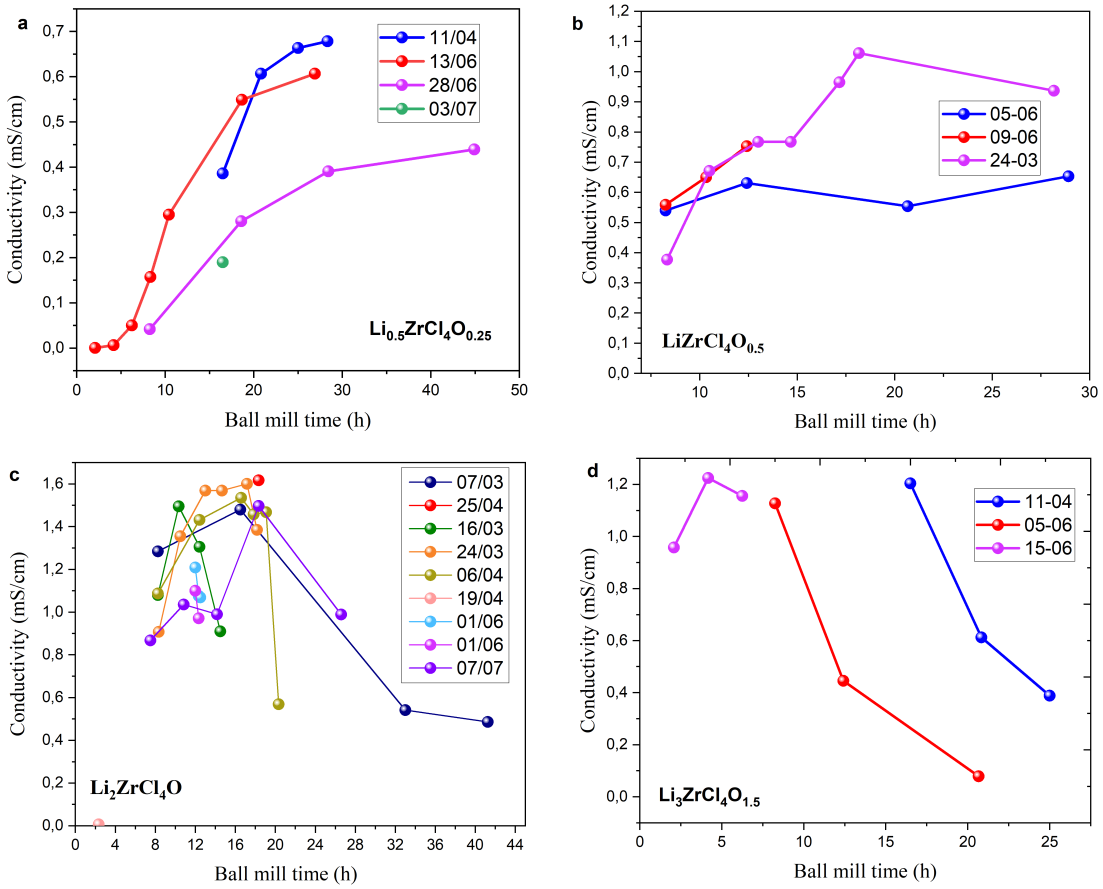

Figure 35: Conductivity measurements of all batches synthesized in the investigation of $Li_{2x}ZrCl_4O_x$ electrolyte with (a) $Li_{0.5}ZrCl_4O_{0.25}$, (b) $LiZrCl_4O_{0.5}$, (c) Li_2ZrCl_4O, and (d) $Li_3ZrCl_4O_{1.5}$.

4.1.4 Stability window analysis of Li_2ZrCl_6, $LiZrCl_4O_{0.5}$, and Li_2ZrCl_4O

As explained in chapter 1.5, the electrochemical stability window is an important parameter in a battery. As within this stability window, a material will not undergo an electrochemical reaction that could hinder the performance of the battery.

In Figure 36a, the Linear Sweep Voltammetry (LSV) plot for Li_2ZrCl_6 reveals that oxidation initiates at approximately 4.142 V vs. Li/Li^+. This suggests that it can be operated up to 4.142 V before any significant reaction occurs. With addition of oxygen the Cyclic Voltammetry (CV) plot for $LiZrCl_4O_{0.5}$ in Figure 36b indicates oxidation starting at around 4.099 V. Additionally, in Figure 36c and d, the LSV and CV curves for Li_2ZrCl_4O are presented, and they show an oxidation potential of 4.033 V and 4.382 V, respectively. This difference in oxidation potential for Li_2ZrCl_4O suggests that a potential error in the synthesis process may have happened, and therefore, this particular data point should be regarded with caution and possibly disregarded.

In general, the addition of oxygen to the chloride-based electrolyte results in a slight decrease in the oxidation potential, in the range of 0.05 to 0.1 V lower than Li_2ZrCl_6. However, this change in oxidation potential is relatively small and may not significantly impact the electrochemical stability window when compared to Li_2ZrCl_6. This suggests that the chloride-based oxyhalide electrolyte could potentially allow the battery to be cycled within a similar voltage range as Li_2ZrCl_6.

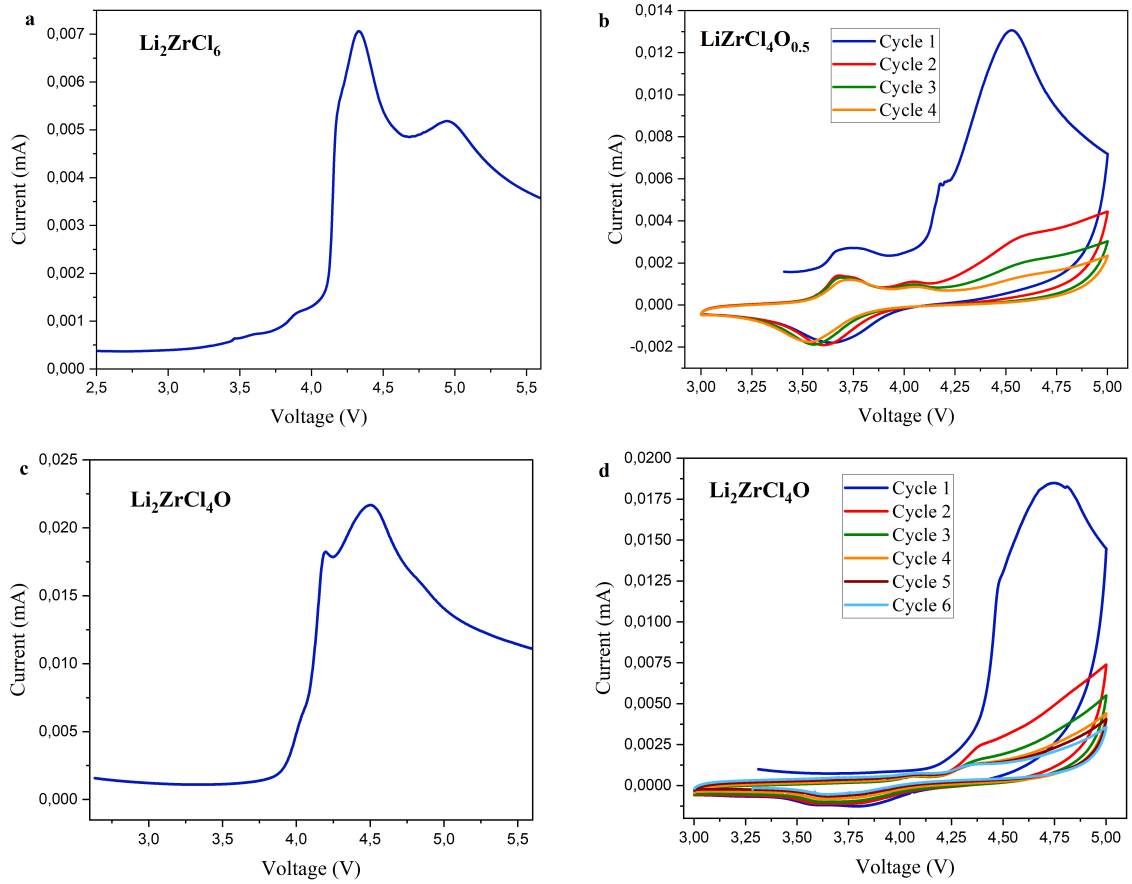

Figure 36: The voltage is vs. Li/Li^+, (a) Linear Sweep Voltammetry (LSV) of Li_2ZrCl_6 and (b) Cyclic voltammetry (CV) of $LiZrCl_4O_{0.5}$ (c) LSV of Li_2ZrCl_4O and (d) CV of Li_2ZrCl_4O.

4.1.5 Morphology analysis of Li_2ZrCl_4O

In a solid structure, particles can be divided into primary and secondary particles. Primary particles are the building blocks of the solid, while secondary particles are an aggregation of primary particles [76].

In order to compare the distinct morphologies of the three identified phases (C2/m, amorphous, and P3m1), scanning electron microscopy (SEM) is employed (see Figure 37). Comparing the amorphous phase with both crystalline phases (C2/m and P3m1), it is observed that the abundance of primary particles is significantly higher in the amorphous phase. A higher number of primary particles could increase the surface area which in turn can increase the interfaces for Li-ion to migrate inside the powder and reach higher conductivities. Furthermore, the comparison between P3m1 and C2/m shows that P3m1 may have a higher concentration of primary particles.

The particle size obtained from the SEM analysis reveals that smaller particles have a range of around 2-4 µm for each phase. For larger particles, C2/m and P3m1 exhibit a size range of 10-15 µm with the amorphous phase exhibiting not many large particles. Additional SEM images can be found in the appendix Figure B.8.

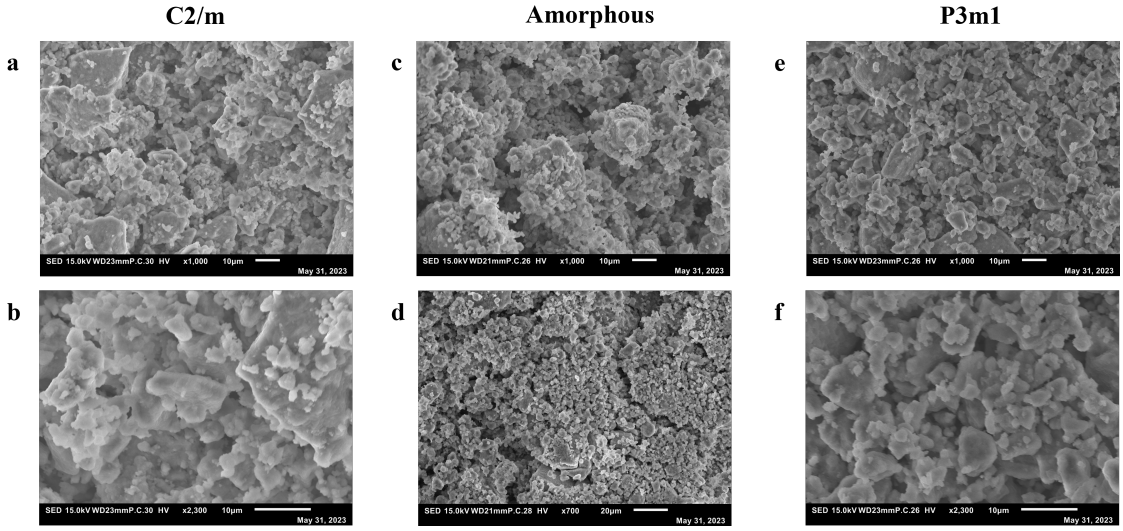

Figure 37: SEM images of Li_2ZrCl_4O with different crystal phases. (a) and (b) are in the C2/m phase, (c) and (d) are in the amorphous phase, (e) and (f) are in P3m1 phase.

4.1.6 Battery cycling performance of Li_2ZrCl_4O

A battery composed of the solid electrolyte Li_2ZrCl_4O is used to test the oxyhalide's long term cycling performances. The battery is composed of 11 mg cathode of NMC/Li_2ZrCl_4O (70 mg NMC and 30 mg Li_2ZrCl_4O), 50 mg of protective layer argyrodite (Li_6PS_5Cl) to prevent reactions with the Li-In anode, 50 mg of Li_2ZrCl_4O electrolyte and Li/In alloy anode (1 mg Li and 40 mg In).

The battery's performance is summarized in Figure 38, which includes voltage profiles with varying numbers of cycles, as well as data on capacity and coulombic efficiency per cycle. The battery is initially activated at 0.05C. After the activation cycles, the battery is charged and discharged at a 0.5C rate, which means it takes 2 hours to charge and 2 hours to discharge fully. The initial charge capacity after the first cycle at 0.5C is 125.6 mAh/g. After 500 cycles, the capacity is 104.55 mAh/g, indicating a capacity retention of 83.24%. After 742 cycles and 1000 cycles, the capacity retention is 77.70% and 67.47% respectively.

These results indicate that the battery maintains its performance even after extended cycling, demonstrating the potential of Li_2ZrCl_4O electrolyte for battery applications.

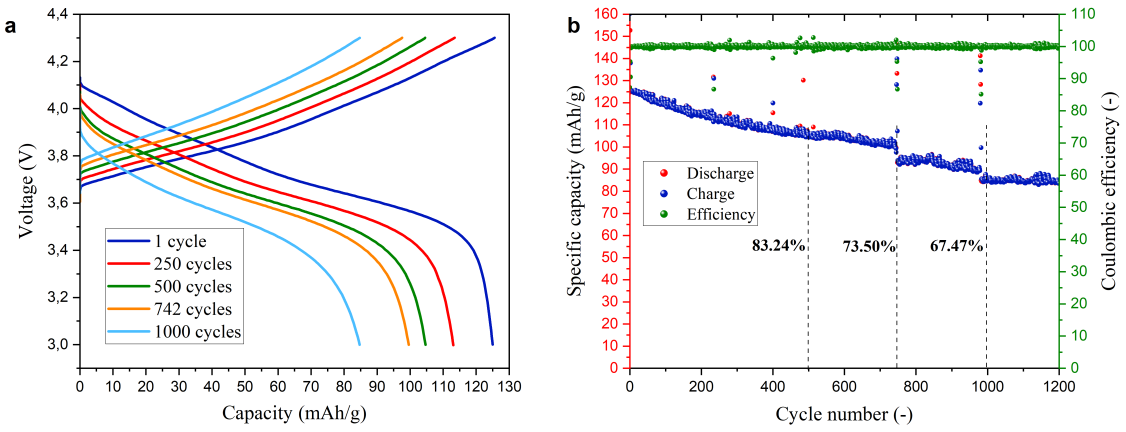

Figure 38: (a) Charge and discharge voltage profiles (vs Li/Li^+) at 0.5C after different cycle amounts, (b) Capacity and coulombic efficiency of ASSB with Li_2ZrCl_4O electrolyte.

4.1.7 Challenges in synthesizing $Li_{2x}ZrCl_4O_x$

The repeatability of batches has proven to be somewhat challenging, as both the XRD patterns and conductivities do not consistently match for different batches with the same duration of ball milling, even when the same parameters are applied. To investigate this issue three separate batches of $LiZrCl_4O_{0.5}$ have undergone BM for 8.3 hours and 16.5 hours as illustrated in Figure B.9. While they exhibit similar structures of C2/m and P3m1, a slight variation in XRD intensities and conductivity is observed. This shows the possible challenge of repeating the same results.

It has also been perceived that achieving the most optimal phase for the highest conductivity is not a simple task. Figure B.10 displays XRD measurements of Li_2ZrCl_4O and indicates a 5.3-hour gap of ball milling time between an almost pure P3m1 and C2/m phase. Within this gap, the coexistence of P3m1, C2/m, and amorphous phases rapidly changes. Obtaining the highest conductivity within this gap is a challenging task that requires careful control. To achieve this, it's necessary to take small BM time steps and closely monitor the structural changes to identify when the desired phase and conductivity are achieved. Additionally, between 19.1 hours and 20.3 hours of ball milling, there is a transition from phase coexistence to almost pure C2/m, revealing how easy it is to overshoot the optimal phase.

Lastly, it is important to assess and compare the performance of different equipment, such as jars used in ball milling processes, to ensure consistency and reliability in materials synthesis. In this case, a direct comparison of the two jars used for all synthesis is made. This is done by synthesizing Li_2ZrCl_4O under identical conditions. The resulting XRD data (see Figure B.11) show similar XRD patterns for both jars after different durations of ball milling, suggesting that the structural phase formation is consistent. However, there is a slight difference in conductivity, with jar 1 showing a conductivity that is 0.1 mS/cm lower than jar 2. This difference could potentially be from a minor error in weighing of the precursors. However, it also suggests the possibility that the two jars may have had a slightly different performance.

4.1.8 Improving synthesis method of $Li_{2x}ZrCl_4O_x$

Instead of direct ball milling of the precursors as is done in the main project, different synthesizing methods of $Li_{2x}ZrCl_4O_x$ are explored. This is done to understand what would be the most efficient synthesizing method considering time and energy.

Synthesis of Li_2ZrCl_4O through hand-grinding or ball milling and subsequent annealing

The first alternative synthesizing approach is to hand grind the powder for 20 minutes and subsequently anneal at varying temperatures. In Figure 39, the conductivity obtained through EIS measurements show a very low ionic conductivity. Even with shorter (5h) and longer (72h) exposure to heat and at higher (500 C°) or lower (200 C°) temperatures the ionic conductivity does not show any considerable improvement. From the XRD it is observed that the structure is well crystallized.

Since the powder is only hand grinded, it might not be mixed enough and as a result, the material may not have a homogeneous composition. As this method results in a very low conductivity, this method is deemed unsuitable and is not further pursued.

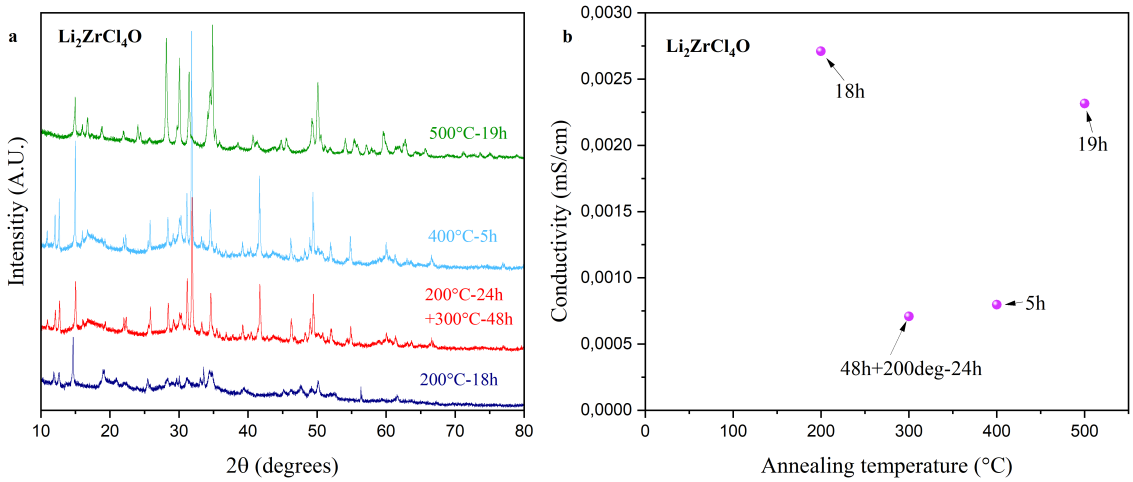

Figure 39: 20 minutes hand grinded Li_2ZrCl_4O and subsequently annealed at different temperatures and annealing times. (a) corresponding XRD patterns and (b) ionic conductivities.

Another synthesizing method attempted is BM of Li_2ZrCl_4O for 8.3 hours and then subsequently annealed. In Figure 40, the XRD and EIS results are displayed with an annealing temperature of 150 C° for 48 hours. The conductivity, after annealing, decreases from around 1.1 mS/cm to 5.38x10^{-5} mS/cm (equivalent to 730Ω), representing a significant decline in conductivity. Consequently, this method is also deemed unsuitable for a more efficient synthesis process.

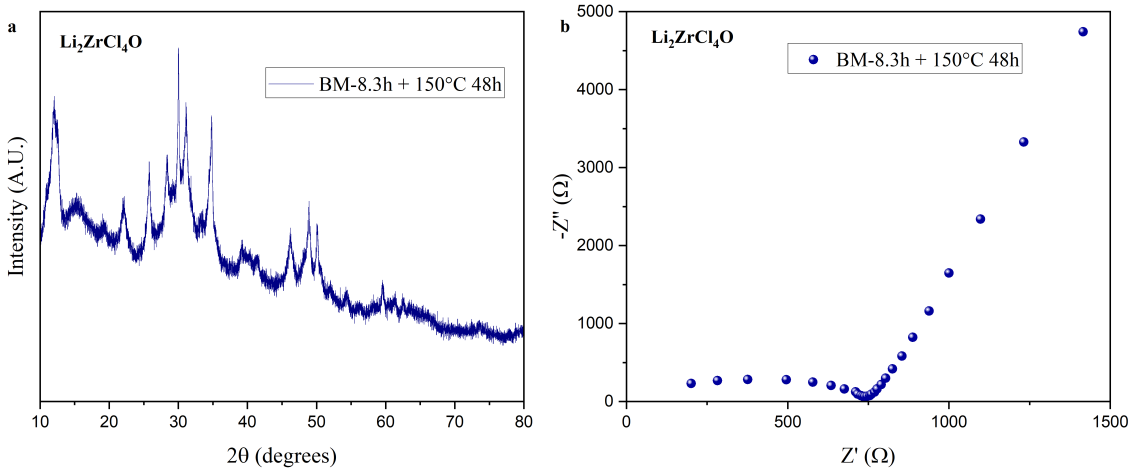

Figure 40: Li_2ZrCl_4O is ball milled for 8.3h and followed by annealing at 150 C°. (a) XRD pattern and (b) ionic conductivity.

4.1.9 Improving $Li_{2x}ZrCl_4O_x$ performance

Different pathways are explored to improve the $Li_{2x}ZrCl_4O_x$ electrolyte's performance. These include investigating into alternative precursors ($Li_2ZrCl_5O_{0.5}$ and $Li_2ZrCl_4O_2$), substitute halides (with Fluoride), sodium based electrolyte (Na^+) and doping with metals (Y^{3+}, La^{3+}, V^{4+} and Ta^{5+}).

LiCl precursor addition ($Li_2ZrCl_5O_{0.5}$)

An alternative composition is explored using precursors LiCl, Li_2O and $ZrCl_4$ resulting in $Li_2ZrCl_5O_{0.5}$. As shown in Figure 41, the resulting structure after 8.25h of BM is P3m1, and with increasing BM time

up to 14.5 hours, there doesn't seem to be any amorphization, and the conductivity stabilizes at around 1.25 mS/cm. Both synthesized batches exhibit the same P3m1 phase and almost the same conductivity. Although it seems the amorphous phased structure will not form and a conductivity plateau is reached, further investigation with longer ball milling times could be interesting to confirm this and understand what the influence of LiCl is. As it seems it might favor the P3m1 structure formation.

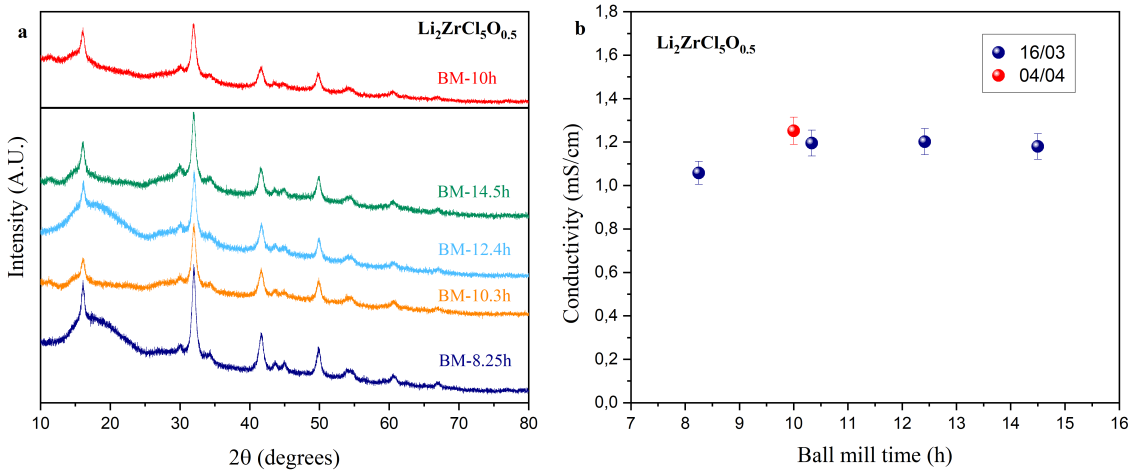

Figure 41: BM samples of $Li_2ZrCl_5O_{0.5}$, (a) XRD patterns of both batches and (b) conductivities of both batches.

LSV and CV measurements are conducted on $Li_2ZrCl_5O_{0.5}$ to see how this compares to the main Zr-based oxyhalide investigated in this report. As expected, from both the LSV and CV an oxidation potential is observed at around 4.019 V which is similar to the previously synthesized oxyhalides 4.1.4.

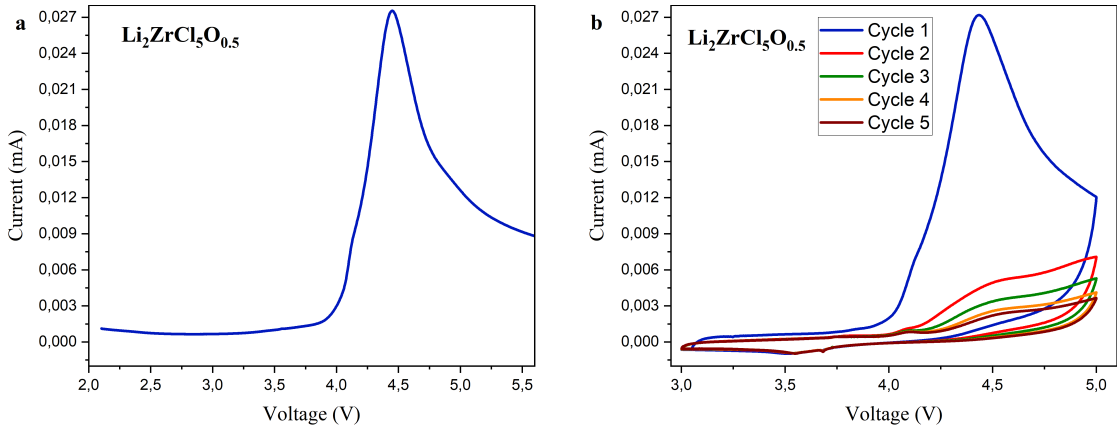

Figure 42: (a) Linear Sweep Voltammetry of $Li_2ZrCl_5O_{0.5}$ and (b) Cyclic Voltammetry of $Li_2ZrCl_5O_{0.5}$.

Trivalent Y doping (YCl_3)

Instead of Zirconium (Zr^{+4}), Yttrium (Y^{3+}), known to also have decent conductivity in electrolytes, is employed as a dopant by utilizing YCl_3 as the precursor [13]. The XRD analysis, depicted in Figure 43, shows that synthesized Li_2YCl_3O has a distinct crystal structure compared to the Zr-based electrolyte. However, the measured conductivity of the Y-doped electrolyte is very poor.

The introduction of metal ions through doping can enhance an electrolyte's conductivity by influencing factors like local disorder, introducing vacancies, tuning Li-ion contents and stabilizing crystal phase

structures [77]. Therefore, to explore the potential for improving the conductivity, the electrolyte is slightly doped with Y^{3+} to synthesize $Li_{2.1}Zr_{0.9}Y_{0.1}Cl_4O$.

From Figure 43a the YCl_3 doping does not appear to alter the starting P3m1 structure and the same transitioning towards an amorphous structure is observed. This closely resembles the undoped electrolyte in Figure 30. Interestingly, it might require less BM time to reach the amorphous phase compared to the undoped electrolyte. Since the amorphous phase is achieved after approximately 12h of BM for the doped electrolyte, compared to an average of 17h for the undoped electrolyte. Additionally, the doped electrolyte seems to be reaching an almost fully amorphous structure which is not reachable with the undoped electrolyte. The Li_2O precursor is still present at short BM durations meaning higher BM durations could be needed to introduce the Li_2O precursor in the structure.

The highest conductivity, approximately 1.58 mS/cm, is reached after 10.8h of BM for the doped electrolyte, which is comparable to the highest conductivity achieved for the undoped electrolyte (1.60 mS/cm). Particularly, this peak conductivity coincides with the presence of the P3m1 crystal phase and closeness to the amorphous-dominated phase. Further investigations, including experiments with higher YCl_3 concentrations and longer BM times, could show the impact of doping on the trend of phase changes and conductivity.

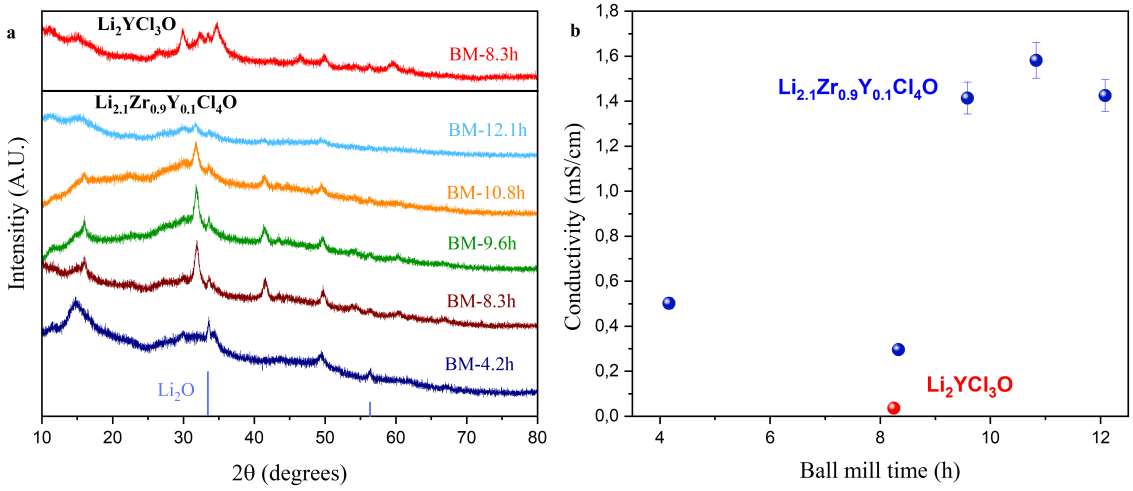

Figure 43: (a) X-ray diffraction measurements and (b) respective ionic conductivity of ball milled synthesized Li_2YCl_3O and $Li_{2.1}Zr_{0.9}Y_{0.1}Cl_4O$.

La-doping ($LaCl_3$)

The potential of incorporating another 3^+ trivalent metal ion, Lanthanum (La^{3+}), into the oxyhalide electrolyte is also investigated. Since a paper from Yu et al. shows that a Lanthanum based electrolyte ($Li_{0.388}Ta_{0.238}La_{0.475}Cl_3$) shows a high conductivity of 3.02 mS/cm and Li-metal stability [78].

The first composition synthesized is Li_2LaCl_3O with precursor $LaCl_3$ mixed with Li_2O. From Figure 44, the XRD data displays a $P6_3/m$ crystal phase after 8.3h of BM. The resulting conductivity is 0.0265 mS/cm and therefore does not seem to have promising performances.

Subsequently, doping with $LaCl_3$ in the Zr-based oxyhalide is explored. The synthesized $Li_{2.5}La_{0.5}Zr_{0.5}Cl_4O$ composition displays a crystal phase similar to the pure lanthanum composition, $P6_3/m$, which appears to be dominant at this concentration. Unfortunately, this composition also yields a very poor conductivity value, indicating that the presence of half of the metal cation being lanthanum may be excessive and detrimental to the conductivity.

The last composition explored is $Li_{0.66}La_{0.5}Z_{0.5}Cl_{3.5}O_{0.33}$ which is a mixture of Li_2O, $LaCl_3$ and $ZrCl_4$.

From Figure 44, this composition also shows $P6_3/m$ crystal phase which differs from the pure Zr-based oxyhalide electrolyte. It again appears that $LaCl_3$ dominates the crystal phase in this composition, and this phase remains unchanged with longer ball milling times. The conductivity, however, seems more promising, with the highest reaching 0.65 mS/cm after 18.9h of BM.

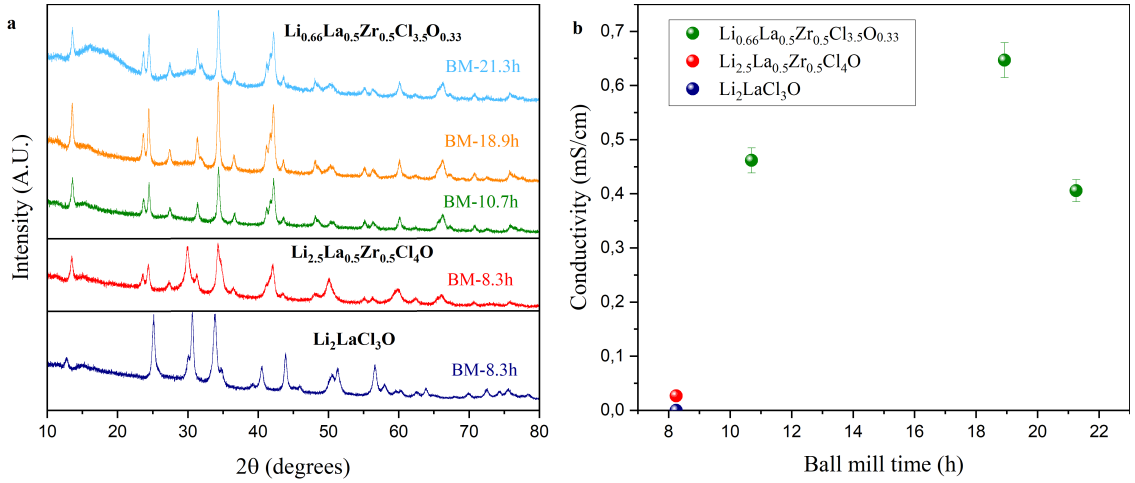

Figure 44: Properties of ball milled synthesized Li_2LaCl_3O, $Li_{2.5}La_{0.5}Zr_{0.5}Cl_4O$ and $Li_{0.66}La_{0.5}Z_{0.5}Cl_{3.5}O_{0.33}$ (a) corresponding X-ray diffraction and (b) conductivity.

Mixed metal electrolyte

As stated before, $Li_{0.388}Ta_{0.238}La_{0.475}Cl_3$ shows promising properties such as high conductivity and stability with Li metal [78]. Therefore, the last doping composition attempted involves $LaCl_3$, $ZrCl_4$, $TaCl_5$ and Li_2O, resulting in the formation of $Li_{0.66}La_{0.5}Zr_{0.25}Ta_{0.25}Cl_{3.75}O_{0.33}$. Additionally, tantalum has been showing very promising conductivities but its main drawback is its scarcity. For this reason only little amount is used for doping the electrolyte.

From Figure 45, it is observed that the resulting crystal structure, for all BM samples, are primarily governed by lanthanum, resulting in a P63/m structure. Despite the dominance of the $LaCl_3$ structure, the conductivity remains high, reaching 1.550 mS/cm after 16.5 hours of ball milling. This high conductivity is likely primarily attributed to the properties of tantalum.

Again, it appears that $LaCl_3$ is governing the crystal structure which might not be the most favorable for ionic conductivity. Therefore, it is interesting for further investigation to dope little amount of tantalum into the Zr-based oxyhalide to explore potential improvements in conductivity.

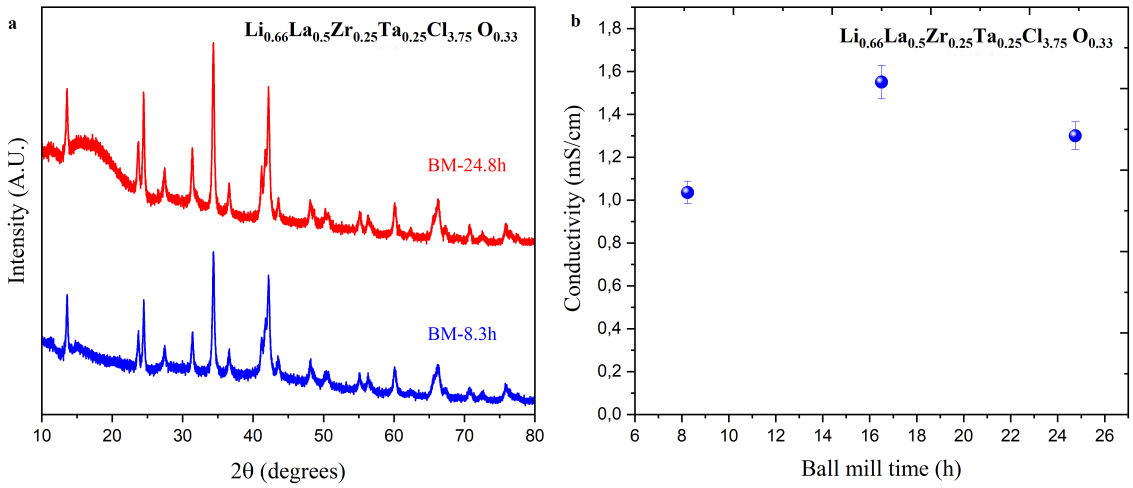

Figure 45: Properties of ball milled synthesized $Li_{0.66}La_{0.5}Z_{0.25}Ta_{0.25}Cl_{3.75}O_{0.33}$ (a) X-ray diffraction and (b) the resulting conductivity.

Additional explored doped and elemental substitution of $Li_{2x}ZrCl_4O_x$ electrolyte

An attempt is made to substitute the chloride halide with fluoride to assess its impact on conductivity and the oxidation potential. This resulted in the following composition, Li_2ZrF_4O. However, Li_2ZrF_4O exhibits terrible conductivity and, as a result, was not investigated further (see Figure B.12).

Another substitution attempt involved replacing lithium with sodium, yielding Na_2ZrF_4O. Sodium is an element that is abundant, cost-effective, and safer. However, after ball milling for 8.3 hours, the resulting conductivity is extremely low, measuring 6.38x10^{-4} mS/cm. The resulting XRD and EIS data are shown in Figure B.13.

In another experiment, the precursor Li_2O_2 is used instead of Li_2O, resulting in $Li_2ZrCl_4O_2$. After ball milling for 8.3 and 16.5 hours, the structural phase identified is C2/m, which has shown to have lower conductivity in this study for the $Li_{2x}ZrCl_4O_x$ electrolyte. Moreover, with increased ball milling, the prevalence of the C2/m phase became more pronounced, indicating no signs of a phase change (see Figure B.14). The resulting conductivities are 0.244 and 0.263 mS/cm, which are significantly lower than those of Li_2ZrCl_4O and other concentrations based on Li_2O precursor.

Finally, metal doping is attempted using vanadium (V^{5+}) to create $Li_{1.6}Zr_{0.6}V_{0.4}Cl_4O$. As shown in Figure B.15, the XRD pattern and corresponding conductivity is displayed. After 8.3 hours of ball milling, a conductivity of 0.161 mS/cm is measured, which is quite low, and therefore further investigation is not continued. Additionally, it's important to note that vanadium 5+ is dangerous for the health.

4.1.10 Li-metal stability

As explained in background 1.2.4, Li-metal as an anode in a battery has several advantages. Li-metal possesses the lowest reduction potential (0 V vs. Li/Li+). This property results in a higher overall cell voltage, leading to increased energy density in the battery. Furthermore, Li-metal can also prevent dendrite formation and has high capacities. These features make Li-metal a highly desirable choice for anode material in battery applications.

For these reasons some synthesized electrolytes from this report are tested for their stability against Li-metal (namely $Li_{1.5}ZrCl_4O_{0.75}$, $Li_{0.66}La_{0.5}Zr_{0.5}Cl_{3.5}O_{0.33}$ and $Li_{0.66}La_{0.5}Z_{0.25}Ta_{0.25}Cl_{3.75}O_{0.33}$). To assess this stability, a symmetrical cell configuration is employed, comprising of an electrolyte layer sandwiched between two Li-metal plates. The results from the measurements are shown in Figure 46. It is evident that the oxyhalide electrolytes exhibit instability when in contact with Li-metal. As with application

of a current and cycling, the voltage is progressively increasing, indicative of reactions occurring at the interface between the electrolyte and the Li-metal electrodes. This reaction is not wanted since it has the potential to increase internal resistance and decrease battery efficiency. Additionally, $Li_{2.5}La_{0.5}Zr_{0.5}Cl_4O$ is also measured with a symmetric cell, and an initial high overpotential (4.1 V vs. Li/Li^+) during the first cycle is observed.

Unfortunately, from these measurements it can be concluded that the oxyhalides synthesized in this report are not stable against Li-metal.

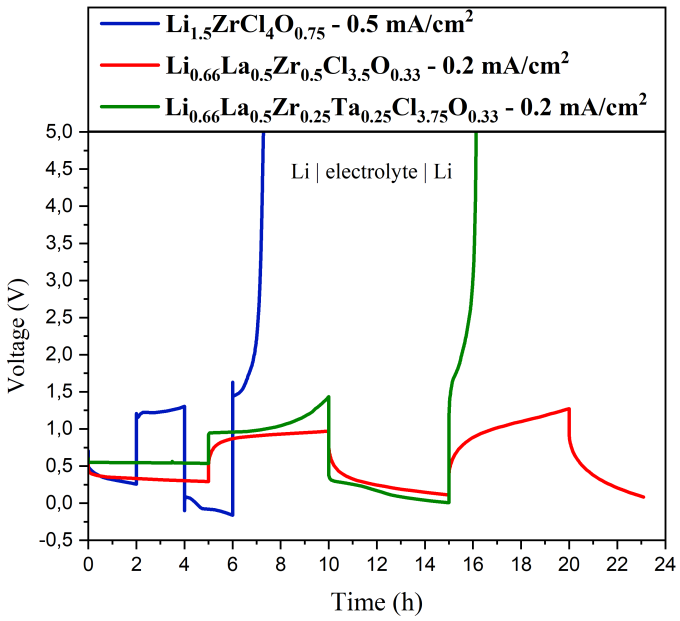

Figure 46: The voltage profiles of the cell configuration of $Li|Li_{1.5}ZrCl_4O_{0.75}|Li$, $Li|Li_{0.66}La_{0.5}Z_{0.5}Cl_4O_{0.33}|Li$ and $Li|Li_{0.66}La_{0.5}Z_{0.25}Ta_{0.25}Cl_{3.75}O_{0.33}|Li$ during galvanostatic cycling measurement at a current density of 0.5 mA/cm^2, 0.2 mA/cm^2 and 0.2 mA/cm^2 respectively.

4.1.11 Conclusion of Zr-based oxyhalides

This work explores the O-doping effect on Zr-based halide solid electrolyte, specifically $Li_{2x}ZrCl_4O_x$ (x= 0.25, 0.5, 1 and 1.5), which is synthesized with Li_2O and $ZrCl_4$. These are subjected to different ball milling (BM) times and are additionally doped with various metals. Here, the most interesting results and findings are summarized.

The reason to investigate Zr-based electrolytes is due to the cost-effectiveness of $ZrCl_4$ (as low as 12.50 USD/kg), its widespread industrial use, and the abundance of Zr in the Earth's crust (165 mg/kg), making this electrolyte suitable for large-scale production. Li_2ZrCl_6 has also shown reasonable conductivities of 0.81 mS/cm achieved after 45 hours of BM [77].

The first aim was to replicate the impressive performance observed of amorphous $LiTaCl_5O_{0.5}$ by Ishiguro et al., achieving a conductivity of 8.92 mS/cm with 200h of BM followed by annealing. However, the highest conductivity achieved in this project is 3.5 mS/cm with 16.5h of BM. Prolonged BM times reveal the presence of poorly conductive ZrO_2 from the BM balls. Nevertheless, these promising results have led to the investigation of the cost-effective zirconium oxyhalide: $Li_{2x}ZrCl_4O_x$.

In terms of phase structure, $Li_{2x}ZrCl_4O_x$ exhibited an initial phase of either C2/m or P3m1, which subsequently transformed into an amorphous structure and, after longer BM times, became P3m1 or C2/m. The initial phase appeared to be influenced by the oxygen (O) content, with lower O contents (x = 0.5 and 1) exhibiting a C2/m phase before transitioning to a fully amorphous phase and, with longer BM

times, P3m1. In contrast, higher O contents (x = 2 and 3) initiated with P3m1 phase and shifted to a coexistence of P3m1, amorphous, and C2/m before ultimately forming a dominating C2/m phase. This re-crystallization phenomena may be related to prolonged exposure to high mechanical energy.

Considering conductivity, Li_2ZrCl_6 exhibited a conductivity of 0.48 mS/cm after 8.3h of BM with a P3m1 phase. With the introduction of Li_2O precursor, $Li_{0.5}ZrCl_4O_{0.25}$ and $LiZrCl_4O_{0.5}$ achieved a fully amorphous structure with the highest conductivity of 0.68 mS/cm after 28.3h BM and 1.06 mS/cm with 18.2h BM, respectively. Li_2ZrCl_4O achieved 1.6 mS/cm with 17.2h BM, and $Li_3ZrCl_4O_{1.5}$ reached 1.23 mS/cm after 4.2h BM characterized by a mixed phase dominated by the P3m1 and amorphous structures.

In general, the amorphous phase enhances conductivity compared to the crystalline structures, possibly through increased space for Li-ion movement and a hopping mechanism facilitating ion mobility. However, comparing all compositions, the most amorphous ones (x = 0.25 and 0.5) do not exhibit the highest conductivity. It appears that the O content has a dual impact: it affects the degree of amorphization and the concentration of Li-ions (where higher Li-ion concentration typically results in a greater number of active Li-ions contributing to the conductivity). This results in a trade-off.

It is observed that Li_2ZrCl_4O and $Li_3ZrCl_4O_{1.5}$ still have slight Li_2O precursor that did not incorporate into the structure. Only after long BM time Li_2O does get incorporated into the C2/m structure. This suggests that higher conductivities can be reached if all Li_2O is incorporated for these compositions, since Li_2O is poorly conductive.

Refinement measurements revealed that ball milled Li_2ZrCl_4O exhibiting 57% of the amorphous phase and 43% P3m1 content displayed higher conductivity compared to 57% of the amorphous and 43% C2/m content, confirming the lower conductivity of the C2/m phase. Furthermore, the amorphous phase is responsible for increasing conductivities. This trend is the opposite of typical halide electrolytes, where the C2/m phase usually exhibits the highest conductivity.

The crystallinity of $Li_{2x}ZrCl_4O_x$ can be tuned both through the presence of oxygen content and the ball milling durations. Additionally, slight 3+ yttrium doping ($Li_{2.1}Zr_{0.9}Y_{0.1}Cl_4O$) enhanced amorphization and achieved a conductivity of 1.58 mS/cm after only 10.8h of BM, suggesting that less BM time might be needed to reach the ideal phase.

Regarding the oxidation potential, Li_2ZrCl_6 exhibited a potential of 4.142 V vs. Li/Li^+ compared to $LiZrCl_4O_{0.5}$, which exhibited an oxidation potential of 4.099 V, and Li_2ZrCl_4O of 4.033 V, indicating that the introduction of oxygen might slightly lower the oxidation potential. It is possible that cycling can be done above this voltage as seen with pure chloride-based electrolytes. Moreover, CV measurements indicate the formation of an interlayer suggesting that the reaction may not significantly impact battery cycling at higher voltages. Lastly, the oxyhalides based on Zr did not show Li-metal stability, both doped and undoped.

To reduce oxygen content while maintaining a high Li content, the electrolyte $Li_2ZrCl_5O_{0.5}$ was investigated, incorporating LiCl, Li_2O, and $ZrCl_4$. However, with BM times up to 14.5h, no signs of amorphization are observed, and a P3m1 phase is identified. The conductivity stabilizes at around 1.25 mS/cm, and the oxidation potential is observed at 4.019V, similar to the other oxyhalides investigated.

The battery cycling performances are promising, with Li_2ZrCl_4O as an electrolyte exhibiting an initial capacity of 125.6 mAh/g at 0.5C and retaining 67.47% capacity after 1000 cycles.

4.2 Mixed halide electrolyte

For the second part of this project an Y-based mixed halides electrolyte is investigated. The reason for studying Y-based electrolyte is that it exhibits the highest conductivity amongst halide electrolytes (5.36 mS/cm for $Li_3YBr_{4.5}Cl_{1.5}$) [65]. Additionally, in terms of cost, yttrium is the second cheapest metal element that is employed in all halide electrolytes (YCl_3 with 330 USD/kg) and considering abundance it is more abundant than most other metals employed with 33 mg/kg in the earth's crust [24, 26].

Additionally, previous work by van der Maas et al. has shown that mixed Cl-Br halide ($Li_3YCl_3Br_3$) electrolyte exhibits substantially increased conductivity compared to a pure Cl electrolyte (Li_3YCl_6), with only a marginal reduction in oxidative stability [65]. Moreover, with limited Br-doping ($Li_3YBr_{1.5}Cl_{4.5}$), the oxidation potential is not affected, however, the conductivity increases considerably from 0.049 to 2.1 mS/cm at 30 °C compared to Li_3YCl_6. Therefore, by incorporating multiple halogen elements and tuning the anion ratio, it may be feasible to achieve an optimal mix of halides which optimizes both conductivity and electrochemical stability. This leads to the investigation of electrolyte $Li_3YCl_3Br_{3-x}I_x$ with x=0, 0.2, 0.4, 0.6, 0.8 and 1.

4.2.1 Annealing temperature optimization for $Li_3YCl_3Br_2I$

The first step in this part of the project is to synthesize $Li_3YCl_3Br_2I$. The ball milling (BM) parameters are set at a consistent duration of 8.3 hours in this experiment. This duration appears to result in a well-crystalline structure, which will be discussed in more detail later. Following BM, the samples are subjected to an annealing process. To determine the most optimal annealing temperature and time, various annealing temperatures are tested in the synthesis of $Li_3YCl_3Br_2$.

Annealing temperatures between 150°C and 500°C are used with a consistent annealing time of 5h (besides for 150°C that is 12h). In Figure 47, the resulting XRD measurements and conductivities are shown. From the XRD measurements, it is observed that annealing temperatures higher than 200°C lead to XRD peaks with very high intensities and a decrease in impurities. This suggests that the structure at these temperatures may be more ordered and crystalline. In contrast, at 150°C, the structure appears less crystalline.

From the conductivity measurements the highest conductivity is achieved at annealing temperature of 400°C for 5h with 3.74 mS/cm. However, the sample annealed at 300°C for 5h also exhibits a very high conductivity of 3.25 mS/cm. Considering that there is a 100°C difference in annealing temperature for a gain of 0.49 mS/cm in conductivity, the 300°C temperature is selected as the annealing temperature to investigate. This decision is based on the idea that it requires less energy to produce the electrolyte at this temperature while maintaining excellent conductivity

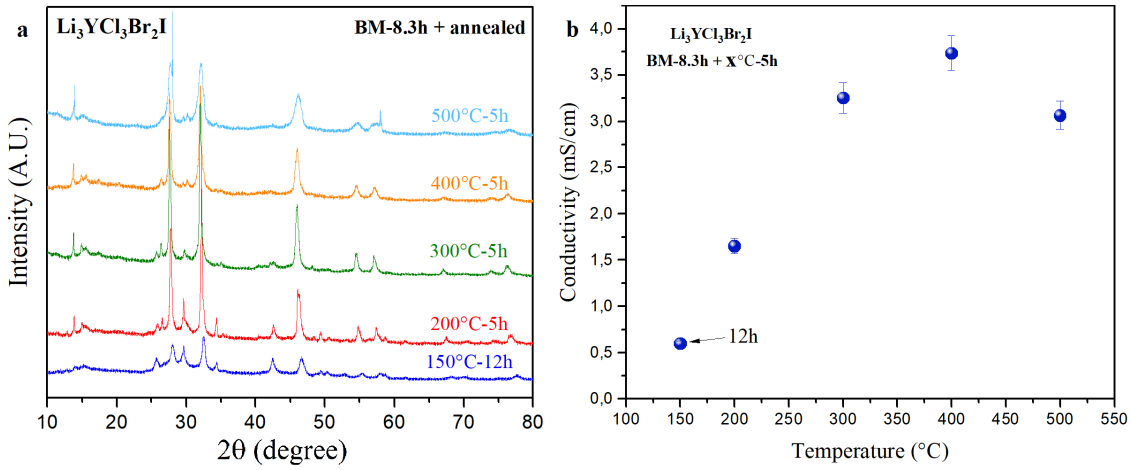

Figure 47: Finding the optimal annealing temperature for $Li_3YCl_3Br_2I$ with (a) the XRD measurements and (b) the resulting conductivities.

4.2.2 Annealing time optimization for $Li_3YCl_3Br_2I$

With the optimal annealing temperature determined, the subsequent investigation aims to identify the most effective annealing time. Various time durations ranging from 5 minutes to 5 hours are examined. XRD measurements, as depicted in Figure 48a, reveal minimal distinctions in structural phases across these different durations. However, there are differences in conductivity (see Figure 48b).

Interestingly, a short annealing duration of 5 minutes at 300°C exhibits the highest conductivity at 3.55 mS/cm, followed closely by 15 minutes at 3.30 mS/cm, and 5 hours at 3.25 mS/cm. The high conductivity achieved with 5-minute annealing period could mean that this short annealing time leads to removal of defects or disordered regions within the material. This phenomenon likely contributes to an enhancement in conductivity by addressing certain crystal imperfections, thereby facilitating improved ion mobility.

Considering the advantages of shorter annealing times, such as reduced energy consumption, greater time efficiency in production and importantly having the highest conductivity, the annealing time of 5 minutes is selected as the optimal time for all halide electrolyte compositions. Furthermore, an additional sample is annealed at 400°C for 5 minutes, revealing no significant differences in crystal structure or conductivity.

It is intriguing that a decline in conductivity is observed with a 3-hour annealing period, followed by an increase in conductivity with more extended annealing times. After 3h of annealing new impurity peaks are formed due to for example elements migrating out of the structure with long exposure to heat. As the annealing time increases, the effects of crystallization may become more pronounced than the impurities created, leading to an increase in conductivity.

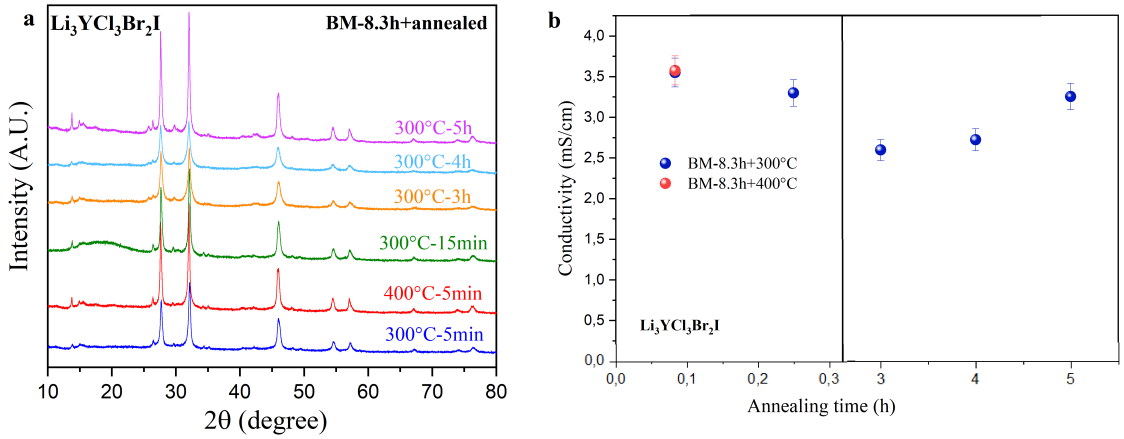

Figure 48: Finding the optimal annealing time at 300°C for $Li_3YCl_3Br_2I$ with (left) the XRD measurements and (right) the resulting conductivities.

4.2.3 Properties of 8.3h ball milled and 300°C for 5 minutes annealed $Li_3YCl_3Br_{3-x}I_x$

This part of the project focuses on the $Li_3YCl_3Br_{3-x}I_x$ electrolyte with varying iodide (I^-) concentrations (x=0, 0.2, 0.4, 0.6, 0.8, and 1). The synthesis is conducted by initial ball milling for 8.3 hours followed by annealing at 300°C for 5 minutes. In Figure 49, crystal structure of $Li_3YCl_3Br_3$ and $Li_3YCl_3Br_2I$ are displayed which both exhibit a C2/m structure.

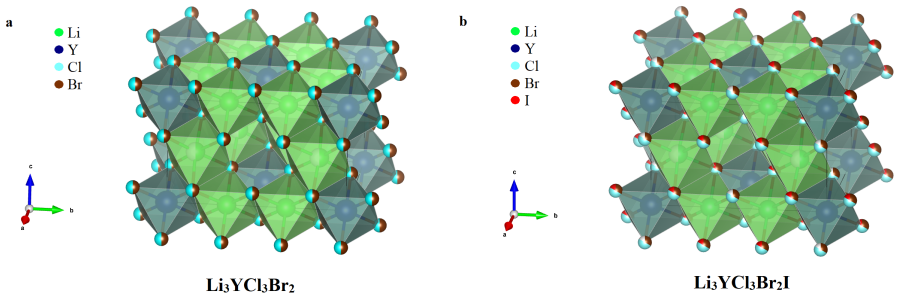

Figure 49: C2/m structure of (a) $Li_3YCl_3Br_3$, and (b) $Li_3YCl_3Br_2I$ after 8.3h of ball milling and annealing at 300°C for 5 minutes.

Figure 50 shows the XRD measurements for the BM samples, BM and subsequently annealed samples, resulting lattice parameters and the corresponding conductivities. The BM samples exhibit a C2/m crystal phase for all iodide concentrations as seen in Figure 50a. However, the addition of iodide results in a left peak shifting in the XRD patterns, indicating lattice relaxation. This shift is attributed to the larger ionic radius of iodide ($r_{I^-} = 202$ pm) compared to bromide ($r_{Br^-} = 182$ pm), causing the lattice to expand when this iodide is inserted in the lattice. Upon BM and subsequent annealing, similar phase structures (C2/m) are observed for each iodide content (see Figure 50b). However, annealed samples display narrower peaks, suggesting improved crystallinity and reduction of defects.

The lattice parameter c of each iodide content is shown in Figure 50c. This is determined through refinement using GSAS II software. The lattice parameters consistently increase with the addition of iodide and the removal of bromide. This expansion in lattice parameters corresponds to the observed leftward peak

shift in the XRD patterns and also results in an increase in volume of the unit cell. The lattice parameters a and b can be found in Table 7 and the fitted XRD patterns with GSAS II are shown in Figure C.1.

Conductivity measurements (Figure 50d) reveals two notable trends. Firstly, annealing consistently enhances conductivity, indicating the removal of defects during annealing. Secondly, an increase in iodide content leads to higher conductivity. As seen with x=0 the conductivity is 1.94 mS/cm while x=0.8 and x=1 the conductivity is 2.85 mS/cm and 3.55 mS/cm respectively. This effect is anticipated since iodide's larger ionic radius allows for more charge carriers per unit volume and promotes greater ionic mobility by reducing interactions with surrounding ions. This is based on the increase of the bottleneck size and allows Li-ions to pass through more easily which has a direct impact on activation energy and, consequently, ionic conductivity. However, at x=0.2 (low iodide concentration), the doping effect on conductivity appears negligible as conductivity is 1.63 mS/cm, suggesting that this concentration might not significantly alter the bottleneck size.

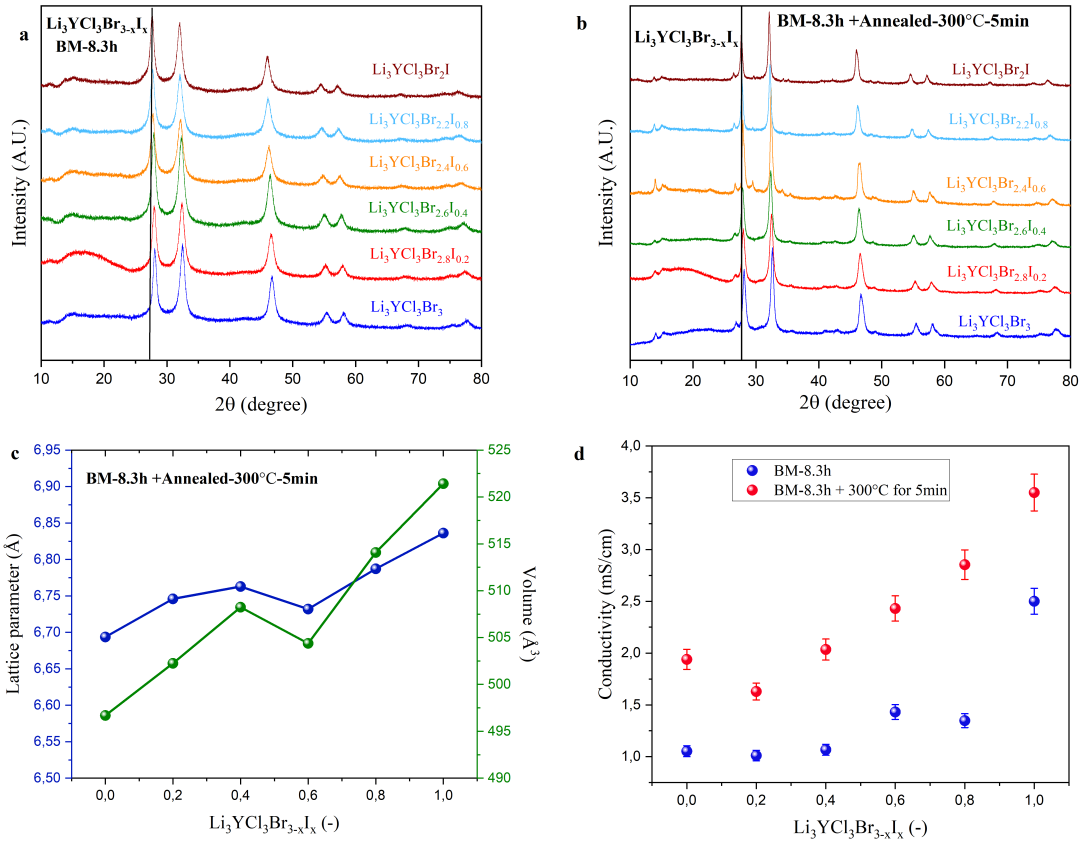

Figure 50: (a) X-ray diffraction (XRD) patterns of ball milled (BM) $Li_3YCl_3Br_{3-x}I_x$ for 8.3 hours, (b) XRD patterns of BM $Li_3YCl_3Br_{3-x}I_x$ for 8.3 hours and subsequent annealing for 5 minutes at 300°C, (c) Results from refinement of $Li_3YCl_3Br_{3-x}I_x$ XRD patterns with GSAS II, (d) Resulting conductivities of BM, and BM with subsequent annealing of $Li_3YCl_3Br_{3-x}I_x$.

4.2.4 Electrochemical stability window of $Li_3YCl_3Br_{3-x}I_x$

The electrochemical stability window of $Li_3YCl_3Br_{3-x}I_x$ with x=0, 0.2, 0.4, 0.6, 0.8 and 1 is examined to gain insights into how iodide doping influences the oxidation potential. Figure 51 displays the linear sweep voltammetry (LSV) results for all concentrations along with their corresponding oxidation potentials relative to their conductivity.

In Figure 51a, the LSV measurements reveal a clear trend where the current onset occurs at lower voltages

as the iodide content increases. The onset of current delimits the oxidation potential that refers to how easily an element can lose an electron. This trend is expected due to the larger ionic radius of iodide compared to bromide, as previously discussed. The greater distance between the outermost electron of iodide and its nucleus makes it easier for iodide ions to undergo oxidation by losing an electron. Additionally, the current generated from iodide oxidation is highest for the highest iodide content which might signify that a higher iodide content provides more iodides available for oxidation.

In Figure 51b, the oxidation potential for the sample with no iodide (x=0) is 3.59 V vs. Li/Li^+ (V), compared to 3.474 V for x=1. However, at x=0.6, the oxidation potential is 3.451 V, not following the expected trend. This anomaly could be attributed to potential errors during the powder synthesis process. Comparing oxidation potential against conductivity clearly demonstrates that iodide improves ionic conductivity but reduces the oxidation potential. Notably, the increase in ionic conductivity from x=0 to x=1 is substantial, with values of 1.94 mS/cm and 3.55 mS/cm, respectively. In contrast, the change in oxidation potential is less pronounced, going from 3.59 V to 3.474 V. This suggests that iodide's effect on conductivity is more significant than its impact on the electrochemical stability window.

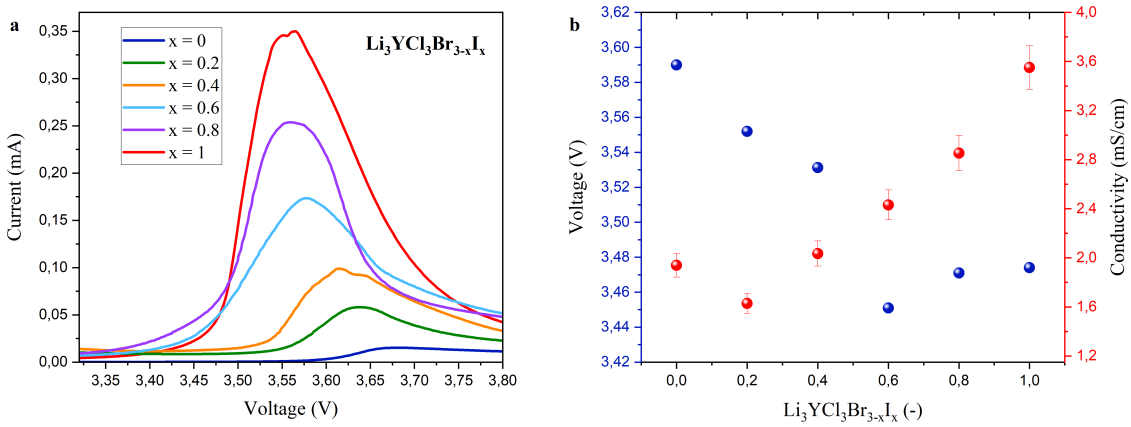

Figure 51: (a) Linear sweep voltammetry of $Li_3YCl_3Br_{3-x}I_x$ with x=0, 0.2, 0.4, 0.6, 0.8 and 1 with voltage vs Li/Li^+, (b) the resulting oxidation potentials and their respective conductivity after BM for 8.3 hours and annealing at 300°C for 5min.

A cyclic voltammetry (CV) measurement is made for $Li_3YCl_3Br_2I$ and is shown in Figure 52a. The first cycle exhibits a clear oxidation peak at around 3.4V vs. Li/Li^+. Upon the next cycles, it seems a stable interlayer is created due to the formation of stable products that prevent further oxidation of the bulk material. As in the subsequent cycles, the resulting current is very low (see Figure 52b). This characteristic could be advantageous in a full battery, suggesting that the electrolyte can remain stable above this voltage.

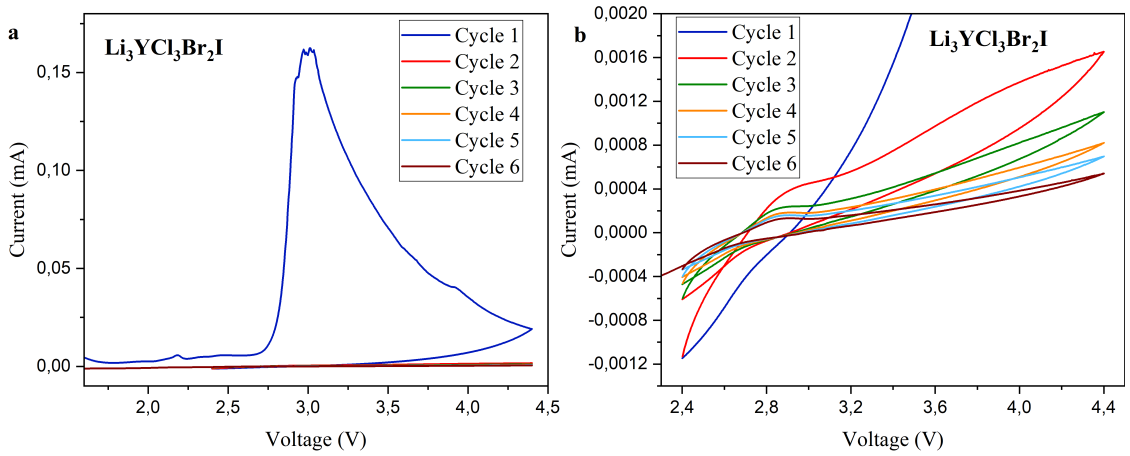

Figure 52: (a) Cyclic voltammetry (CV) of $LiY_3Cl_3Br_2I$ and (b) zoomed in on the last five cycles of the CV.

4.2.5 X-ray Photoelectron Spectroscopy of pristine and cycled $Li_3YCl_3Br_2I$

The electron configuration of chloride is $1S^2\ 2S^2\ 2P^6\ 3S^2$, bromide is [Ar] $4s^2 3d^{10} 4p^5$ and iodide is [Kr] $4d^{10} 5s^2 5p^5$. With X-ray Photoelectron Spectroscopy (XPS) measurements, the core level orbital is analyzed and is based on the energy required to eject an electron from this orbital. For chloride the 2p orbital (Cl2p) is used as reference, meaning that the binding energy associated with the 2p subshell of chlorine is looked at. For bromide and iodide it is Br3d and I3d respectively.

All orbitals, except for the s-orbitals, exhibit a doublet (meaning there are two different energies) and they possess a specific different binding energy. This difference between the two peaks is a characteristic for each element and is referred here as Δ. Additionally, typically the binding energy in a doublet is selected to be the peak with the highest intensity. From the NIST XPS Database, the -1 oxidation state of chloride, bromide, and iodide showcase binding energies of approximately 198.5–199 eV (Clp3/2), 68.7 eV (Br3d5/2), and approximately 619 eV ($I3d_{5/2}$), respectively. Meanwhile, Δ is 1.6 eV, 1.04 eV, and 11.5 eV, respectively. Lastly, a binding energy of 619.9 eV for iodide with an oxidation number of 0 is reported [79].

In theory, iodide should undergo oxidation at a lower voltage compared to chloride and bromide due to its larger atomic size and greater electron shielding. With Linear Sweep Voltammetry the oxidation potential of an electrolyte is explored, while XPS serves to confirm which element undergoes oxidation first. Experimental XPS data is presented in Figure 53. Figure 53a and 53b depict the chloride and bromide doublet peaks, corresponding to Cl^- and Br^-, respectively. Table 6 shows (Δ) values for chloride and bromide, that are around literature values of 1.6 eV and 1.04 eV. The bonding energies of Cl^- and Br^- from literature closely match the measured binding energies with 198.59 eV and 68.62 eV, confirming the absence of oxidation for these elements. Additionally, the peaks remain unchanged between the pristine and post-LSV electrolyte meaning no oxidation has undergone.

The expectation of iodide oxidizing first is being confirmed. In Figure 53c, 4 peaks are observed corresponding to the 2 doublets of I(0) (in red) with a measured binding energy of ≈620 eV, while the peaks in green represent I^-, exhibiting a binding energy of 618.9 eV. These are similar to the literature values (619.9 eV and 619 eV, respectively). Both I(0) and I^- exhibit a Δ binding energy around 11.5 eV, characteristic for the iodide element.

When comparing the pristine and post-LSV XPS data for iodide, a clear increase of the intensity of the red peaks is observed. This signifies an increase in the presence of oxidized I(0), while the intensity of I^- decreases. Consequently, this means that iodide is the first element to undergo oxidation with increasing

the cell voltage. Lastly, it is interesting to note that there is already some iodide with oxidation state of 0 in the pristine cell meaning that the iodide might have LiI reacted with air to form elemental iodide (I_2).

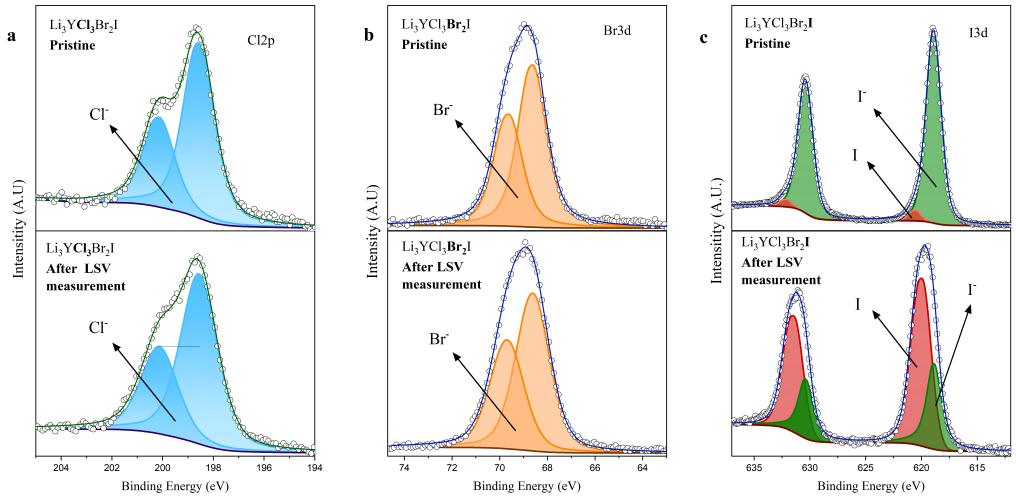

Figure 53: XPS analysis results comparing the pristine and post-LSV (Linear Sweep Voltammetry) measurements of the $Li_3YCl_3Br_2I$ electrolyte. Shown are XPS spectra for (a) chloride (Cl2p), (b) bromide (Br3d), and (c) iodide (I3d) elements.

Table 6: XPS analysis results comparing the pristine and post-LSV (Linear Sweep Voltammetry) measurements of the $Li_3YCl_3Br_2I$ electrolyte. The respective binding energies from the XPS measurements and literature are shown with its intensities of chloride (Cl2p), bromide (Br3d), and iodide (I3d) elements.

	Chloride (Cl2p)		**Bromide (Br3d)**		**Iodide (I3d)**			
State	Pristine	Post LSV	Pristine	Post LSV	Pristine		Post LSV	
Binding energy (eV)	200.18-**198.59**	200.15-**198.59**	69.66-**68.63**	69.69-**68.62**	630.43-**618.91**	632.16-**620.60**	630.42-**618.92**	631.52-**620.02**
Δ binding energy (eV)	1.59	1.55	1.03	1.07	11.52	11.56	11.52	11.52
Literature Δ binding energy (eV)	1.6		1.04		11.5			
Intensity (A.U.)	13020-16339	12889-16714	8394-10494	8535-10787	69456-86463	27809-24257	25035-26570	31668-35529

4.2.6 Doping with fluoride in $LiY_3Cl_3Br_2I$

In the final experiment of this project, $LiY_3Cl_3Br_2I$ is doped with fluoride to examine its effect on the electrochemical stability window. In theory, fluoride should increase the stability window but decrease the conductivity because fluoride has the smallest ionic radius among the halides.

From Figure 54, the XRD pattern of LiY_3FCl_3Br is shown exhibiting a structure with low ionic conductivity after ball milling (BM) for 8.3 hours. Since a very low conductivity is measured, the next composition is prepared with half the amount of fluoride, resulting in $Li_3YF_{0.5}Cl_3Br_2I_{0.5}$. Initially, it is subjected to BM for 8.3 hours and exhibits a crystalline C2/m phase, suggesting that the fluoride structure is not dominant, with a conductivity of 0.67 mS/cm.

Upon annealing for 5 minutes at 300°C, the C2/m structure is maintained but appears to be more crystallized, and the conductivity increases significantly to 2.14 mS/cm. However, it is observed that the oxidation potential does not change significantly, measuring at 3.54 V vs. Li/Li^+. This is close to what has been observed with $LiY_3Cl_3Br_{2.6}I_{0.4}$ (3.531 V).

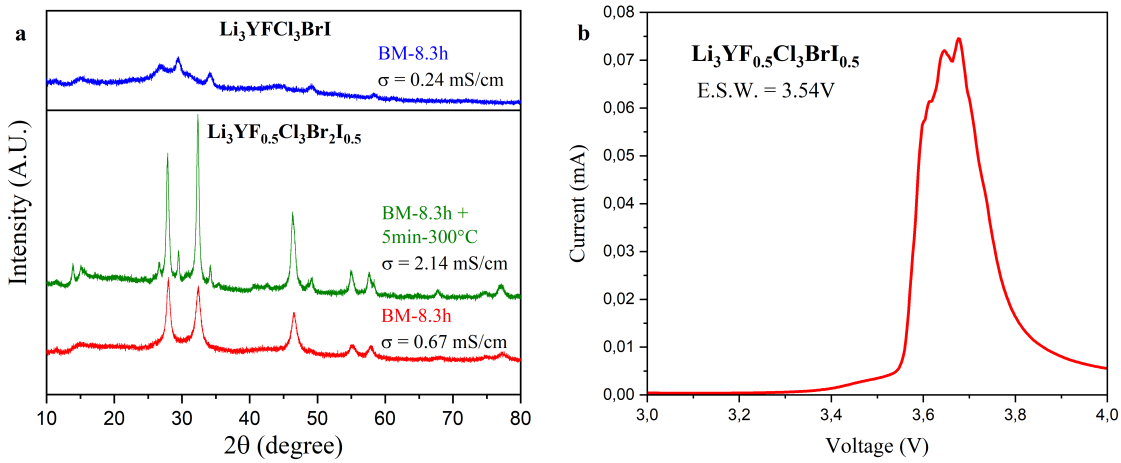

Figure 54: (a) X-ray diffraction patterns of LiY_3FCl_3BrI and $LiY_3F_{0.5}Cl_3Br_2I_{0.5}$, (b) Linear sweep voltammetry measurement of $LiY_3F_{0.5}Cl_3Br_2I_{0.5}$.

4.2.7 Conclusion mixed halide electrolytes

Mixed halide electrolytes offer the potential for tunable ionic conductivities and electrochemical stability window properties due to the distinct characteristics of different halides as displayed in the paper by van der Maas et al [65]. Additonally, yttrium is the second cheapest metal element that is employed in all halide electrolytes (YCl_3 with 330 USD/kg) and is more abundant than most other metals employed with 33 mg/kg in the earth's crust. Therefore, $Li_3YCl_3Br_{3-x}I_x$ with x=0, 0.2, 0.4, 0.6, 0.8, and 1 has been investigated.

In this project, the ball milling (BM) time for all samples was kept constant at 8.3 hours. Initially, the optimal annealing temperature for $Li_3YCl_3Br_2I$ was explored, revealing that annealing at 300°C for 5 hours resulted in a conductivity of 3.25 mS/cm. Subsequently, the optimal annealing time was determined to be 5 minutes at 300°C, resulting in a higher conductivity of 3.55 mS/cm. These optimized conditions were then applied to the other compositions. The short annealing time may contribute to the removal of defects or disordered regions within the material, enhancing conductivity. X-ray diffraction (XRD) measurements indicated a clear crystalline C2/m phase with narrowed peaks for the annealed sample, suggesting improved crystallinity and reduced defects.

The increase in ionic conductivity with increasing iodide content is substantial after annealing for 5 minutes at 300°C. $Li_3YCl_3Br_3$, $Li_3YCl_3Br_{2.8}I_{0.2}$, $Li_3YCl_3Br_{2.6}I_{0.4}$, $Li_3YCl_{2.4}Br_{0.6}$, $Li_3YCl_3Br_{2.2}I_{0.8}$, and $Li_3YCl_3Br_2I$ exhibited values of 1.94, 1.63, 2.03, 2.43, 2.85, and 3.55 mS/cm, respectively. In contrast, the change in oxidation potential was less pronounced, decreasing from 3.59 V for x=0 to 3.474 V for x=1. This suggests that the impact of iodide on conductivity is more significant than its effect on the electrochemical stability window. X-ray photoelectron spectroscopy (XPS) measurements confirmed the presence of iodide (0) after linear sweep voltammetry (LSV) measurements, indicating that iodide is the first halide to oxidize. Additionally, cyclic voltammetry (CV) measurements suggested that iodide oxidation creates a stable product layer, protecting the electrolyte from further oxidation. This could potentially imply that cycling can be conducted above these potentials.

Finally, with increasing iodide content, lattice expansion has been observed due to the larger ionic radius of iodide (r_{I^-} = 202 pm) being inserted into the crystal compared to bromide (r_{Br^-} = 182 pm). This

expansion increases the bottleneck size, allowing Li-ions to pass through more easily, possibly impacting activation energy and, consequently, ionic conductivity.

5

Final conclusion and recommendations

Final conclusion

- **Zr-based oxyhalide ($\mathbf{Li_{2x}ZrCl_4O_x}$)**
- For $Li_{2x}ZrCl_4O_x$ compositions, the structure can be tuned through the duration of mechanical ball milling. Optimizing the ball milling time is crucial in achieving the most amorphous phase, thereby optimizing conductivity.
- The oxygen (O) content present has a dual impact: it influences the degree of amorphization (with amorphous structure enhancing conductivity) and the concentration of Li-ions (where higher Li-ion concentration typically results in a greater number of active Li-ions). This results in a trade-off. Lower O contents result in complete amorphization, but this is accompanied by a decrease in Li-ion concentration, which, leads to lower conductivity compared to samples with higher O doping. Higher O contents lead to increased crystallinity (which is less conductive) but is compensated by an increase in Li-ion concentration. Additionally, higher O content results in a reduction in the time required for ball milling to achieve the most amorphous structure. This trade-off leads to the highest conductivity with Li_2ZrCl_4O at room temperature of 1.60 mS/cm after 17.2 effective hours of ball milling with a coexisting structure of P3m1 and amorphous phases.
- The C2/m structure demonstrates poor conductivity, while the P3m1 structure exhibits good conductivity. The amorphous phase, however, stands out as the most conductive. This is the opposite trend with typical halide electrolytes, where the C2/m phase usually exhibits the highest conductivity.
- The higher conductivity in the amorphous phase is likely due to increased disorder, enabling more free movement of lithium ions.
- With yttrium doping, less ball milling time is required to reach the desired structure and an almost fully amorphous phase can be formed.
- The battery cycling performances are promising, with Li_2ZrCl_4O as an electrolyte exhibiting an initial capacity of 125.6 mAh/g at 0.5C and retaining 67.47% capacity after 1000 cycles.

- **Mixed halides ($\mathbf{Li_3YCl_3Br_{3-x}I_x}$)**
- $Li_3YCl_3Br_{3-x}I_x$ electrolyte have shown to posses tunable conductivity and oxidation potential, making them promising candidates for solid-state battery applications.
- Iodide's larger ionic radius, compared to bromide, increases the lattice parameter and positively influences conductivity, as seen in $Li_3YCl_3Br_2I$ with conductivity of 3.55 mS/cm.
- Iodide negatively impacts the oxidation potential, with $Li_3YCl_3Br_3$ at 3.59 V vs Li/Li^+ compared to 3.474 V for $Li_3YCl_3Br_2I$.

- Iodide is the first halide element that oxidizes upon cycling.
- $Li_3YCl_3Br_2I$ forms a stable product layer upon cycling, potentially allowing the battery to be cycled beyond its oxidation potential.

Recommendations

- **Zr-based oxyhalide ($\mathbf{Li_{2x}ZrCl_4O_x}$)**
- Improve Zr-based oxyhalide properties by exploring iron (Fe^{3+}) doping, higher yttrium (Y^{3+}) doping concentrations with prolonged ball milling, and tantalum (Ta^{5+}) doping to enhance amorphization and conductivity.
- Conduct analysis using transmission electron microscopy (TEM) to better understand morphology, grain boundaries and microstructures and nuclear magnetic resonance (NMR) to better comprehend local atomic structure of amorphous materials.
- Investigate the electrolyte's compressibility at various ball milling durations.
- Perform XPS analysis on $Li_{2x}ZrCl_4O_x$ samples before and after LSV to confirm the oxygen oxidation.
- Examine the battery's performance under various cycling rates to gain insights into its behavior.
- **Mixed halides ($\mathbf{Li_3YCl_3Br_{3-x}I_x}$)**
- Conduct density functional theory (DFT) to gain insight into the electronic structure, energetics, and atomic interactions of the material.
- Utilize NMR to better comprehend the local atomic structure of annealed samples.
- Improve conductivity through optimizing the ball milling duration.
- Assemble a battery utilizing $Li_3YCl_3Br_2I$ or $Li_3YF_{0.5}Cl_3Br_2I_{0.5}$ as the electrolyte and a sulfur or NMC coated cathode to investigate the cycling limits and performance characteristics.

6

Appendix

6.1 Appendix A - Background

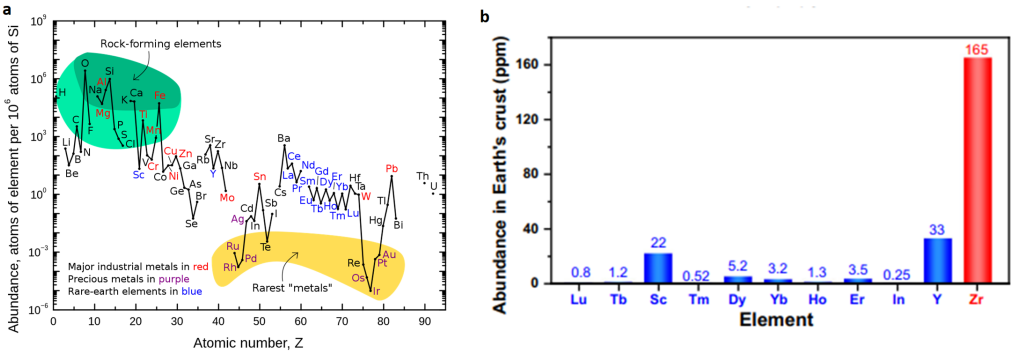

Figure A.1: (a) Abundance of metals in the earth's crust [80] and (b) abundance of elements in earth's crust relevant for chloride based electrolytes [26].

SE	structure	ionic conductivity (mS cm^{-1})	specific density (g cm^{-3})	concentration of Li or Na (mol L^{-1})
Li_3YCl_6 Halides	trigonal, $P\bar{3}m1$	0.51	2.43	22.61
Li_3InCl_6	monoclinic, $C2/m$	1.54	2.71	23.34
Li_3ScCl_6	monoclinic, $C2/m$	3.02	2.2	23.70
$Li_2Sc_{2/3}Cl_4$	cubic, $Fd\bar{3}m$	1.5	2.19	23.59
HT-Li_2ZrCl_6	monoclinic, $C2/m$	0.005	2.53	15.92
BM-Li_2ZrCl_6	trigonal, $P\bar{3}m1$	0.51	2.57	16.17
Na_2ZrCl_6	trigonal, $P\bar{3}m1$	0.018	2.43	13.89
$Na_{2+x}Zr_{1-x}Er_xCl_6$	monoclinic, $P2_1/n$	0.05	2.43–2.97	13.89–19.85
Li_3YbCl_6	trigonal, $P\bar{3}m1$	0.1	3.14	23.17
	orthorhombic, $Pnma$	0.1	3.12	23.02
Li_3YBr_6	monoclinic, $C2/m$	1.7	3.63	18.48
$Li_3In[Cl_5F]_6$	monoclinic, $C2/m$	0.51	2.55	23.32
$Li_2Sc_{2/3-x}In_xCl_4$	cubic, $Fd\bar{3}m$	2	2.2	23.59
$Li_{2+x}Zr_{1-x}Fe_xCl_6$	trigonal, $P\bar{3}m1$	0.98	–	–
$Li_{2+x}Zr_{1-x}In_xCl_6$	monoclinic, $C2/m$	0.005–2	2.53–2.71	15.92–23.34
$Li_{3-x}Yb_{1-x}Zr_xCl_6$	orthorhombic, $Pnma$	1.1	–	–
xLiCl-GaF_3	–	3.7	–	–
$LiAlF_4$	amorphous	0.001	–	–
$Li_{5.5}PS_{4.5}Cl_{1.5}$ Sulfides	cubic, $F\bar{4}3m$	9.4	1.88	38.78
$Li_{10}GeP_2S_{12}$	tetragonal, $P42/nmc$	10	2.08	35.33
$Li_7La_3Zr_2O_{12}$ Oxides	cubic, $Ia\bar{3}d$	0.1–0.4	5.15	42.93
$La_{0.57}Li_{0.29}TiO_3$	tetragonal, $P4/mmm$	0.02	5.14	10.22
$LiTi_2(PO_4)_3$	trigonal, $R\bar{3}c$	0.1	2.93	9.97

Figure A.2: Properties of solid halide electrolytes compared with sulfide and oxide electrolytes [27].

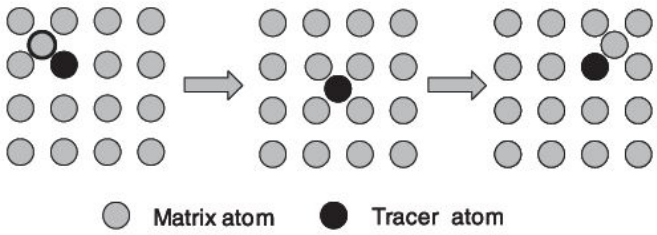

Figure A.3: Interstitialcy mechanism of diffusion [33].

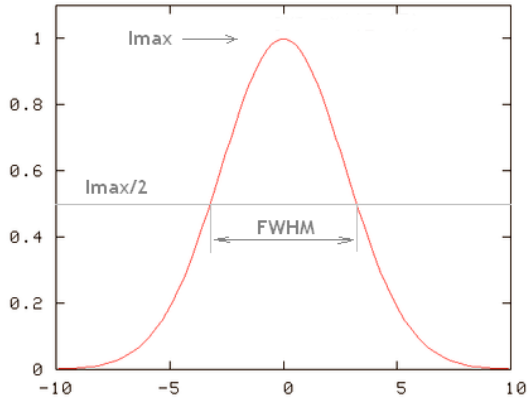

Figure A.4: Illustration of the full width at half-maximum of a diffraction peak (FWHM).

6.2 Appendix B - Oxyhalides electrolyte

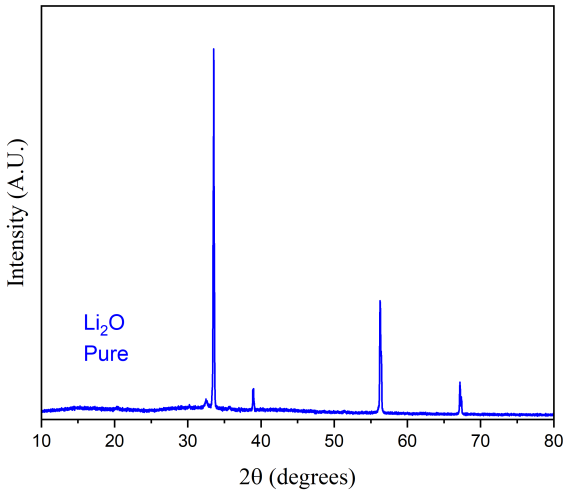

Figure B.1: X-ray diffraction of pure Li_2O.

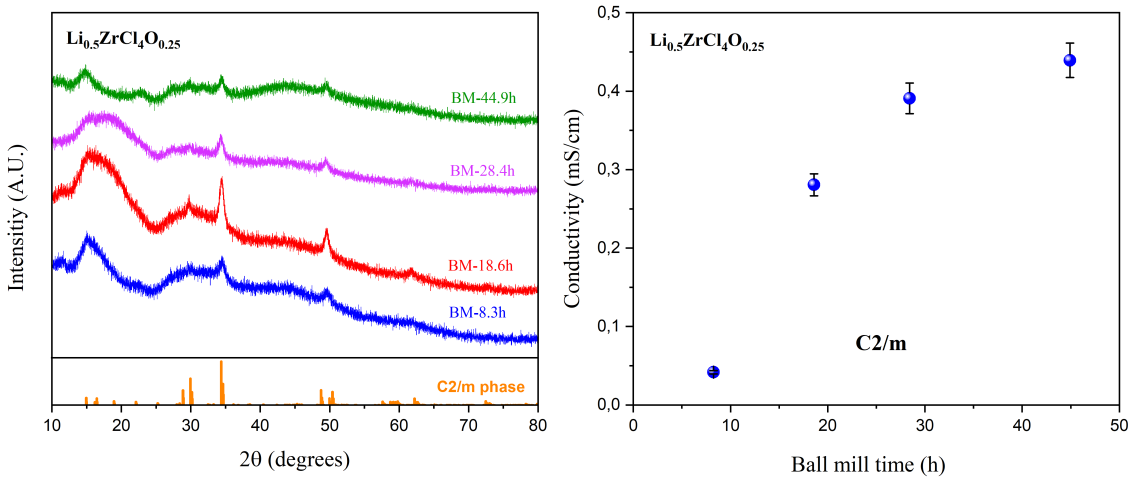

Figure B.2: (left) X-ray diffraction measurements and (right) conductivity measurements of $Li_{0.5}ZrCl_4O_{0.25}$ ball milling for different durations.

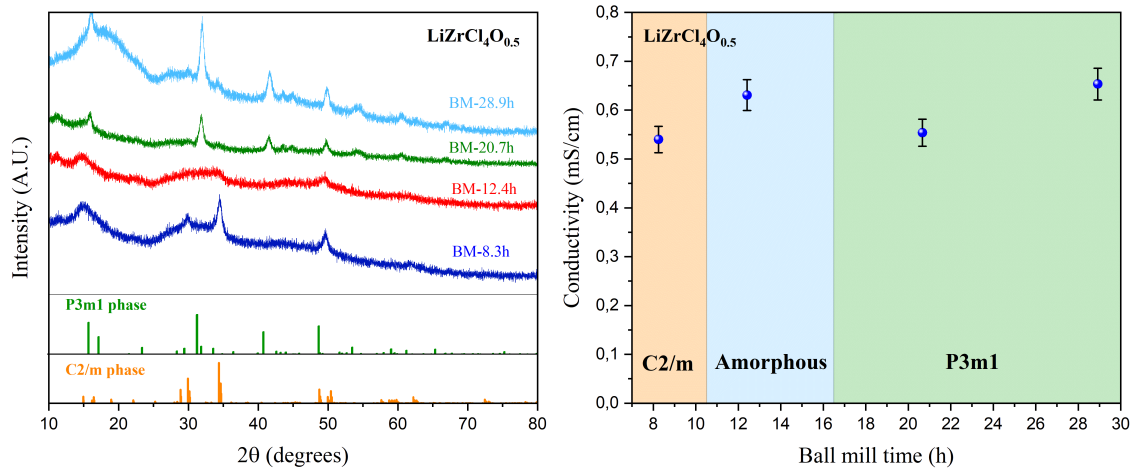

Figure B.3: (left) X-ray diffraction measurements and (right) conductivity measurements of $LiZrCl_4O_{0.5}$ ball milling for different durations.

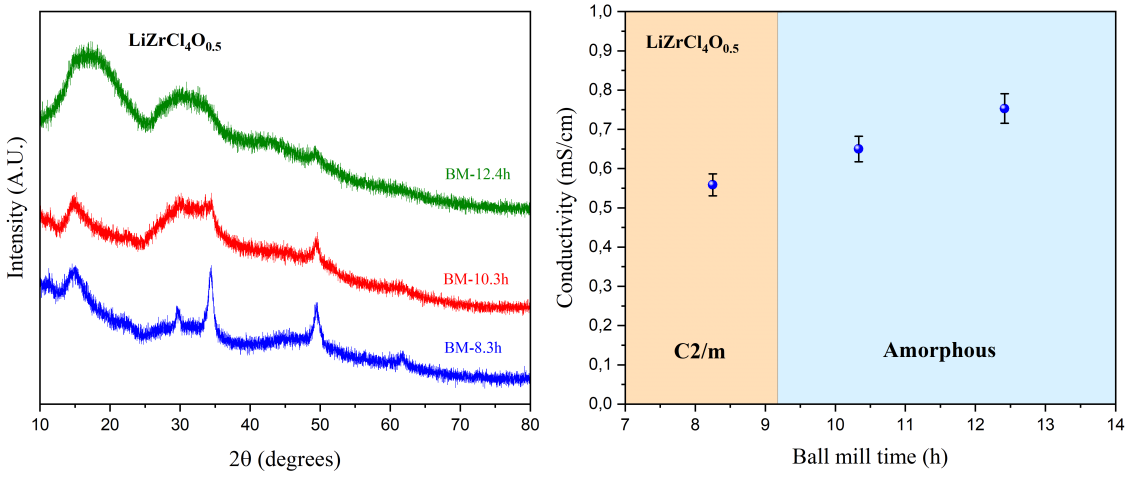

Figure B.4: (left) X-ray diffraction measurements and (right) conductivity measurements of $LiZrCl_4O_{0.5}$ ball milling for different durations.

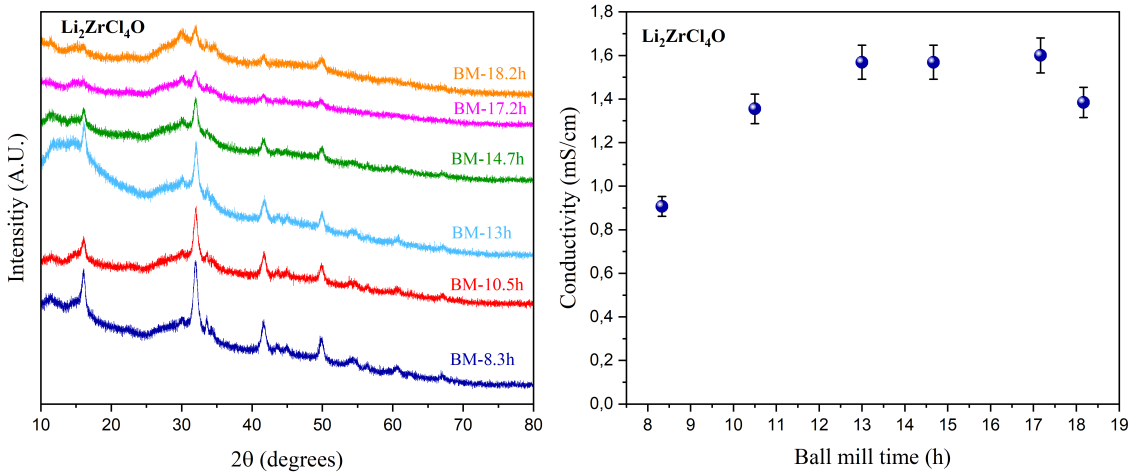

Figure B.5: (left) X-ray diffraction measurements and (right) conductivity measurements of Li_2ZrCl_4O ball milling for different durations.

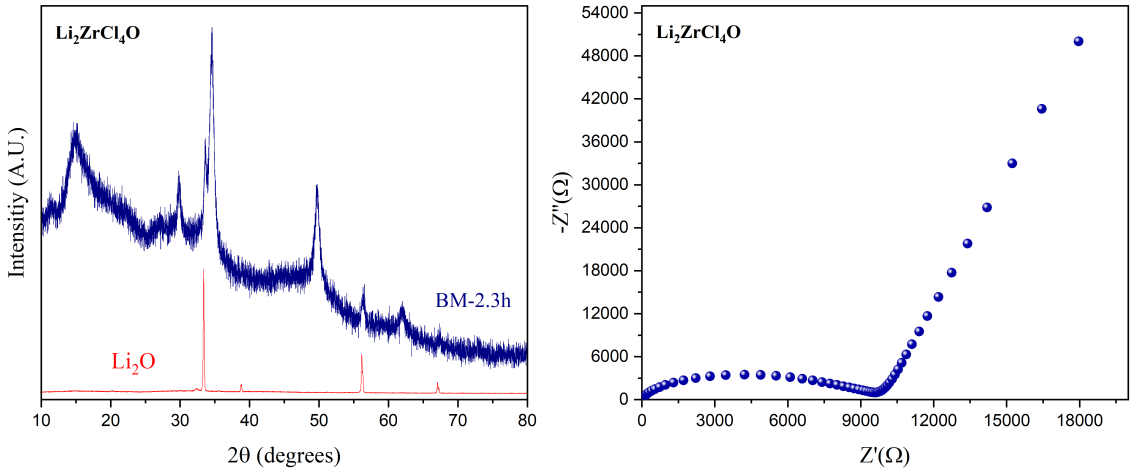

Figure B.6: (left) X-ray diffraction measurement and (right) EIS measurement of ball milled Li_2ZrCl_4O for 2.3 hours.

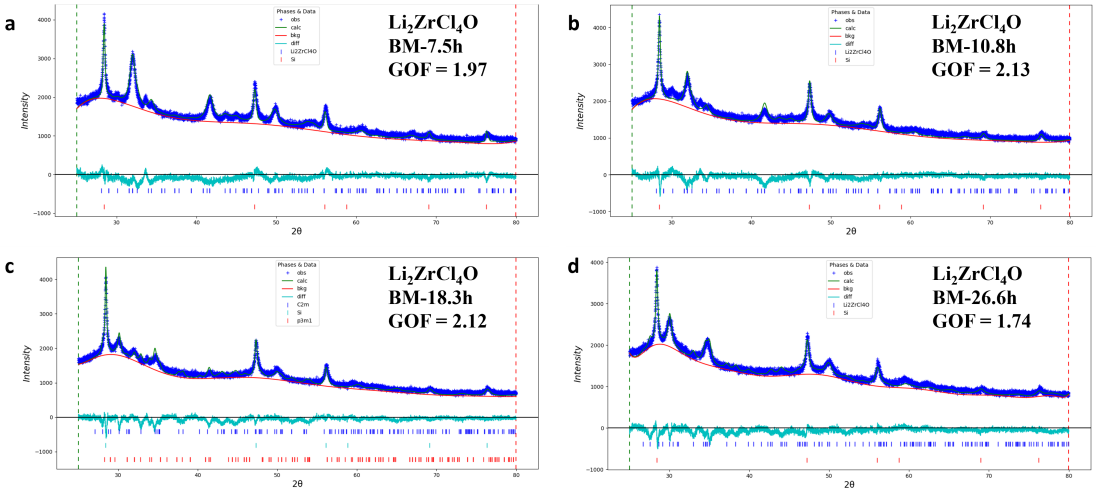

Figure B.7: Refinement results from GSAS II software of Si-Li_2ZrCl_4O (2-8) with (a) 7.5h of BM, (b) 10.8h of BM, (c) 18.3h of BM and (d) 26.6h of BM.

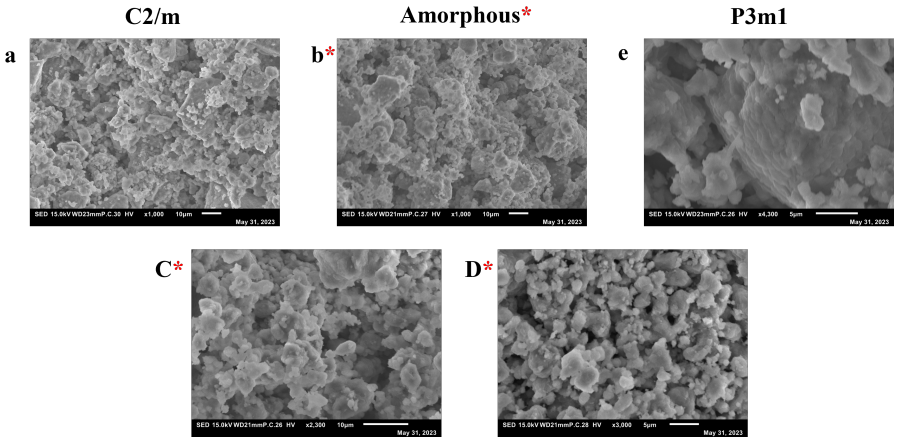

Figure B.8: Additional SEM results for synthesized Li_2ZrCl_4O at different structural phases.

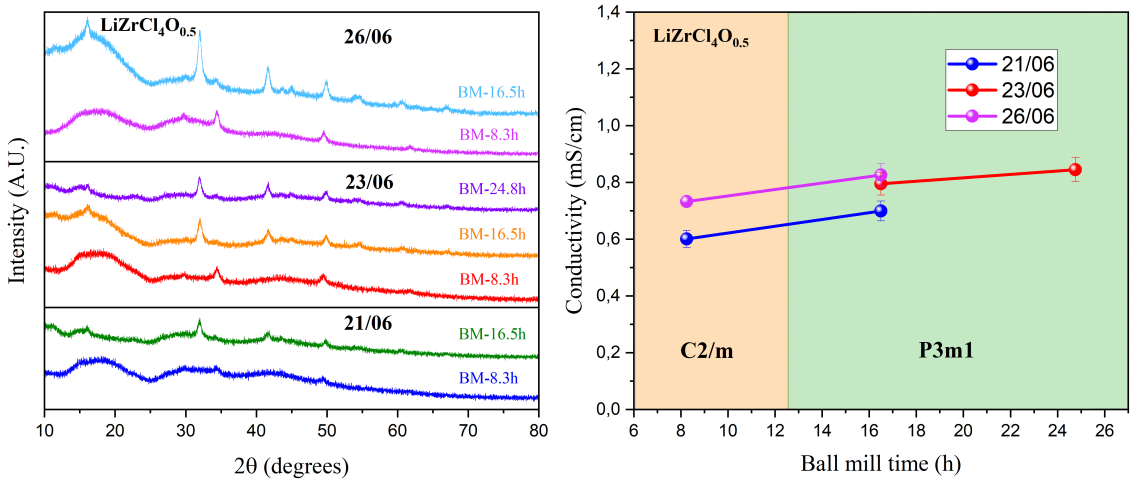

Figure B.9: (left) X-ray diffraction measurements of X-ray diffraction results of $LiZrCl_4O_{0.5}$ with different ball milling durations and batches, and (right) the resulting conductivity measurements of the different $LiZrCl_4O_{0.5}$ ball milled batches.

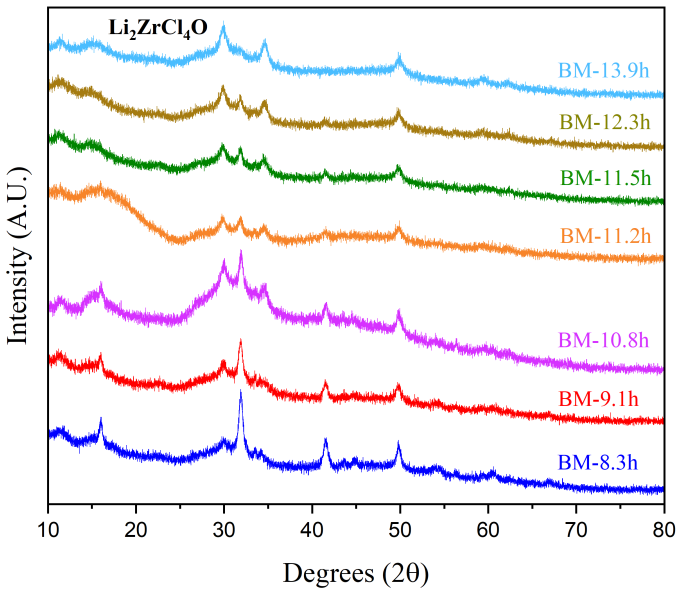

Figure B.10: X-ray diffraction measurements of ball milled Li_2ZrCl_4O for different durations.

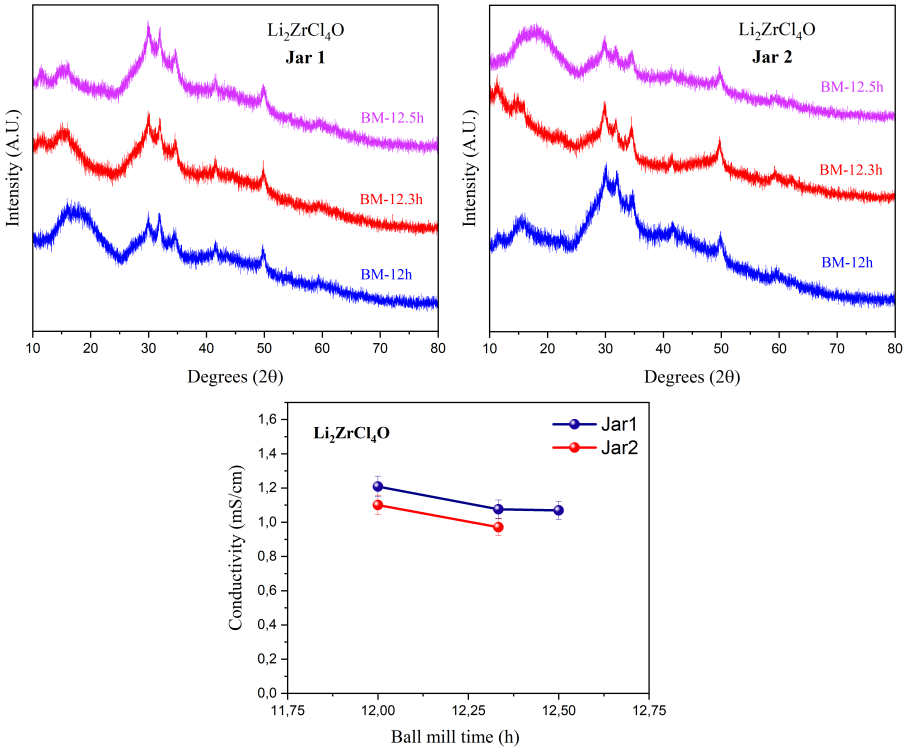

Figure B.11: (top left) X-ray diffraction (XRD) results of Li_2ZrCl_4O at different ball milling durations with Jar 1, (top right) XRD results of Li_2ZrCl_4O at different ball milling durations with Jar 2, and (bottom) resulting conductvities of Jar 1 and Jar 2.

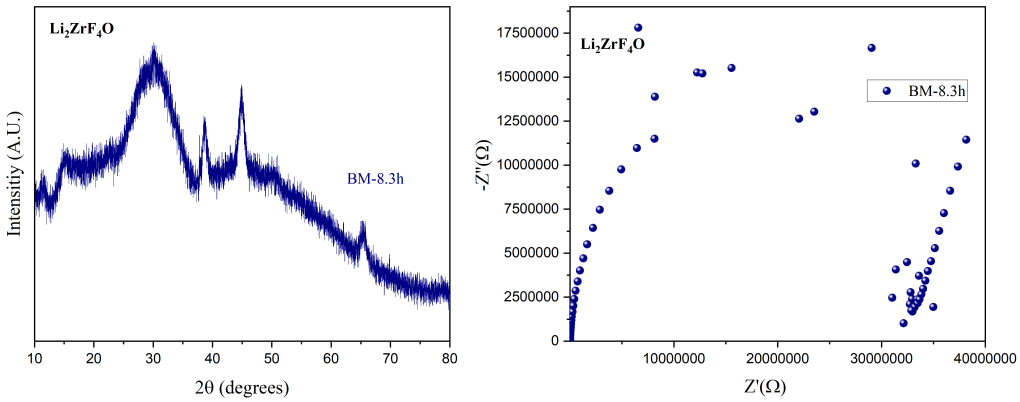

Figure B.12: (left) X-ray diffraction measurements and (right) EIS measurements of ball milled Li_2ZrF_4O for 8.3 hours.

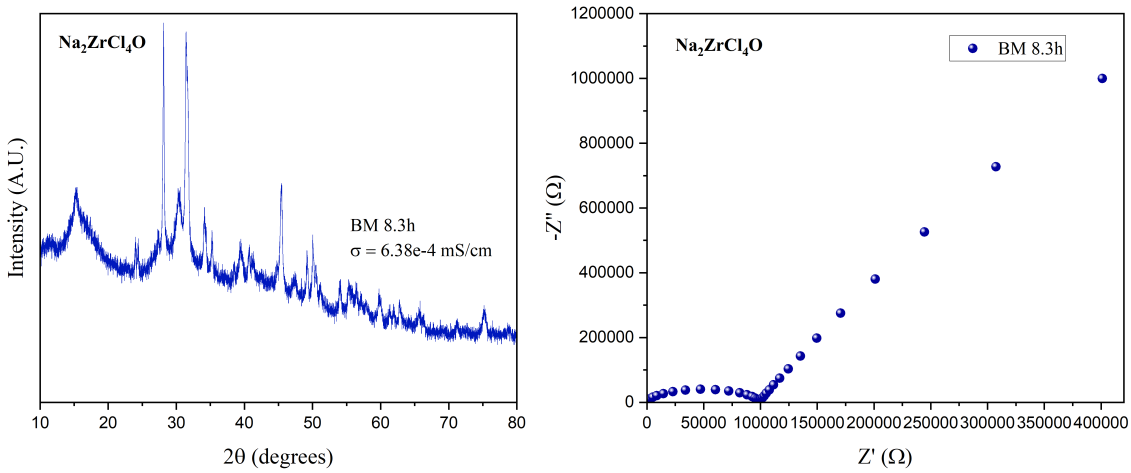

Figure B.13: (left) X-ray diffraction measurements and (right) EIS measurement of ball milled Na_2ZrCl_4O for different 8.3 hours.

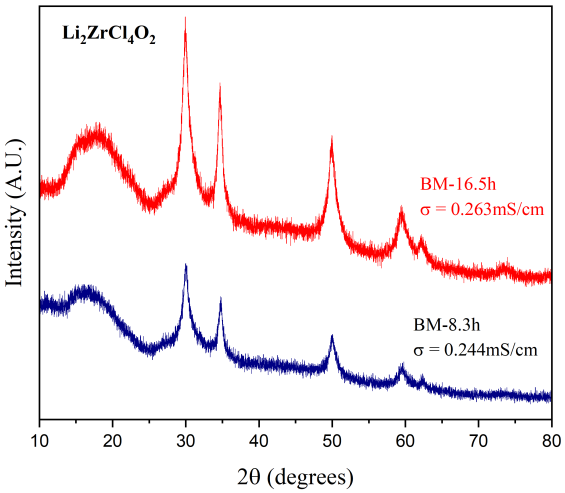

Figure B.14: X-ray diffraction measurements of ball milled $Li_2ZrCl_4O_2$ for 8.3h and 16.5h with its respective conductivity.

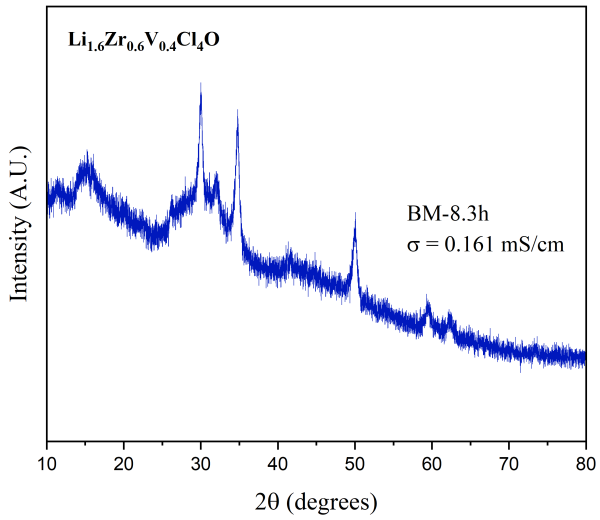

Figure B.15: X-ray diffraction measurements of ball milled $Li_{1.6}Zr_{0.6}V_{0.4}Cl_4O$ for 8.3h with its conductivity.

6.3 Appendix C - Mixed halides electrolyte

Table 7: Lattice parameters and volume of 8.3h ball milled and annealed at 300 °C for 5 minutes of $Li_3YCl_3Br_{3-x}I_x$ with x=0, 0.2, 0.4, 0.6, 0.8 and 1. These are obtained with GSAS II software.

$Li_3YCl_3Br_{3-x}I_x$	a (Å)	b (Å)	c (Å)	Volume (Å^3)
x = 0	6.731	11.688	6.694	496.687
x = 0.2	6.752	11.699	6.746	502.253
x = 0.4	6.773	11.760	6.763	508.237
x = 0.6	6.775	11.741	6.732	504.376
x = 0.8	6.808	11.779	6.787	514.074
x = 1	6.582	11.815	6.836	521.416

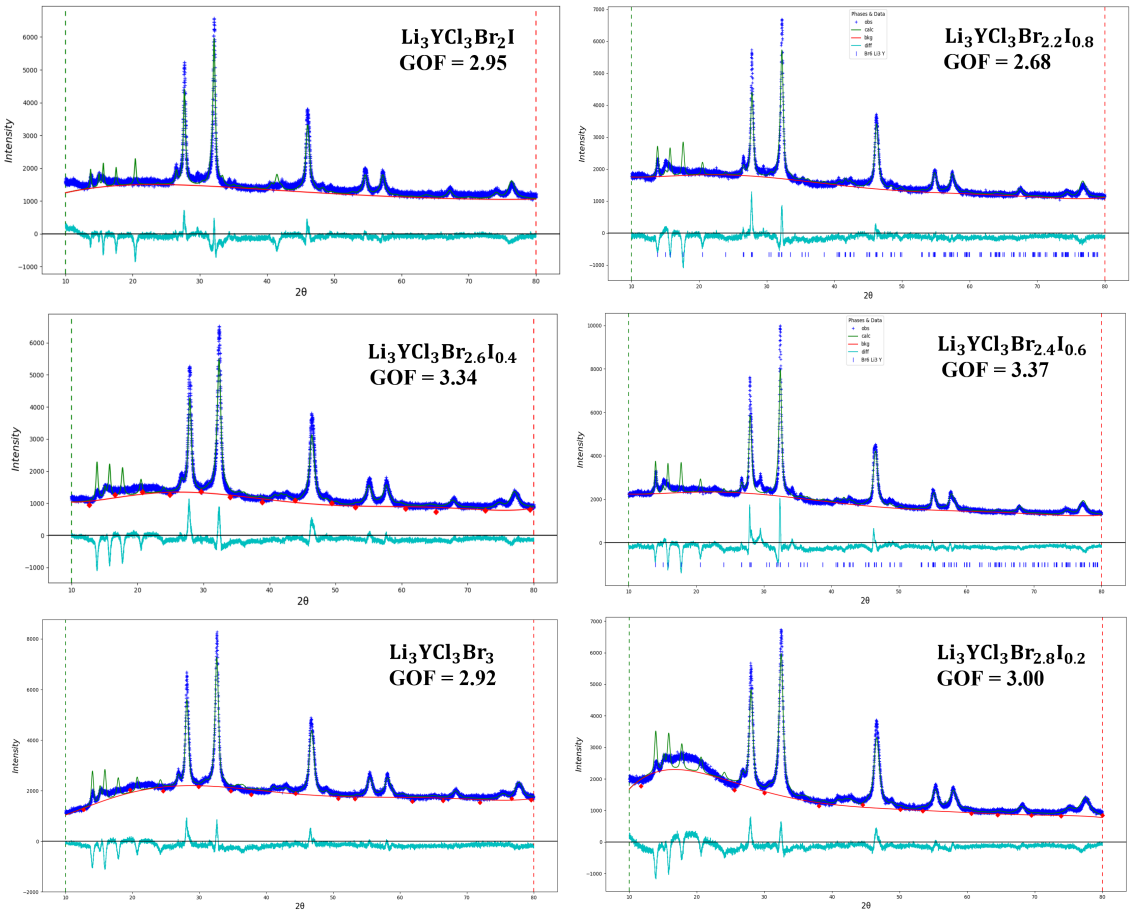

Figure C.1: Refinement results from GSAS II software of $Li_3YCl_3Br_{3-x}I_x$ with x=0, 0.2, 0.4, 0.6, 0.8 and 1.

References

[1] Lívia Salles Martins et al. "Electric car battery: An overview on global demand, recycling and future approaches towards sustainability". In: *Journal of Environmental Management* 295 (Oct. 2021), p. 113091. ISSN: 0301-4797. DOI: 10.1016/J.JENVMAN.2021.113091.

[2] Richard Van Noorden. "A better battery". In: *Nature* 507 (Mar. 2014), pp. 26–28. URL: https://www.nature.com/news/polopoly_fs/1.14815!/menu/main/topColumns/topLeftColumn/pdf/507026a.pdf.

[3] Yu Miao et al. *Current li-ion battery technologies in electric vehicles and opportunities for advancements*. Mar. 2019. DOI: 10.3390/en12061074.

[4] O'Dea S. *Global battery market size by technology | Statista*. Jan. 2023. URL: https://www.statista.com/statistics/1339880/global-battery-market-size-by-technology/.

[5] Timur Gül, Araceli Fernandez Pales, and Leonardo Paoli. *Batteries and hydrogen technology: keys for a clean energy future – Analysis - IEA*. Tech. rep. IEA, May 2020. URL: https://www.iea.org/articles/batteries-and-hydrogen-technology-keys-for-a-clean-energy-future.

[6] H. Qiao and Q. Wei. "Functional nanofibers in lithium-ion batteries". In: *Functional Nanofibers and their Applications* (Jan. 2012), pp. 197–208. DOI: 10.1533/9780857095640.2.197.

[7] Orendorff Christopher J. "The Role of Separators in Lithium-Ion Cell Safety". In: *The Electrochemical Society Interface* (2012). URL: https://www.electrochem.org/dl/interface/sum/sum12/sum12_p061_065.pdf.

[8] Sushyanth Sridhar and Surender Reddy Salkuti. *Development and Future Scope of Renewable Energy and Energy Storage Systems*. June 2022. DOI: 10.3390/smartcities5020035.

[9] Teddy Mageto et al. "Developing practical solid-state rechargeable Li-ion batteries: Concepts, challenges, and improvement strategies". In: *Journal of Energy Storage* 55 (Nov. 2022), p. 105688. ISSN: 2352-152X. DOI: 10.1016/J.EST.2022.105688.

[10] Philip Minnmann et al. "Editors' Choice-Quantifying the Impact of Charge Transport Bottlenecks in Composite Cathodes of All-Solid-State Batteries". In: (2021). DOI: 10.1149/1945-7111/abf8d7.

[11] Chuang Yu et al. "Accessing the bottleneck in all-solid state batteries, lithium-ion transport over the solid-electrolyte-electrode interface". In: *Nature* (2017). DOI: 10.1038/s41467-017-01187-y. URL: www.nature.com/naturecommunications.

[12] Feng Zheng et al. "Review on solid electrolytes for all-solid-state lithium-ion batteries". In: *Journal of Power Sources* 389 (June 2018), pp. 198–213. ISSN: 0378-7753. DOI: 10.1016/J.JPOWSOUR.2018.04.022.

[13] Tetsuya Asano et al. "Solid Halide Electrolytes with High Lithium-Ion Conductivity for Application in 4 V Class Bulk-Type All-Solid-State Batteries". In: *Advanced Materials* 30.44 (Nov. 2018). ISSN: 15214095. DOI: 10.1002/ADMA.201803075.

[14] Windhu Griyasti Suci et al. "Review of various sulfide electrolyte types for solid-state lithium-ion batteries". In: *Open Engineering* 12.1 (Jan. 2022), pp. 409–423. ISSN: 23915439. DOI: 10.1515/eng-2022-0043.

[15] Kazuya Terabe, Takashi Tsuchiya, and Tohru Tsuruoka. *Solid state ionics for the development of artificial intelligence components*. Oct. 2022. DOI: 10.35848/1347-4065/ac64e5.

[16] Lv Hu et al. "A cost-effective, ionically conductive and compressible oxychloride solid-state electrolyte for stable all-solid-state lithium-based batteries". In: *Nature Communications* 14.1 (June 2023). ISSN: 20411723. DOI: 10.1038/s41467-023-39522-1.

[17] Qi Li et al. *Progress in electrolytes for rechargeable Li-based batteries and beyond*. Apr. 2016. DOI: 10.1016/j.gee.2016.04.006.

[18] Rezan Demir-Cakan, M. Rosa Palacin, and Laurence Croguennec. *Rechargeable aqueous electrolyte batteries: From univalent to multivalent cation chemistry*. 2019. DOI: 10.1039/c9ta04735b.

[19] Duygu Karabelli, Kai Peter Birke, and Max Weeber. *A performance and cost overview of selected solid-state electrolytes: Race between polymer electrolytes and inorganic sulfide electrolytes*. Mar. 2021. DOI: 10.3390/batteries7010018.

[20] Trang Thi Vu et al. "Hybrid electrolytes for solid-state lithium batteries: Challenges, progress, and prospects". In: *Energy Storage Materials* (Aug. 2023), p. 102876. ISSN: 24058297. DOI: 10.1016/j.ensm.2023.102876.

[21] M. Hagen et al. "Studies on preventing Li dendrite formation in Li–S batteries by using pre-lithiated Si microwire anodes". In: *Journal of Power Sources* 248 (Feb. 2014), pp. 1058–1066. ISSN: 0378-7753. DOI: 10.1016/J.JPOWSOUR.2013.09.144.

[22] Laidong Zhou et al. "High areal capacity, long cycle life 4 V ceramic all-solid-state Li-ion batteries enabled by chloride solid electrolytes". In: *Nature* (2022). DOI: 10.1038/s41560-021-00952-0. URL: https://doi.org/10.1038/s41560-021-00952-0.

[23] Elena Vergori, Francesco Mocera, and Aurelio Somà. "Battery Modelling and Simulation Using a Programmable Testing Equipment". In: *Computers 2018, Vol. 7, Page 20* 7.2 (Mar. 2018), p. 20. ISSN: 2073-431X. DOI: 10.3390/COMPUTERS7020020. URL: https://www.mdpi.com/2073-431X/7/2/20/htm%20https://www.mdpi.com/2073-431X/7/2/20.

[24] Changhong Wang et al. *Prospects of halide-based all-solid-state batteries: From material design to practical application*. Tech. rep. 2022, p. 9516. URL: https://www.science.org.

[25] Thomas Schmaltz et al. *Solid-State Battery Roadmap 2035+*. Tech. rep. Faunhofer ISI, 2020. URL: https://www.isi.fraunhofer.de/content/dam/isi/dokumente/cct/2022/SSB_Roadmap.pdf.

[26] Kai Wang et al. "A cost-effective and humidity-tolerant chloride solid electrolyte for lithium batteries". In: *Nature Communications* 12.1 (Dec. 2021). ISSN: 20411723. DOI: 10.1038/s41467-021-24697-2.

[27] Hiram Kwak et al. "Emerging Halide Superionic Conductors for All-Solid-State Batteries: Design, Synthesis, and Practical Applications". In: *ACS Energy Letters* 7.5 (May 2022), pp. 1776–1805. ISSN: 23808195. DOI: 10.1021/ACSENERGYLETT.2C00438/ASSET/IMAGES/LARGE/NZ2C00438{_}0017.JPEG. URL: https://pubs.acs.org/doi/full/10.1021/acsenergylett.2c00438.

[28] John Christopher Bachman et al. *Inorganic Solid-State Electrolytes for Lithium Batteries: Mechanisms and Properties Governing Ion Conduction*. Jan. 2016. DOI: 10.1021/acs.chemrev.5b00563.

[29] Theodosios Famprikis et al. *Fundamentals of inorganic solid-state electrolytes for batteries*. Dec. 2019. DOI: 10.1038/s41563-019-0431-3.

[30] Masatoshi Uno and Koji Tanaka. "Accelerated charge-discharge cycling test and cycle life prediction model for supercapacitors in alternative battery applications". In: *IEEE Transactions on Industrial Electronics* 59.12 (2012), pp. 4704–4712. ISSN: 02780046. DOI: 10.1109/TIE.2011.2182018.

[31] E L Van Der Maas. *Halide solid electrolytes From structure to properties*. 2023. ISBN: 978-9464-693-836. DOI: 10.4233/uuid:a5ad83c4-f85b-4cc3-b775-7959236b37f1. URL: https://doi.org/10.4233/uuid:a5ad83c4-f85b-4cc3-b775-7959236b37f1.

[32] Myounggu Park et al. "A review of conduction phenomena in Li-ion batteries". In: *Journal of Power Sources* 195.24 (Dec. 2010), pp. 7904–7929. ISSN: 0378-7753. DOI: 10.1016/J.JPOWSOUR.2010.06.060.

[33] M. Helmut. *Diffusion in solids*. Ed. by Cardona M. Springer, 2007. ISBN: 978-3-540-71486-6.

[34] Wu Musheng, Xu Bo, and Ouyang Chuying. "Physics of electron and lithium-ion transport in electrode materials for Li-ion batteries". In: *Chinese Physics B* (2016).

[35] Kecheng Zhang et al. "Lithium ion diffusion mechanism in covalent organic framework based solid state electrolyte". In: *Physical Chemistry Chemical Physics* 21.19 (May 2019), pp. 9883–9888. ISSN: 1463-9084. DOI: 10.1039/C9CP02117E. URL: https://pubs.rsc.org/en/content/articlehtml/2019/cp/c9cp02117e%20https://pubs.rsc.org/en/content/articlelanding/2019/cp/c9cp02117e.

[36] Laidong Zhou et al. "A new halospinel superionic conductor for high-voltage all solid state lithium batteries". In: *Energy & Environmental Science* 13.7 (July 2020), pp. 2056–2063. ISSN: 1754-5706. DOI: 10.1039/D0EE01017K. URL: https://pubs.rsc.org/en/content/

articlehtml/2020/ee/d0ee01017k%20https://pubs.rsc.org/en/content/articlelanding/2020/ee/d0ee01017k.

[37] Hiram Kwak et al. "New Cost-Effective Halide Solid Electrolytes for All-Solid-State Batteries: Mechanochemically Prepared Fe3+-Substituted Li2ZrCl6". In: *Advanced Energy Materials* 11.12 (Mar. 2021), p. 2003190. ISSN: 1614-6840. DOI: 10.1002/AENM.202003190. URL: https://onlinelibrary.wiley.com/doi/full/10.1002/aenm.202003190%20https://onlinelibrary.wiley.com/doi/abs/10.1002/aenm.202003190%20https://onlinelibrary.wiley.com/doi/10.1002/aenm.202003190.

[38] Shuo Wang et al. "Lithium Chlorides and Bromides as Promising Solid-State Chemistries for Fast Ion Conductors with Good Electrochemical Stability". In: *Angewandte Chemie International Edition* 58.24 (June 2019), pp. 8039–8043. ISSN: 1521-3773. DOI: 10.1002/ANIE.201901938. URL: https://onlinelibrary.wiley.com/doi/full/10.1002/anie.201901938%20https://onlinelibrary.wiley.com/doi/abs/10.1002/anie.201901938%20https://onlinelibrary.wiley.com/doi/10.1002/anie.201901938.

[39] Yubin Zhang et al. *Fundamental Relationship of Microstructure and Ionic Conductivity of Amorphous LLTO as Solid Electrolyte Material*. Tech. rep. 2019. DOI: 10.1149/2.0161904jes.

[40] Sophia Akhtar et al. "Conduction Mechanism of Charge Carriers in Electrodes and Design Factors for the Improvement of Charge Conduction in Li-ion Batteries". In: *Journal of Electrochemical Science and Technology* 12.1 (Jan. 2021), pp. 1–20. ISSN: 2093-8551. DOI: 10.33961/JECST.2020.01564. URL: http://jecst.org/journal/view.php?number=371.

[41] Fudong Han et al. "High electronic conductivity as the origin of lithium dendrite formation within solid electrolytes". In: *Nature Energy 2019 4:3* 4.3 (Jan. 2019), pp. 187–196. ISSN: 2058-7546. DOI: 10.1038/s41560-018-0312-z. URL: https://www.nature.com/articles/s41560-018-0312-z.

[42] Adrien Méry et al. *A critical review for an accurate electrochemical stability window measurement of solid polymer and composite electrolytes*. July 2021. DOI: 10.3390/ma14143840.

[43] P. J. Gellings and H. J. M. Bouwmeester. *The CRC handbook of solid state electrochemistry*. CRC Press, 1997, p. 630. ISBN: 0849389569.

[44] William D. Callister and David G. Rethwisch. *Materials Science and Engineering*. Vol. 10. Hachette Livre - Département Pratique, 2018. ISBN: 9781119321590.

[45] Josh Halpern. *Crystal structures*. Tech. rep. 2023. URL: https://LibreTexts.org.

[46] Kate J. Jeffery et al. "Neural encoding of large-scale three-dimensional space—properties and constraints". In: *Frontiers in Psychology* 6 (July 2015). ISSN: 1664-1078. DOI: 10.3389/fpsyg.2015.00927.

[47] Adrien Stoliaroff, Camille Latouche, and Stéphane Jobic. "Versatile electrical behavior of 1T-TiS2 elucidated from a theoretical study". In: *Physical Review B* 99.16 (Apr. 2019). ISSN: 24699969. DOI: 10.1103/PhysRevB.99.165122.

[48] Feng Zheng et al. "Exploration of crystal structures and phase transitions in Hf ₃ N ₄". In: *CrystEngComm* 19.19 (2017), pp. 2608–2613. ISSN: 1466-8033. DOI: 10.1039/C7CE00524E.

[49] Hosni Idrissi, Philippe Carrez, and Patrick Cordier. *On amorphization as a deformation mechanism under high stresses*. Feb. 2022. DOI: 10.1016/j.cossms.2021.100976.

[50] Shumin Zhang et al. "A family of oxychloride amorphous solid electrolytes for long-cycling all-solid-state lithium batteries". In: *Nature Communications* 14.1 (Dec. 2023). ISSN: 20411723. DOI: 10.1038/s41467-023-39197-8.

[51] Jean Marie Tarascon et al. "On the benefits of ball milling within the field of rechargeable Li-based batteries". In: *Comptes Rendus Chimie* 8.1 (Jan. 2005), pp. 17–26. ISSN: 16310748. DOI: 10.1016/j.crci.2004.12.006.

[52] Roman Schlem et al. *Energy Storage Materials for Solid-State Batteries: Design by Mechanochemistry*. Aug. 2021. DOI: 10.1002/aenm.202101022.

[53] Pardeep Sharma. "Ball milling for the formation of nanocrystalline intermetallic compounds from Ni-Ti elemental powders". In: *Journal of the Mechanical Behavior of Materials* 27.5-6 (Dec. 2018). ISSN: 21910243. DOI: 10.1515/jmbm-2018-2005.

[54] Peter Baláž et al. “Hallmarks of mechanochemistry: From nanoparticles to technology”. In: *Chemical Society Reviews* 42.18 (Aug. 2013), pp. 7571–7637. ISSN: 14604744. DOI: 10.1039/c3cs35468g.
[55] C Suryanarayana. *Progress in Materials Science*. Vol. Volume 46. 2001.
[56] Yukihiro Okuno, Jun Haruyama, and Yoshitaka Tateyama. “Comparative study on sulfide and oxide electrolyte interfaces with cathodes in all-solid-state battery via first-principles calculations”. In: *ACS Applied Energy Materials* 3.11 (Nov. 2020), pp. 11061–11072. ISSN: 25740962. DOI: 10.1021/acsaem.0c02033.
[57] Ran Wei et al. “Challenges, fabrications and horizons of oxide solid electrolytes for solid-state lithium batteries”. In: *Nano Select* 2.12 (Dec. 2021), pp. 2256–2274. ISSN: 2688-4011. DOI: 10.1002/nano.202100110.
[58] Yoshitaka Ishiguro et al. “TaCl5-glassified Ultrafast Lithium Ion-conductive Halide Electrolytes for High-performance All-solid-state Lithium Batteries”. In: *Chemistry Letters* 52.4 (2023), pp. 237–241. ISSN: 13480715. DOI: 10.1246/cl.220540.
[59] ATSDR (Agency for Toxic Substances and Disease Registry). *Hydrogen Sulfide Hydrogen Sulfide Patient Information Sheet*. Tech. rep.
[60] Boran Tao et al. *Halide solid-state electrolytes for all-solid-state batteries: structural design, synthesis, environmental stability, interface optimization and challenges*. Aug. 2023. DOI: 10.1039/d3sc02093b.
[61] K Kim et al. *Materials Design Strategy for Halide Solid Electrolytes for All-Solid-State High-Voltage Li-Ion Batteries Chemistry of Materials*. Tech. rep. 2021.
[62] Zhantao Liu et al. “High Ionic Conductivity Achieved in Li3Y(Br3Cl3) Mixed Halide Solid Electrolyte via Promoted Diffusion Pathways and Enhanced Grain Boundary”. In: *ACS Energy Letters* 6.1 (Jan. 2021), pp. 298–304. ISSN: 23808195. DOI: 10.1021/acsenergylett.0c01690.
[63] Shuting Luo et al. “Growth of lithium-indium dendrites in all-solid-state lithium-based batteries with sulfide electrolytes”. In: *Nature Communications* 12.1 (Dec. 2021). ISSN: 20411723. DOI: 10.1038/s41467-021-27311-7.
[64] Xuming Luo et al. “Ionic Conductivity Enhancement of Li2ZrCl6Halide Electrolytes via Mechanochemical Synthesis for All-Solid-State Lithium-Metal Batteries”. In: *ACS Applied Materials and Interfaces* (2022). ISSN: 19448252. DOI: 10.1021/acsami.2c14903.
[65] Eveline van der Maas et al. “Investigation of Structure, Ionic Conductivity, and Electrochemical Stability of Halogen Substitution in Solid-State Ion Conductor Li3YBrxCl6-x”. In: *Journal of Physical Chemistry C* 127.1 (Jan. 2023), pp. 125–132. ISSN: 19327455. DOI: 10.1021/acs.jpcc.2c07910.
[66] Abraham J. Padilla. *Mineral Commodity Spotlight Production*. Tech. rep. 2019. URL: https://www.usgs.gov/centers/nmic.
[67] Birkholz M. *Thin Film Analysis by X-Ray Scattering*. 2006. ISBN: 3-527-31052-5. URL: https://application.wiley-vch.de/books/sample/3527310525_c01.pdf.
[68] Mehmet Gumustas et al. “Effect of Polymer-Based Nanoparticles on the Assay of Antimicrobial Drug Delivery Systems”. In: *Multifunctional Systems for Combined Delivery, Biosensing and Diagnostics* (Jan. 2017), pp. 67–108. DOI: 10.1016/B978-0-323-52725-5.00005-8.
[69] *Bragg law | Definition, Equation, Diagram, & Facts | Britannica*. URL: https://www.britannica.com/science/Bragg-law.
[70] Tawfik Abdo Saleh. “Structural characterization of hybrid materials”. In: *Polymer Hybrid Materials and Nanocomposites*. Elsevier, 2021, pp. 213–240. DOI: 10.1016/b978-0-12-813294-4.00005-4.
[71] Pooja Vadhva et al. *Electrochemical Impedance Spectroscopy for All-Solid-State Batteries: Theory, Methods and Future Outlook*. June 2021. DOI: 10.1002/celc.202100108.
[72] Alexandros Ch Lazanas and Mamas I. Prodromidis. “Electrochemical Impedance SpectroscopyA Tutorial”. In: *ACS Measurement Science Au* (June 2022). ISSN: 2694250X. DOI: 10.1021/acsmeasuresciau.2c00070.
[73] Weilie Zhou and Zhong Lin Wang. *Scanning Microscopy for Nanotechnology Techniques and Applications*. 2006. ISBN: 978-0-387-33325-0.

[74] Fred A. Stevie and Carrie L. Donley. "Introduction to x-ray photoelectron spectroscopy". In: *Journal of Vacuum Science & Technology A* 38.6 (Dec. 2020), p. 063204. ISSN: 0734-2101. DOI: 10.1116/6.0000412.

[75] Taewhan Kim et al. "Applications of Voltammetry in Lithium Ion Battery Research". In: *Journal of Electrochemical Science and Technology* 11.1 (Jan. 2020), pp. 14–25. ISSN: 2093-8551. DOI: 10.33961/JECST.2019.00619. URL: http://www.jecst.org/journal/view.php?doi=10.33961/jecst.2019.00619.

[76] Zhengrui Xu et al. *Chemomechanical behaviors of layered cathode materials in alkali metal ion batteries*. 2018. DOI: 10.1039/c8ta06875e.

[77] Yue Wang et al. *Doping strategy and mechanism for oxide and sulfide solid electrolytes with high ionic conductivity*. Mar. 2022. DOI: 10.1039/d1ta10966a.

[78] Yi Chen Yin et al. "A LaCl3-based lithium superionic conductor compatible with lithium metal". In: *Nature* 616.7955 (Apr. 2023), pp. 77–83. ISSN: 14764687. DOI: 10.1038/s41586-023-05899-8.

[79] Charles D Wagner. *The NIST X-Ray Photoelectron Spectroscopy (XPS) Database*. 1991.

[80] Gordon B. Haxel, James B. Hedrick, and Greta J. Orris. *Rare Earth Elements—Critical Resources for High Technology*. Tech. rep. 2005. URL: https://pubs.usgs.gov/fs/2002/fs087-02.